STUDY OF HIGH ENERGY LEPTON, GAMMA RAYS AND HADRON INTERACTIONS IN PARTICLE DETECTORS

A Thesis submitted in a partial fulfillment of the requirements for the Award of the Degree of

DOCTOR OF PHILOSOPHY

IN

PHYSICS

By

S.N.L Sirisha

Department of Physics and Computer Science
Faculty of Science
Dayalbagh Educational Institute,
Dayalbagh Agra
(Deemed University)

2016

DAYALBAGH EDUCATIONAL INSTITUTE

DAYALBAGH, AGRA-282005

CERTIFICATE

Certified that Ms. S.N.L SIRISHA has completed Ph.D. research work in the subject Physics and Computer Science on the topic entitled: ***"STUDY OF HIGH ENERGY LEPTON, GAMMA RAYS AND HADRON INTERACTIONS IN PARTICLE DETECTORS"*** and is being submitted to Dayalbagh Educational Institute (Deemed University), Dayalbagh, Agra, for the award of the Degree of Doctor of Philosophy. As per bye-laws of the Institute and to the best of my knowledge and belief the research report presented in the thesis has not been submitted either in part or full to any other university or institution for the award of any other degree whatsoever. The thesis, in my opinion, has reached the standard fulfilling the requirements for the award of Ph.D. degree. The researcher worked for the required period and has put in attendance for the required number of days. The Ph.D. candidate has cleared all the dues to the Institute.

Sonali Bhatnagar.

Dr. SONALI BHATNAGAR

Supervisor

Dept. of Physics and Computer Science

Faculty of Science, DEI.

Forwarded

Prof. G.S TYAGI

Head, Dept. of Physics & Computer Science

Faculty of Science

Dayalbagh Educational Institute

Prof. Ravinder Kumar

Dean

Faculty of Science

Dayalbagh Educational Institute

DAYALBAGH EDUCATIONAL INSTITUTE

DAYALBAGH, AGRA-282005

DECLARATION

I solemnly affirm that the thesis entitled, ***"STUDY OF HIGH ENERGY LEPTON, GAMMA RAYS AND HADRON INTERACTIONS IN PARTICLE DETECTORS"*** embodies an original work carried out by me and has not been submitted, either in part or full, to any other University/Institute for the award of any other degree

(S.N.L SIRISHA)
Department of Physics and Computer Science
Faculty of Science

ABSTRACT

The Quantum Field Theory (QFT) of constituent part in high-energy physics motivates every researcher for tracking the ultimate structure of matter. The present research work have been carried out using a muon telescope to conduct experimental and Geant4 based simulation studies to understand the concept of electroweak and hadronic interactions with matter. The muon telescope is a new experimental setup after the Geiger Muller detector and NaI detector in our Detector Physics laboratory. This is an outcome of the collaboration between D.E.I and T.I.F.R, Mumbai under which the Institute has acquired plastic scintillation detectors from Cosmic Ray Laboratory, Ooty for research purpose. The Nuclear Electronics for the NIM has been setup in the laboratory along with a characteristic study of secondary cosmic rays. It is analyzed through a basic and advanced educational activity for post graduate (PG) students. The correlation between muon count rate corresponding to temperature and atmospheric pressure is also discussed to study Decoherence curve. It is nothing but measure of the muon coincidence rate as function of distance variation among the detectors. It mainly helps to determine one of the most interesting aspect of cosmic ray showers i.e. energy of primary particle.

Further discussion includes Geant4 based simulation of the muon telescope on implementation of a G4EMStandard Physics model for study of electroweak interactions in muon and gamma radiations. There are certain parameters which can’t be performed through an experiment such as multiple coulomb scattering (MCS) phenomena and cross-section of muon interaction processes, effect of surface characteristics of detectors on photon yield, Compton Effect. These concepts also been considered in this simulation study.

The study of hadronic interactions is based on medical application i.e. Hadrontherapy, where proton beams are used for curing tumors. The physical characteristics of proton beam such as stopping power and range and its equivalent dose for specific organs such as brain, thyroid and kidney for human phantom at different ages (0, 1, 5, 15 year and Adult) are computed through simulation.

ACKNOWLEDGEMENT

This work is an outcome of the inspiration and encouragement given by so many persons to whom words of thanks are merely a token of gratitude and appreciation.

I bow low and have no words to express my deepest regards and infinite gratitude to The Most Revered Prof. P.S. Satsangi, Chairman, Advisory Committee on Education, Dayalbagh Educational Institutions for His guidance and unbounded grace in all spheres of life which have crowned my humble efforts with success throughout my life. We are forever indebted to him for his magnanimity and motivation and making us realize that whatever we achieve in life is only due to Supreme Grace which crowns humble human efforts.

I am highly indebted to my supervisor, Dr. Sonali Bhatnagar at D.E.I whose timely efforts kept me on my toes to work as per the planned datelines. Her constant encouragement and ardent support made it possible for me to complete this work.

I am thankful to Cosmic Ray Laboratory (C.R.L), Field Station of Tata Institute of Fundamental Research, Ooty; for its technical assistance in fabricating and designing the plastic scintillation detectors. I would like to express special thanks to Prof. Sunil Gupta, Shri K.C Ravindran, Shri. Atul Jain, C. Ravi and to the staff , management of Cosmic Ray Laboratory, Ooty. Even want to express special thanks to Dr. Vipin Bhatnagar (Panjab University (P.U)), V.K Bhandari (P.U), Kundan Singh (Inter University Accelerator Center (I.U.A.C)), Ruby Santhi (I.U.A.C) and V.V.V Satyanarayana (I.U.A.C).

I extend my sincere thanks to Prof. Ravinder Kumar, Dean, Faculty of Science and Prof. G.S. Tyagi, Head, Department of Physics and Computer Science for making available the facilities of the Faculty during the course of this work. Their invaluable support and encouragement helped in sustaining the pace of the work.

I owe infinite gratitude to Prof. P.K. Kalra, Director, DEI, a visionary and academician beyond par for his patronage which encouraged me to take this work to fruition.

Similarly, I am grateful to Prof. V.G. Das, ex-Director, DEI for all the support extended by him from time to time.

I extend my warm thanks to my lab mate Miss Kajal Garg for creating a congenial environment for learning and discussions at every step during the project, and making it a memorable experience.

Words are inadequate to thank my parents, respected Mr. S.V.N Janardhana Rao and Mrs. S. Prema Kumari and my sister Anusha for their constant love, affection, blessings and encouragement. Their poise and charm have always been a source of inspiration during the trying moments. I am thankful to my husband Mr. Sarath Thatavarthy for his encouragement and support.

I am a product of the Dayalbagh Educational Institute and feel proud to be part of this great center of learning, which provides a unique atmosphere for academic pursuits and brings about physical, intellectual, emotional and ethical integration of an individual with a spirit of truthfulness, temperance and courage, and cultivates a spirit of humility, simple living, selfless service and sacrifice, while imparting education of excellence as well as of relevance to contemporary needs with a scientific temper.

(S.N.L SIRISHA)

Table of Contents

List of tables

List of Figures

Chapter – 1

Introduction

1.1 Origin of the proposal:

The structure of matter in this universe is meant to study from the standard model of physics **(Zohar, 2016).** It has been developed based on the concept of Quantum field theory (QFT) **(Schwartz, 2014)**. A consistent phenomenon is observed in nature can be understood through an interaction of the fundamental particles and their respective forces. These particles act in respective functions corresponding to their roles in this model. Currently, researchers are focusing on detecting particles and their performance beyond the standard model. The most recent highlight about the invention of Higgs boson which is conducted at Large Hadron Collider (LHC) **(Bahr, 2016)** leads to complete construction of standard model **(Macdonald, 2015)**. The search for new physics motivates the current research field to analyze cosmic ray experimental results at LHC energies. The principle of interaction kinematics in colliders and in cosmic rays leads to study of their energy spectrum ranging within the interval $10^{15} – 10^{17}$ eV (1-100PeV) **(Joyce, 2015)**. The higher their energy, the lower is their flux. Up to 10^{14} eV, cosmic rays undergo direct detection technique by use of balloon and space born experiments. But the flux of cosmic ray particles is too low at this energy range due to limitation on detector surface area **(Ellis, 2015)**. Thus, in order to determine the cosmic ray flux, one needs to study on the ground through the primary and secondary particle productions they generate.

When the primary proton in the atmosphere interacts with air nucleus, it results in generation of secondary particles ($\pi^{\pm}$, π^{0}, K, charmed particles D-mesons or Λ_c-baryons and particles with very short life time – resonances) **(Collaboration, 2012)**. This forms a cascade air shower also termed as Extensive Air Shower **(Carmi, 2012)**. These are mostly initiated by the decay of the neutral and charged pions, electromagnetic sub-cascades. The resultant charged pions may also further interact with air nuclei and decay into muons. At sea level, the charged component of the cosmic ray showers is mostly consists of muons **(Poulson, 2016)**. The neutrinos which are part of generation in the extensive air showers have a very low flux while compared to muons which are able to reach the earth's surface. The muons which are produced in the form of secondaries in a shower cascade are available in abundant along with its increase of energy of the primary cosmic ray and/or its mass **(Abbasi, 2013)**. They further decay into electrons, positrons and low energy gamma rays or photons.

The thesis work also mainly focus on the study of electrodynamics and strong interactions while particles penetrate through matter. The physics and the interaction phenomena of muons, gamma radiation and protons are simulated in a Monte-Carlo based Geant4 object-oriented toolkit. It is to study some important aspects which are difficult to attain without any considerate result. It includes different interaction mechanism of a particle, energy deposition into sensitive volumes and surface characteristics of the detector.

Muons play a key role mainly in cosmic ray experiments, especially for accelerators. They are produced from interactions of muon neutrinos and electro production of muon pairs **(Pich, 2012)**. A highly penetrating ability of these muons while compared to electrons and positrons leads to a possibility to detect them at larger distances **(Yu-Cheng, 2013)**. In cosmic rays, the muon detection is mainly involved in primary cosmic ray composition study where the heavy nuclei in its flux may lead to increase in its intensity **(Kojima, 2015)**. It also helps in understanding the background of the underground detectors and to simulate the atmospheric showers induced by muons. Muons at super high energies are considered for exploration of primary cosmic rays, neutrino studies in different arrays like Super-Kamiokande **(A.A.Petrukhin, 2014)**, GRAPES-3 (Gamma Ray Astronomy at PeV EnergieS) **(Gupta, 2014)** and for numerous environmental experiments like the solar report or observations from climatic changes **(Dayananda, 2013)**. Also, it has successfully been used in scientific search of volcanoes and also about hidden rooms in pyramids by implementation of muons in imaging technique **(B´en´, 2013)**. The other possible proposals which are applicable to deal with safety techniques in mining excavations, oil industries for scanning the vehicles at the custom checkpoints **(Overholt, 2015)**. An accurate determination of the source of gamma radiation to observe from its emission which is needed or desirable is used in many industrial and academic applications. Radiation therapy treatments, the search for unknown sources and homeland security applications are few of the fields that can benefit from directional sensitivity to gamma-radiation **(Cortes, 2014)**.

Hadron therapy is one of the technique that is developed to destroy the cancerous tumors by use of ionizing particles along with maintaining the functioning of adjacent healthy tissues **(Dosanjh, 2016)**. The emission of energy from radiation and its propagation through space or a material medium is different from a particle radiation. The term particle radiation is meant for the energy transmitted in cells with a considerable mass and momentum **(Seo Hyun Park, 2011)**. The relationship among these particles can only be explained through the Standard Model of fundamental particles which may not be a complete theory, but it helps in framework of theoretical and experimental advances **(Newhauser, 2015)**. The dose deposition of X-rays induced by different projectiles decreases slowly in relative to the diffusion of the tumor region. While compared to X-rays, the charged particle beams have a finite range of ballistics which helps in defining finest depth within the tissue **(Paganetti, 2013)**. Both proton and ^{12}C beams deposit their maximum dose located at the end of the path. This results in a Bragg Peak where its location depends on the beam energy, tissue density, and its composition. The proton beam gradually slows down by energy loss undergoing Multiple Coulomb Scattering with a material **(R, 2013)**. The consistency of dose deposition may also be influenced by inhomogeneous materials present in the path of beam direction. These inhomogenities results in degradation of Bragg peak and its range **(Park, 2011)** . This uncertainty in dose distribution can be determined from Full Width Half Maximum **(M, 2010)** (distance between the entrance surface of beam and distal FWHM) which has a large impact on treatment system because maximum dose of proton may be delivered to normal tissue **(S.N.L Sirisha, 2014)**. The point at 80% of energy deposition results in particle range during beam irradiation. Another parameter, penumbra width gives the resultant absorbed dose in distal region of Bragg peak. At low energy range (<100 MeV) **(Grassberger C, 2011)**, proton beams is a key issue in various experimental domain such as oncological radiotherapy, radiation protection, space science and optimization of radiation monitoring detectors **(Mendez, 2015)**. A number of medical physicists are making collaboration with Stanford Linear Accelerator Center (SLAC) **(Amaldi, 2014)** for working on Geant4 applications, especially for the treatment of tumors in in hadron therapy and brachytherapy.

In the upcoming sections, thesis objectives are given in section 1.2. The chapter ends with a brief description on outline of the thesis which comprises of summary of the research work performed. The highlights of the simulation and experimental results and their discussion for study of muons, gamma radiation and hadron interactions in various particle detectors are presented in section 1.3.

1.2 Thesis objectives

Step I: Fabricate and characterize the muon telescope.

a. Design and fabricate a muon telescope of dimension 23.5x24x2 cm^3, embedded with single and double fibre at Cosmic Ray laboratory, field station of TIFR, Ooty.
b. Find the acceptance of the telescope.
c. Find the efficiency of muon telescope.

Step II: Geant4 based simulation study of the high energy muon interactions with muon telescope.

a. Study the dependence of muon interaction processes on differential cross-section and its energy loss within the muon telescope.
b. Observe the muon response of the telescope and its effect on implementing various surface reflectors of UNIFIED model.
c. Study the electromagnetic interactions in telescope using standard, low energy and Penelope packages.

Step III: Energy spectrum and Rotational Matrix based study of Gamma rays.

a. Study the dependence of Compton scattering process on scattering angle based on Rotation Matrix of Geant4 simulation.

Step IV: Analytical study of hadron interactions in a sensitive region of a water phantom.

a. Determine the energy deposition of particle beams in homogeneous and inhomogeneous materials: Bragg Peak.
b. Compute the specific dose equivalent of proton beam for distinct ages of human phantom.
c. Study the influence of nucleus-nucleus collisions in study of dose computation.

1.3 Outline of the thesis

The thesis work mainly deals with study of interaction processes that a particle undergoes while penetrating through medium. There are also several other aspects such as cross-section, energy loss, response and surface characteristics of detectors that play a major role which helps in study of detector sensitivity and also can't be performed through an experiment. Thus, an object – oriented programming i.e. Geant4 simulation based toolkit is used to study the aspects and their principle which are mentioned above. The research work covers the study of interactions of muons, gamma rays and hadronic interactions performed in particle detectors. A muon telescope is fabricated at Cosmic Ray Laboratory (CRL), Ooty, a field station of TATA INSTITUTE OF FUNDAMENTAL RESEARCH (T.I.F.R), Mumbai. A brief description of experimental setup and its results are discussed in chapter 2. It includes the cut off rigidity of primary particle is to be 22GeV which is computed for the location i.e. Agra (27.18 N, 78.02 E), India where the experiment is situated. Integral muon flux computed from analytical and experimental calculation is 9.61/cm^2.sec.str with a statistical error of ±0.31%. The count rate as function of detector separation (horizontal-vertical) is determined to project decoherence curve over a period of 1 December 2014 – 16 September 2015. Three fold efficiency of muon paddle ranges within 60-80%. It also showed stability in muon detection. The correlation between temperature/atmospheric pressure and count rate was also analyzed. The chi-square testing is also applied for the count rate where the p-value of the correlation coefficient is observed to be less than 0.01.

In chapter 3, the theory of muon interactions with matter and significance of multiple scattering physics in its energy loss in matter is discussed. The physics models used in Geant4 simulation are based on theory of Quantum Electro Dynamics (QED) **(Nagashima, 2012)** which helps in energy loss calculations. The muon telescope is also simulated to observe the response of muon and also the effect on photon yield while corresponding to various surface characteristics. The Tyvek wrapping with a polished surface of dielectric_metal interface is observed to have 96% of photon yield that reaches the sensitive region of the detector. The intensity and peak energy of gamma radiation source (Cs-137) is observed for a plastic scintillator. The Compton scattering phenomena is also studied based on concept of rotation matrix on varying the angle between scatterer and detector. The characteristic study of secondary cosmic rays provided from a basic and advanced educational activity for undergraduate and PG students. The feedback is also analyzed based on the conceptual questionnaire of NIM (Nuclear Instrumentation Module) experiments performed in the laboratory.

Chapter 4 discuss the physical characteristics of particle beams in hadron therapy, its effect on curing tumors in presence of heterogeneous medium and specific dose equivalent required for patients of various ages. The key points of chapter 4 include: The stopping power of proton beam in various materials like brass, aluminum, copper, water, lead, plexi glass and galactic is computed within an energy range of 0.1 to 10^5 MeV. Physical distribution of dose curves of proton beam is studied from Geant4 simulation of the setup installed at INFN Catania **(Paganetti, 2013)**, for curing ocular tumors. The significance of the energy spectrum of secondaries generated during irradiation of 60 MeV proton beam is also observed from the study of Radioactive Biological Efficiency (RBE) and Spread Out in Bragg Peak (SOBP). The dose deposition of passive proton beam of 60 – 240 MeV in a human phantom is determined. The Bragg peak and its parameters are calculated and verified with results of other groups. The effect of the various medium in tumour has done by numerous reports that helps in finding the ability of beam density to determine dose equivalent required. Adipose, bone and soft tissues materials are simulated as inhomogeneous mediums along with their positioning of the tumor region are also designed. The energy range which is necessary in curing tumor corresponding to its volume is optimized. The parameters which have their impact on Bragg curve are also computed. A substantial error in the Bragg peak position is observed which is approximately of

-0.36% for muscular skeleton, -0.44% for soft tissue. The major effect on dose equivalent of proton beam which is necessary for treatment of tumors in human phantom at different ages is studied. Distinctive volumes of human phantom at various ages also simulated. The relation between dose equivalent and absorbed dose as function of depth to target volume is computed. A dependency of the dose deposition on patient's age is also observed i.e at younger age, a higher amount of dose is necessary, while it gradually decreases in the other cases i.e. 10 year, 15 year and adult.

The discussion ends with the conclusion along with its prospect of work in future directions in order to extend in initial directions of Quantum Field Theory.

Chapter 2
Muon Telescope – Experimental Studies

(This chapter is based on the following published papers)

- Shubhi Parolia, S.N.L Sirisha, Sonali Bhatnagar ***"Preliminary Studies of Muon Telescope"*** presented in IARPNC-2014: 31. IARP National Conference on Advances in Radiation Measurements Systems and Techniques; Bhabha Atomic Research Centre; Mumbai and published in conference proceedings by Indian Association for Radiation Protection (IARP), Reference No: 46053360, The International Nuclear Information System (INIS) Volume: 26, INIS Issue:23, 2014.
- S.N.L Sirisha, Kajal Garg, Sonali Bhatnagar "***Muon Telescope – An Educational Experiment For Post Graduate Students",*** published in Physics Education Journal, Indian Association of Physics Teachers: ISSN 0970-5953, Volume 32, Issue 1, Article no: 12, Jan-Mar 2016, Page No: 1-17.
- S.N.L Sirisha, Kajal Garg, Sonali Bhatnagar ***"Study the correlation of muon paddle efficiency with temperature, pressure, decoherence curve and effect of Multiple Scattering Physics in Geant4 based detector simulation" ,*** International Journal of Current Research Vol. 8, Issue, 09, pp.39537-39545, September, 2016.

2.1 Observables of Muon flux at sea level:

The spectrum of relativistic particles has been observed ranging from 10^6eV to 10^{19}eV **(Cecchini, 2012)**. It is described by a power law which slightly steepens at $3x10^{15}$eV termed as 'knee' and the spectrum flattens down at the ankle near $3x10^{18}$eV **(Blasi, 2013)**. This may be due to the restriction on particle acceleration at knee region where as the ankle part results in transition of particles from extragalactic origin. The primary CR (cosmic radiation) in earth's atmosphere undergoes interaction with electrons and nuclei of atoms and molecules that constitute the air. As a result, the composition of radiation changes as it propagates through the atmosphere and forming cascades of showers that comprises of electromagnetic (80%), muonic (1.7%) and hadronic (0.3%) components **(Ralph Engel, 2011,)**. They also suffer energy loss undergoing hadronic and electromagnetic processes while propagating the atmospheric medium. At sea level, the charged component of the cosmic ray showers is mostly consists of muons. They further decay into electrons, positrons and low energy gamma rays or photons. High energy strong interactions as well as electromagnetic processes such as pair production lead to the secondaries in the shower cascade **(Sirisha, 2014)**. The collision or interaction of particles can be explained in terms of cross-section which helps us to determine the probability for an interaction process to occur while particle penetrating through a medium.

Relativistic charged particles will produce scintillation and Cerenkov light as they propagate through a detector in the atmosphere. The excitation of nitrogen molecules also finally results in emission of fluorescence light. Detector sensitivity for a particle of incident energy depends on many factors including cross-section for ionizing reactions in the detector, characteristic detector noise and surface material that surrounds the sensitive volume of the detector **(B.Mitrica, 2015)**. The cross-section and detector mass determine the probability of the incident particle to convert its energy deposited in the detector into form of ionization. When a highly ionized charged particles incident on a detector of low density and small volume, it produces ionization resulting in a certain minimum amount of signal which is further determined by noise from the detector and its associated electronics in the form of a fluctuating voltage or current at the detector output. The surface material which is used to cover the detector may also restrict the particles to penetrate through it due to the ability of absorbing the radiation which is below the threshold energy range **(Collaboration, 2014)**. For measurement of energy spectra, an important factor which must be considered is the response of the detector.

The experimental studies on muon intensities at sea level have been important for astrophysical standards and also contain information about cosmic ray interaction processes **(Mauro, 2014)**. The probability of a muon i.e. 'dP' to decay in a time interval 'dt' which is insignificant and also independent of its life time is denoted by:

$$dP = \Gamma dt \qquad (1)$$

here Γ is the decay rate and is inversely proportional to the lifetime of muon: $\Gamma = 1/\tau_\mu$

This process of muon decay within the time interval i.e. t to $t+dt$ surveys an exponential prospect of probability density function:

$$dP_e(t) = \Gamma e^{-\Gamma t} dt \qquad (2)$$

Here, the time t is called as decay time which is measured as a time required for a particular decay to occur. At the earth's surface, the differential flux of cosmic ray muons (per unit time, per unit area, per unit solid angle) **(Sirisha, 2014)** is approximately described by:

$$\frac{dN}{dA d\Omega dt} \approx I_0 cos^k \theta \qquad (3)$$

here θ is a polar angle with respect to vertical direction of earth's surface, $k \approx 2$, and $I_0 \approx 100$ $m^{-2}sr^{-1}s^{-1}$ at sea level. But the flux of muons is not expected to be dependent on the azimuthal angle ϕ. The equation (3) is also not valid for $\theta > 80^\circ$ since beyond that range, the Earth's curvature will be considered for study.

The muons gradually lose their incident energy while penetrating through the atmosphere and its materials. The scattering nature of any particle within the medium leads to energy loss and also forms scattering angles. At very low energies of muons, the angular scattering becomes small and also significant **(D.J Thomson, 2012)**. The stopping power or mean energy loss per unit length for any charged particle while passing through a medium can be directed by the Bethe-Bloch equation:

$$\frac{dE}{dx} = -Kz^2\frac{Z}{A}\frac{1}{\beta^2}\left[\frac{1}{2}ln\frac{2m_ec^2\beta^2\gamma^2T_{max}^2}{I^2} - \beta^2 - \frac{\delta}{2}\right] \quad (4)$$

From the equation, we need to know that β and γ are the relativistic factors, Z and A are the atomic and mass number of the medium, z is the charge of the incident particle, T_{max} is the maximum kinetic energy which can be transmitted to an electron during collision, and K, I, and δ are the atomic factors. Figure 1 shows the stopping power of muons as a function of momentum while incident on a copper medium **(PDG et.al, 2015)**. The units are in MeV cm^2/g.

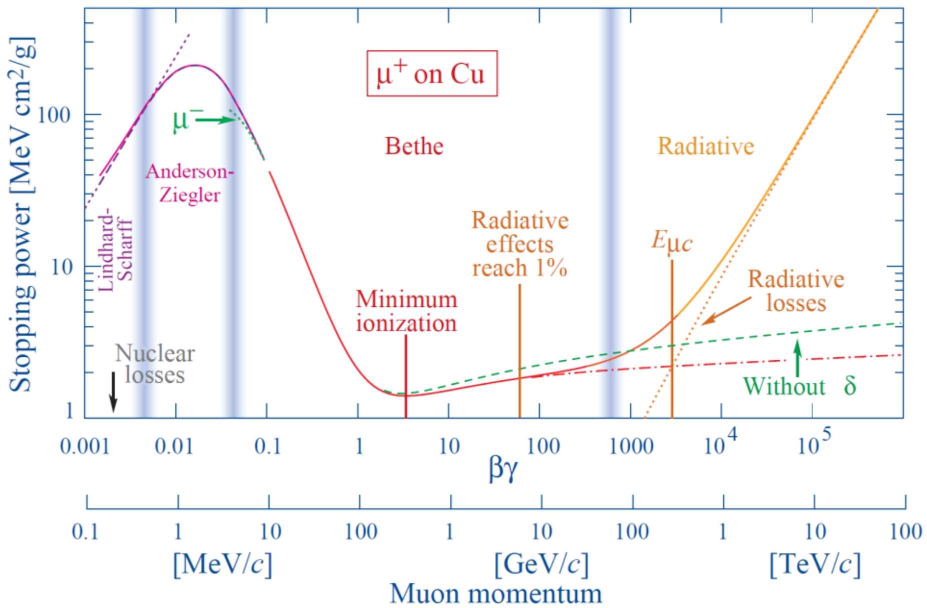

Figure1: Muon stopping power in a copper medium ***(PDG et.al, 2015).***

It can be observed from figure that initially the charged particles promptly lose energy through ionization at low momentum which results in increase of stopping power. But in relativistic case, the stopping power decreases while momentum gradually increases and reaches a minimum value **(D. Kosenko, 2014)**. Further, it increases gradually from its minimum value corresponding to a continuous increase of particle momentum. Even though, when a muon can travel with speed of light, it can travel only 660 m before decaying in 2.2 μs **(B´en´, 2013)**. But due to the effect of time dilation of relativity, only high-energy muons are able to travel much far distance before decaying and can also reach our detector where we can measure their flux and angular distribution.

Once a muon comes to rest in a material, it can decay into an electron and two neutrinos with an average lifetime of 2.2 μs as already mentioned. However, for negatively charged muons ($\mu-$), a second decay process is possible. Negative muons, once stopped, can displace an atomic electron in the material and be bound with an atomic radius 207 times smaller than that for the displaced electron.

The directional intensity $I_i(\theta,\phi)$, of muons is defined as the number of muons (i) while incident dN_i on an area, dA, per unit time, dt, within an element of solid angle, $d\Omega$. Thus,

$$I_i(\theta,\phi) = \frac{dN_i}{dAdtd\Omega}[cm^{-2}s^{-1}sr^{-1}] \tag{5}$$

The intensity is dependent on the zenith angle θ and azimuthal angle ϕ and also on the energy, E, and on time, t. It can be determined either in the form of total intensity integrated over all energies, $I_i((\theta,\phi) > E, t)$ or form differential intensity, $I_i((\theta,\phi), E, t)$. The flux, $J_{l,i,}$ is defined as the number of particles of a given kind, i, that travels in a direction towards downward on a horizontal element of area, dA, per unit time, dr. Thus,

$$J_1 = \int I(\theta,\phi)\cos(\theta)\, d\Omega\ \ [cm^{-2}sec^{-1}] \tag{6}$$

On integrating the directional intensity I over all angles, we get the omnidirectional or integrated intensity, J_2 i.e.

$$J_2 = \int I(\theta,\phi) d\Omega \tag{7}$$

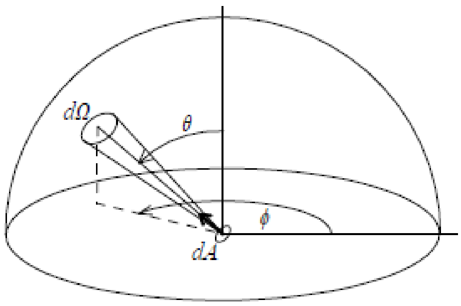

Figure 2: Schematic representation of directional intensity and solid angle. Here θ and ϕ are the zenith and azimuthal angles and $d\Omega$ is solid angle respectively, ***(B.Mitrica et.al, 2014).***

But we know from the conceptual description of directional intensity and solid angle i.e. from figure 2; that $d\Omega = sin\theta\ d\theta d\phi$. Thus,

$$J_2 = \int_{\theta=0}^{\pi}\int_{\phi=0}^{2\pi} I(\theta,\phi)sin(\theta)d\theta\ d\phi \tag{8}$$

There were also numerous number of reports which mentions about muon measurements that were carried out in horizontal direction with a large ground based magnetic spectrometer at Mt. Aragats, Armenia (250 m a.s.1.) **(Asatiani et al. 2013)**. A series of new complex balloon-borne instruments employing superconducting magnets were also used to determine the vertical muon intensity over a wide range of atmospheric depths. **(Bellotti et al., 2016 and 2013; Carlson et al., 2012; Coutuet al., 2011; Franke et al., 2010; Golden et al., 2009; Krizmanic et al. and Schneider et al. 2008**). Even at low energy range, they have a maximum detectable momentum of 100 GeV/c. The low energy capabilities are particularly important for the accurate determination of the low energy muon spectrum and charge ratio which are relevant in connection with the study of atmospheric neutrinos. **Blokh et al. (2015),** investigated from his study that a dependence of integral vertical muon intensity w.r.t altitude in the lower regions of the atmosphere ranges between 650 and 950 g cm^{-2} with the help of a scintillation telescope which is shielded by a 10 cm of lead. A magnetic spectrometer is used by **Shen and Chiang (2014)**, which is in conjunction with a counter hodoscope in order to determine the intensity at 320 m from sea level. They found the vertical muon intensity, I_v, for energies > 2 GeV:

I_v (≥ 2 GeV) = (4.9±0.2). 10 $^{-3}$ [$cm^{-2}s^{-1}sr^{-1}$]. (9)

Unlike photons and neutrinos, muons are the most abundant component among secondaries at sea level. In addition muon data reveal information on high energy processes in the atmosphere and on the primary radiation, in particular on its spectrum and composition. A complete collection of reviews on this issue have been presented in papers at international cosmic ray conferences and in review articles **(Allkofer, 2012 and 2013a; Thompson, 2011; Kitamura, 2011; Narasimham, 2010; and Ryazhskaya, 2009). S.K Gupta et al. (2014)** even gave a detail report recently regarding some theoretical aspects of atmospheric muons, which includes their contribution to charm decay and its comparisons with the data obtained from experimental setup.

Another important parameter is the vertical muon intensity at sea level. It is relatively dependent on geomagnetic latitude A, at low momenta (p≤ 5 GeV/c) where the measurement is performed from the solar activity. The geomagnetic cutoff rigidity and its effects performed in present study is discussed in the upcoming section 2.2. Muon measurements up to 2014 had been summarized by **Allkofer and Jokisch (2014).** The so-called hard component which penetrates 15 cm of lead (167 g/cm 2) consists mostly of muons (p > 0.3 GeV/c), and protons or other particles are nearly less than 1%. The vertical integral intensity, I_v (≥ p), flux, J_1 (≥ p), and the omnidirectional intensity, J2 (≥ p), of the hard component at a latitude of 50^{o} and an altitude of 259 m at sea level (1007 g.cm $^{-2}$) mentioned here below which are obtained by (Ithaca, N.Y.) **(Greisen 2012).** The data which is applicable for muons of momentum ≥0.35 GeV/c, would result in a slight inclined trajectories in the absorber of the muon telescope.

I_v(≥ O.35 GeV/c) = 0.82-10 $^{-2}$ [$cm^{-2}s^{-1}sr^{-1}$] (10)

J_l(> 0.35 GeV/c) = 1.27.10 $^{-2}$ [$cm^{-2}s^{-1}$] (11)

Precise measurements of the muon flux are important for different practical applications, both in environmental studies and for the approximation of the water equivalent depths **(Abgrall,**

2016). A mobile detector has been setup at IFIN-HH, Romania for cosmic muon flux measurements **(B.Mitrica, 2015)**. It is used to measure the muon flux on different locations at the surface and underground **(Mitrica, 2013)**. The Lawrence Berkeley National Laboratory (LBNL) also designed a plastic scintillator (EJ212) coupled with a light guide to PMT for detection of gamma rays and to improve its efficiency. The effect of different shielding on gamma rays produced and the flux dependency on direction were also studied **(Bachri, 2011)**. In recent years, a numerous number of high schools and universities are making collaborations (for e.g.: CROP (Cosmic Ray Observatory Project), CHICOS (California High School Cosmic ray ObServatory), SEASA (Stockholm Educational Air Shower Array), ALTA (Alberta Large Area Time-Coincidence Array) for performing the cosmic ray studies all over the world **(Riggi F. , 2014)**. Many educational aspects tend to characterize the experiments using different detection techniques for study of fundamental properties of high energy particles. This has also offered a possible usage of the advanced nuclear laboratory which involves construction of apparatus, use of different detectors, physical measurements, muon monitoring, data analysis and interpretation for students in field of high energy physics **(Riggi S, 2013)**. Instead of measuring the number of particles passing through the detector, efficiency of the entire system can be determined from the coincidence measurement. The ratio of coincidence counters to optimized counters allows to study the number of particles in a particular counter detects relative to the others **(A.A Petrukhin, 2014)**.

2.2 Muon Telescope Experimental Setup

The motivation behind the work discussed is to study the correlation between muon count rates with the atmospheric parameter that may affect detector sensitivity. The Muon Telescope, a prototype detector which is used in this work, aims for exposure of cosmic ray muons. The relativistic nature of muons provides a life time of 2.2 μsec can penetrate the earth's surface without absorbing in matter. The muon rate would be 1 muon/cm^2/min/str at sea level. A series of calibration procedures using muon telescope were performed. The light leakage testing, discriminator threshold and operating voltage of the photo-multiplier tube are optimized to suppress the detector noise which allows for greater sensitivity and little interference of background radiation **(Sirisha et.al, 2014)**. The characteristic study of secondary cosmic rays provided from a basic and advanced educational activity is performed with the help of undergraduate and PG students **(Sirisha et.al, 2016)**. It is based on the conceptual understanding of NIM (Nuclear Instrumentation Module) experiments performed in the laboratory which is discussed in Appendix I. The relativity within the intensity and energy spectrum of cosmic ray muons are analytically computed and discussed in section 2.2.1. To characterize the muon telescope, the acceptance of the detector is computed using Matlab 7.1 and its effect on varying distance among two detectors when placed in coincidence also observed. The significant influence of muon paddle efficiency by environmental factors like temperature and pressure is analyzed and discussed in section 2.2.2. For a better understanding of the muon flux, the count rate dependence is observed on varying the distance among the two muon paddles at different elevations in section 2.2.3.

2.2.1 Intensity and Energy Spectrum of Cosmic Ray Muons

This section gives a detail description of relevant processes that may influence the cosmic ray phenomena while propagating in atmosphere and at sea level. The primary radiation of cosmic rays is influenced mostly by galactic, interplanetary, magnetospheric and geomagnetic fields while reaching the earth's surface **(Grider, 2008)**. The interplanetary magnetic field is only about 5 nT at earth's orbit. The magnetospheric fields also significantly vary on undergoing secular changes while the geomagnetic field is generated by sources inside the earth. The secondary cosmic rays which are electrically charged also subject to effect of geomagnetic rigidity.

Charged particles while reaching the Earth from outer space tend to form into curved trajectories due to the presence of geomagnetic field in their propagation. They also subject to interactions with atmospheric constituents **(Yun Ho Kim, 2012)**. Let us consider that whether a particle can reach the Earth's surface irrespective of its magnitude and direction within the local magnetic field, along with its rigidity and direction of propagation.

A practical measure to compare and understand its measurements which are performed at different locations on Earth, particularly at diverse geomagnetic latitudes, are the effective vertical cutoff rigidity, P_c, which is referred to as the cutoff rigidity **(Grider 2008)**. It must be emphasized that in general P_c depends on location and time whereas geomagnetic and geographic coordinates are not the same. It is a coordinate that designates charged particle contact at any location in the magnetosphere. They are used to describe both the shielding effect of the geomagnetic field and also to order the data of charged particle which is acquired from the magnetosphere. The charged particles while traversing within a magnetic field would undergo a vector force that leads to a curved path and also subject to interactions with atmospheric constituents. The particles which are able to reach the earth’s surface mainly depend on magnitude and direction of earth’s magnetic field and also on rigidity and direction of particle propagation. The study of cosmic ray muons which are able to reach the earth’s surface within geomagnetic field helps in observation of directional asymmetries detected in flux at low energies. In this paper, the cutoff rigidity (GV) of primary cosmic rays for a specified region at latitude of 28.12^0 N and longitude 78.02^0 E i.e. Agra, India where the experiment is been setup. It is calculated using stormer’s equation which mainly concerns with the discrepancy between arrival directions of a particle from interplanetary space at a given location in geomagnetic field direction.

$$R_c = \frac{M\cos^4(\lambda)}{r^2[1+(1-\cos^4(\lambda)\cos(\epsilon)\sin(\zeta))^{1/2}]^2} \quad (12)$$

R_c is geomagnetic cutoff rigidity (in GV), M is magnitude of dipole moment in G cm^3, λ is latitude from magnetic equator, ϵ is zenith angle and ζ is azimuthal angle, r is distance from the dipole center (earth’s radii). The magnitude of dipole moment has been normalized to 58 G cm^3. $R_c = \frac{14.5\cos^4(\lambda)}{r^2}$. Thus for geomagnetic latitude at 28.12^0 N with zenith angle direction in $\theta=0^0$ the obtained cut off rigidity is 22 GV. The cutoff rigidities in Tsukuba (36.2^0N, 140.1^0E) and

Lynn Lake (56.5^0N, 101.0^0 W) were also computed using Stormer equation, i.e. 11.4 GV and 0.4 GV respectively. The major difference among the results while comparing with present discussion is mainly due to the altitude of the experimental site considered. The angular and azimuthal dependence of cutoff rigidities is also studied at Agra, India which is located at 28.12^0 N latitude, 78.02^0 E longitude and 169 m altitude above sea level. It can be observed from figure 3. The azimuthal angle is varied from 0 to 2π direction and the cutoff rigidity of primary particle is observed for each zenith direction i.e. $0\text{-}80^0$.

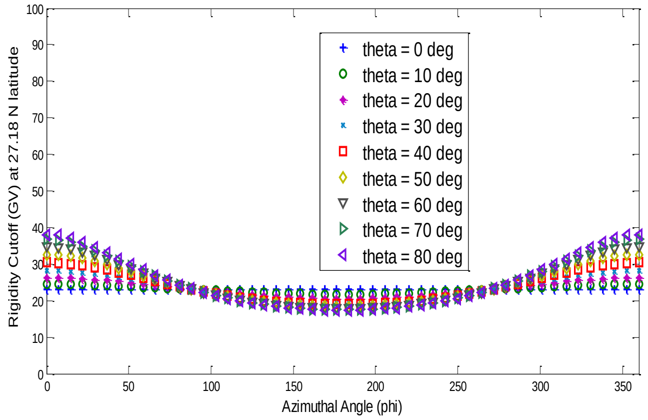

Figure 3: Effect of azimuthal angle on rigidity cutoff of primary particle w.r.t earth's surface.

A significant azimuthal asymmetry is observed in the cutoff rigidity due to location which is near to the equator. The cutoff rigidity in different directions at different zenith angles is observed from figure 3 where the primaries cutoff rigidity is subjected to fall at higher zenith angles.

The experiment considered for the present study mainly deals with cosmic ray muon flux using muon paddle. It is characterized for a detector setup of area 564 cm^2 ($24\text{x}23.5\text{x}2\ cm^3$) which are placed in coincidence. The area of top detector 'A_t' defines the solid angle of acceptance 'Ω_t' for each area on 'A_b' i.e. bottom detector. It is shown in Figure 4.

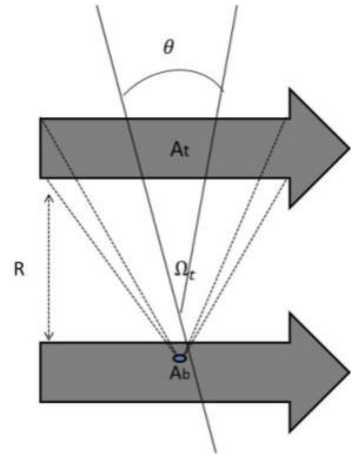

Figure 4: Geometrical description of telescope when two detectors are placed in coincidence. The dotted line shows the solid angle Ω_t *subtended from top to the bottom detector and R is the distance separated* ***(CRM Experiment et.al, 2013)***.

Solid angle is the acceptance of muons arriving at the detector area. For present setup, the solid angle obtained is $\Delta\Omega_2 = \frac{A_t A_b}{d^2} = 0.15\, radians$. The effect of solid angle while varying the distance between two detectors is also studied. A gradual decrease in solid angle can be observed from figure 5 on increasing the distance among the detectors.

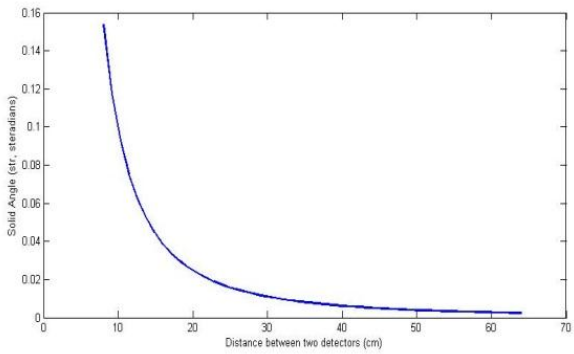

Figure 5: Effect on solid angle obtained on varying distance between two detectors when placed in coincidence.

The differential intensity as discussed in section 2.1 of cosmic muons i.e. number of particles per unit area per unit time per solid angle per energy is observed to be 8.84 x 10^{-2} ($sr^{-1}.cm^{-1}.sec^{-1}$. $(GeV/c)^{-1}$). The correlation for distance between the detectors corresponding to solid angle, count rate, integral flux and differential intensity of the muon are also studied and shown in table 1. There is a gradual decrease in the parameter on increasing the distance. This is due to dependence of solid angle and count rate on the area of the detectors. As the distance is varied, the solid angle gets decreased, which may affect the acceptance of the detector. This leads to decrement in efficiency of the detector

Table 1: Correlation among the solid angle and count rate of muon telescope on varying the distance among the detectors

Vertical Separation (cm)	*Solid Angle (Steradian)*	*Muon Rate/sec*	*Integral Intensity (sr^{-1}. cm^{-1}. sec^{-1})*	*Differential Intensity x10^{-2} (sr^{-1}. cm^{-1}. sec^{-1}. $(GeV/c)^{-1}$)*	*Statistical Error (%)*
8	0.15	775±27	9.61	8.84	±0.31%
10	0.09	471±21	9.27	8.52	±0.41%
12	0.06	333±18	9.04	8.31	±0.53%
14	0.05	244±15	8.65	7.95	±0.54%
16	0.03	163±12	8.53	7.84	±0.60%
18	0.03	124±11	7.32	7.21	±0.65%
20	0.02	119±10	6.54	6.01	±0.68%

The dependency of muon differential intensity w.r.t muon momentum is also computed which is shown in table 2, where a proportional increase can be observed.

Table 2: Differential Intensity (sr^{-1}. cm^{-1}. sec^{-1}. $(GeV/c)^{-1}$) w.r.t Muon momentum (GeV/c)		
Muon Momentum (GeV/c)	*Differential Intensity x 10^{-2} (sr^{-1}. cm^{-1}. sec^{-1}. $(GeV/c)^{-1}$)*	*Statistical Error (%)*
0.35	3.36	±0.18
0.45	4.32	±0.20
0.55	5.28	±0.22
0.65	6.24	±0.24
0.75	7.20	±0.26
0.85	7.78	±0.27
0.95	9.12	±0.30

2.2.2 Efficiency of the Telescope:

The setup used for conducting the studies is shown in figure 6. To transmit the signal processing from detector set up we used NIM bin (Nuclear Instrumentation Module). It provides a standard negative NIM logic output pulse of >-0.8V amplitude with an adjustable pulse width ranging from (2-60) ns. The signal cables from each paddle counter of 9.7 m with 48.6 ns delay is connected to the Quad 300 MHz Discriminator Model 704, Phillips Scientific. Then discriminator threshold is optimized at -15 mV to further transmit the signal into digital form with 60 ns in pulse width on suppressing the noise rate. This unit introduces a delay of 8 ns between the input and output pulse. Further the digital signal from discriminator is carried with a 92 cm cable length which has a delay of 4.6 ns to the scalar Model N1145 Quad Scaler and Preset Counter/Timer, CAEN is used to count logic (NIM) pulses for a preset period of time. In this study, counter is operated in TIMER mode the counter is decremented by an internal clock, regardless of the input pulses. The 8-digit up counters was operated in GATE+CLEAR mode where the leading edge of the GATE input clears the counter.

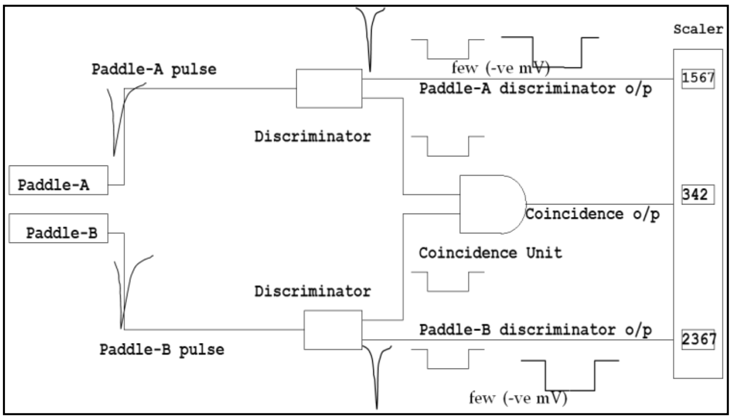

Figure 6: Experimental setup used for studies conducted in present report

To improve the acceptance value of plastic scintillator while suppressing the lower energy signals from PMT, the operating voltage for each detector i.e. (Double Fiber Detector, DFD and Single Fiber Detector, SFD) is determined. The experimental setup is shown in figure 6. The coincidence rate/sec with respect to high voltage (H.V.) is observed for each PMT of the detector in order to determine its operating voltage.

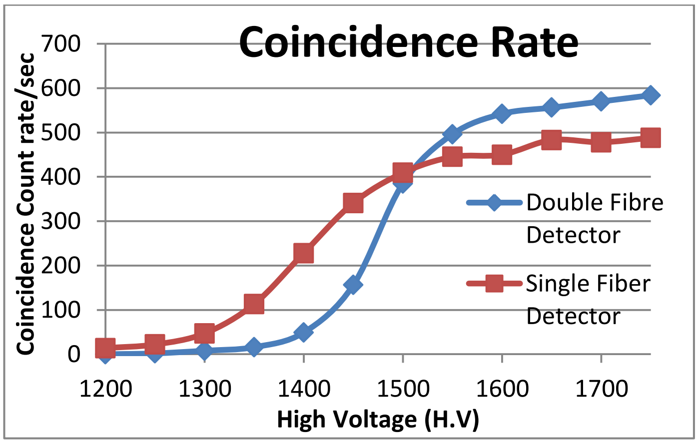

Figure 7: Operating voltage of PMT in DFD and SFD

From the plot (Figure 7), the operating voltage for each detector is observed at the point of inflexion for single fiber detector it is observed to be 1500V and for double fiber detector at 1550V. While making the coincidence measurement, we should consider the uncorrelated background events in the detector. They may arrive within the resolving time of the circuit or through random noise which triggers the discriminator. We can overcome this disadvantage by measuring the accidental coincidences that occur in circuit which must be kept to a minimum. The rate of accidentals can be estimated from the singles rate in each detector and the time resolution of the circuit. Consider n1 and n2 are the individual count rate for detector 1 and 2 respectively and τ is the resolution time which is set to trigger the circuit. Total number of accidentals per unit time, $A = 2\tau n_1 n_2$, Where τ is 60 ns. Correlation of detector count rate with accidental is shown in figures 8 (a), (b).

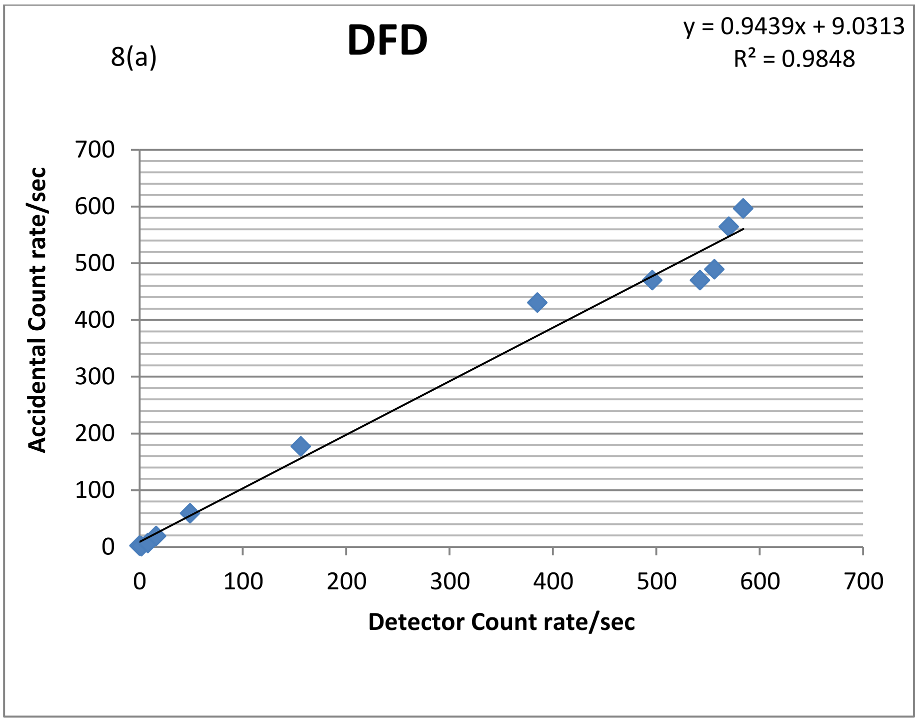

Figure 8(a): Correlation between detector count rate and accidentals in double fiber detector

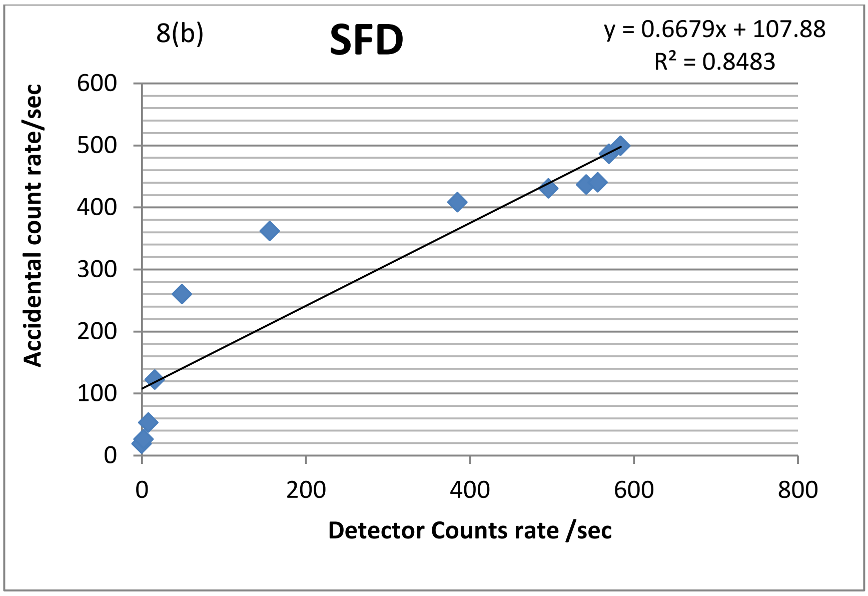

Figure 8(b): Correlation between detector count rate and accidentals in single fiber detector

From figure 8 (a), (b); we can observe a linear relation with in the detector count rate and its accidentals. This is due to the noise which gradually increases with count rate on increasing the high voltage (H.V) of the PMT. The count rate of muons passing through two detectors comprised in the setup is 775±27/sec. The flux N is determined from observed coincidence rate $N = N_c \frac{d^2}{A_1 A_2} = 9.16 \pm 0.31/$ cm^2.str.sec. It is further set to determine the efficiency and also observed the effect on count rate by distance separation among the detectors. Many studies also enlighten their significant role of cosmic rays in formation of low cloud coverage and its consequent impact on the global temperature variation of the earth. Ground based detectors such as Oulu, ASEC and WILLI **(S.K Gupta, 2014)** focus on correlation studies of space and earth's atmosphere weather patterns with variation of cosmic ray neutron and muon flux. The correlation of secondary cosmic ray muons flux relative to earth's atmosphere and space weather patterns was also studied by a Nuclear Physics Group of Georgia State University. The coincidence data of the detector is observed over a period of 16 Dec 2014 – 24 Dec 2014 to observe its effect due to temperature, pressure and humidity. The efficiency of the detector was calculated using

$$\eta = \frac{C_{D1 \cap D2 \cap D3}}{C_{D1 \cap D2}} \tag{13}$$

Where η is efficiency, $C_{D1\cap D2\cap D3}$ is number of muons detected in D1, D2 and D3, $C_{D1\cap D2}$ is number of muons detected in D1 and D2 respectively.

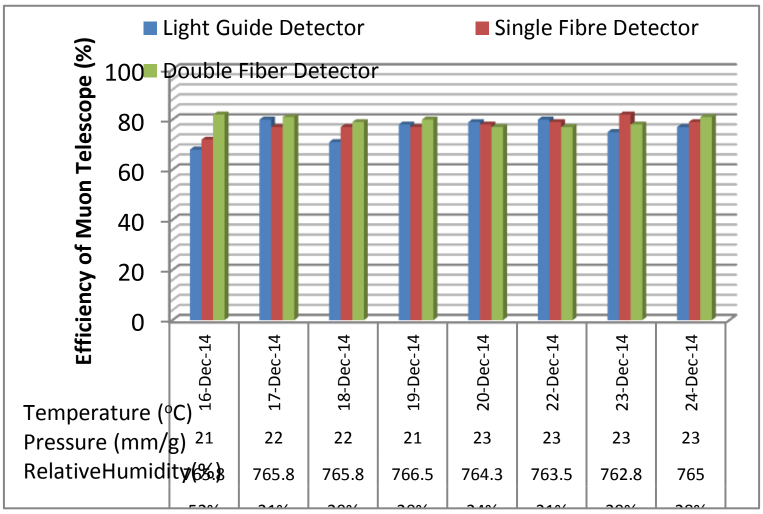

Figure 9: Efficiency of Muon Telescope as function of Temperature, Pressure and Humidity.

It is observed from figure 9 that the efficiency of each detector ranges within 60 – 80 %, which also proves that telescope is suitable for muon detection.

2.2.3 Decoherence Curve and Correlation of Count Rate with Temperature and Atmospheric Pressure:

Measuring muon flux at different heights above the sea level is an important relativistic time dilation experiment. It is also important in many applications such as low background measurements, environmental factors like characterization of solar activity **(Cecchini, 2012)**. Two plastic scintillators with fibers are considered for the present study. The count rate dependence on varying the distance between them is observed. In first case, the detectors are separated in upright and plane direction i.e. (0 foot (0 m), 1 foot (0.3 m) and 2 foot (0.7 m)) respectively. The data obtained over the period is shown in Table 3 where the count rate obtained is also compared Experimental setup used for studies conducted in present report with theoretical calculations.

Table 3: Count rate obtained on varying distance among the detectors

Distance Varied	*Theoretical (Muon Rate/sec)*	*Experimental (Muon Rate /sec)*								*Error%*
		Day1	*Day2*	*Day3*	*Day4*	*Day5*	*Day6*	*Day7*	*Day8*	
0 foot (0 m)	775	762	778	771	775	759	765	770	769	±0.01
1 foot (0.3 m)	108	98	101	95	91	97	92	96	93	±0.09
2 foot (0.7 m)	76	53	58	51	57	55	59	52	54	±0.3

Here the count rate on varying the distance within the detectors is also observed at different elevations i.e. both inside a room and at roof (10m height from ground level). It is observed that the count rate gradually decreased, on increasing the distance among the detectors. But the count rate is less at ground level when compared to an altitude of 10 m. Here the detector separation gives a possible approach to collect single muons and the detected coincidences are from related air shower particles. One of the most common measurements is decoherence curve, which is the rate of particle coincidences in two detectors as a function of detector separation.

Consider muons passing through a detector setup where in order to count the coincidences for a period of time. In Figure 10 (a), (b); detection results from 1 Dec. 2014 to 16 Sep. 2015 show that the count rate was relatively low at low atmospheric pressure. The motive for this outcome was absence of adjustment in the laboratory environmental temperature. Due to the variation of temperature, an expansion of change in the detection system was responsible for a direct proportional relationship between the count rate and the atmospheric pressure.

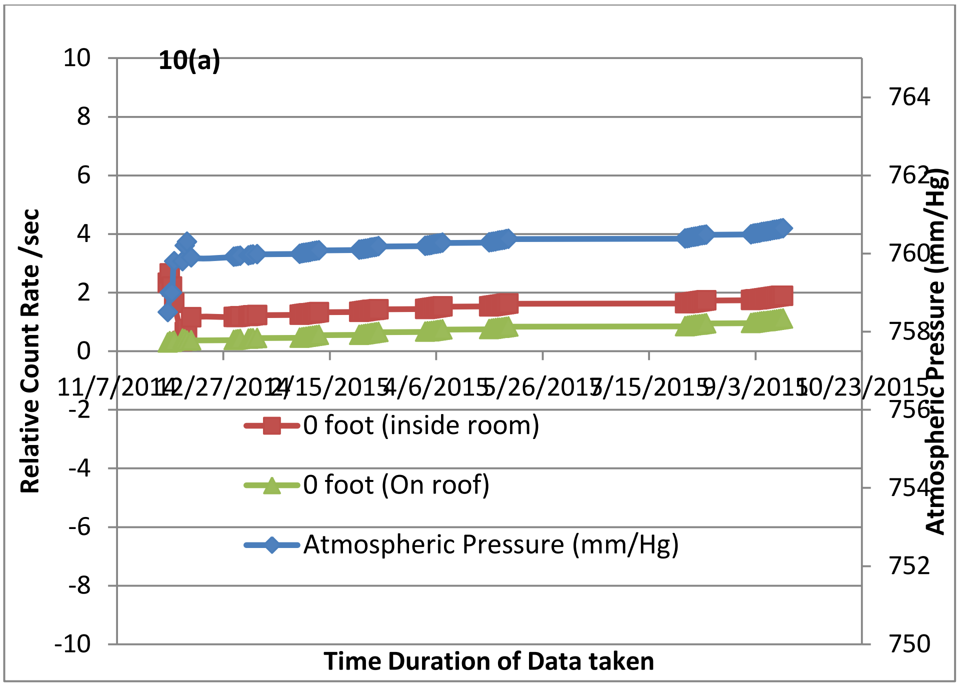

Figure 10(a): Relative Count rate corresponding to atmospheric pressure

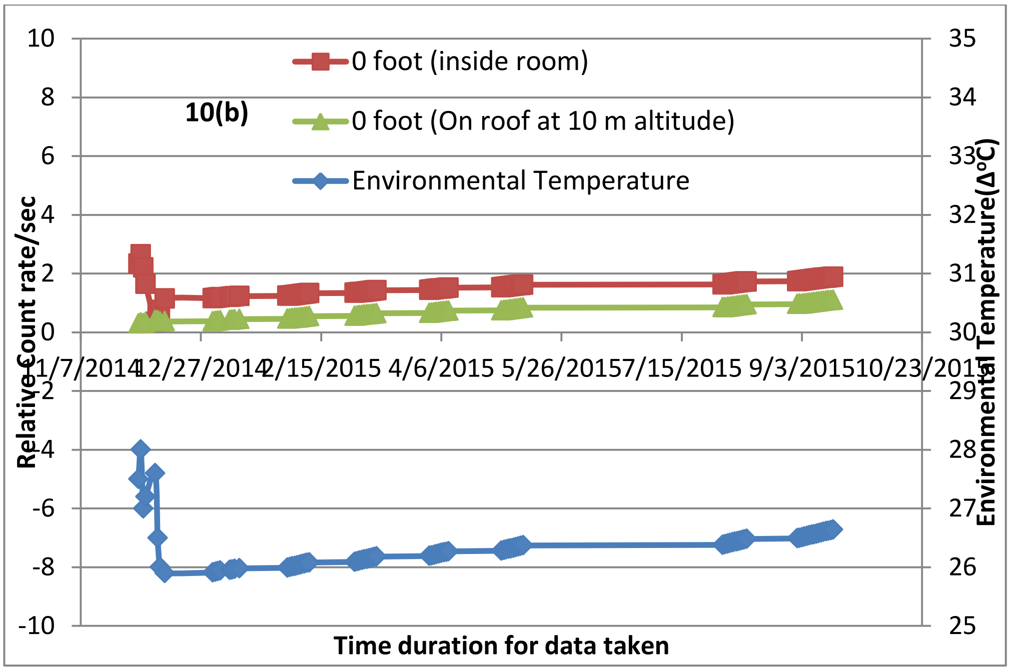

Figure 10(b): Relative Count rate corresponding to environmental temperature

The correlation between the laboratory environmental temperature and the count rate with the chi-squared test was analyzed. The p-value for the experimental era was less than 0.01 (significance level 1%), so the correlation between the experimental temperature and the count rate was valid. The study of coincidence rate as function of detector separation helps to determine the decoherence curve. Figures 11 (a), (b); show a correlation between the count rate and the laboratory environmental temperature where it is observed that count rate is proportion to the temperature (figure 11(b)). The slope of the fitted curve also indicates the degree of dependence.

$$\frac{\Delta I}{I} = \alpha \Delta T \quad (14)$$

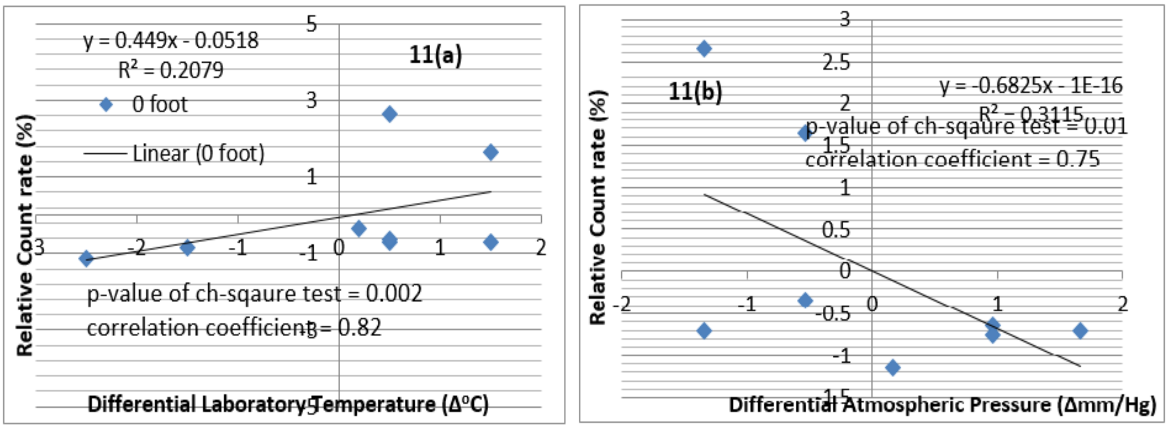

Figure 11(a), (b): Correlation between relative coincidence rate corresponding to differential laboratory temperature and atmospheric pressure.

The correlation between count rate and atmospheric pressure is also observed in inverse relation. It is due to atmosphere which acts as an absorber for muons which results in lower count rate at high pressure. It is also observed to be ranging from 0.293 to -0.1112 mm/Hg. This coefficient is also influenced by cut-off rigidity because of geological factors such as latitude, longitude and altitude. It is also given from reports **(Mitrica, 2013)**, that correlation between count rate and atmospheric pressure from 27 Sep to 5 Oct. observed ranging from -0.1% to -0.2% mm/Hg for muon detector. It is initiated by means of linear correlation between intensity and atmospheric pressure.

Figure 12(a, b, c and d): Count rate dependence of detector coincidence as function of horizontal separation among the detectors in a room and at roof (10m height from room level).

Data taken during the period from 1-December-2014 to 16-September-2015

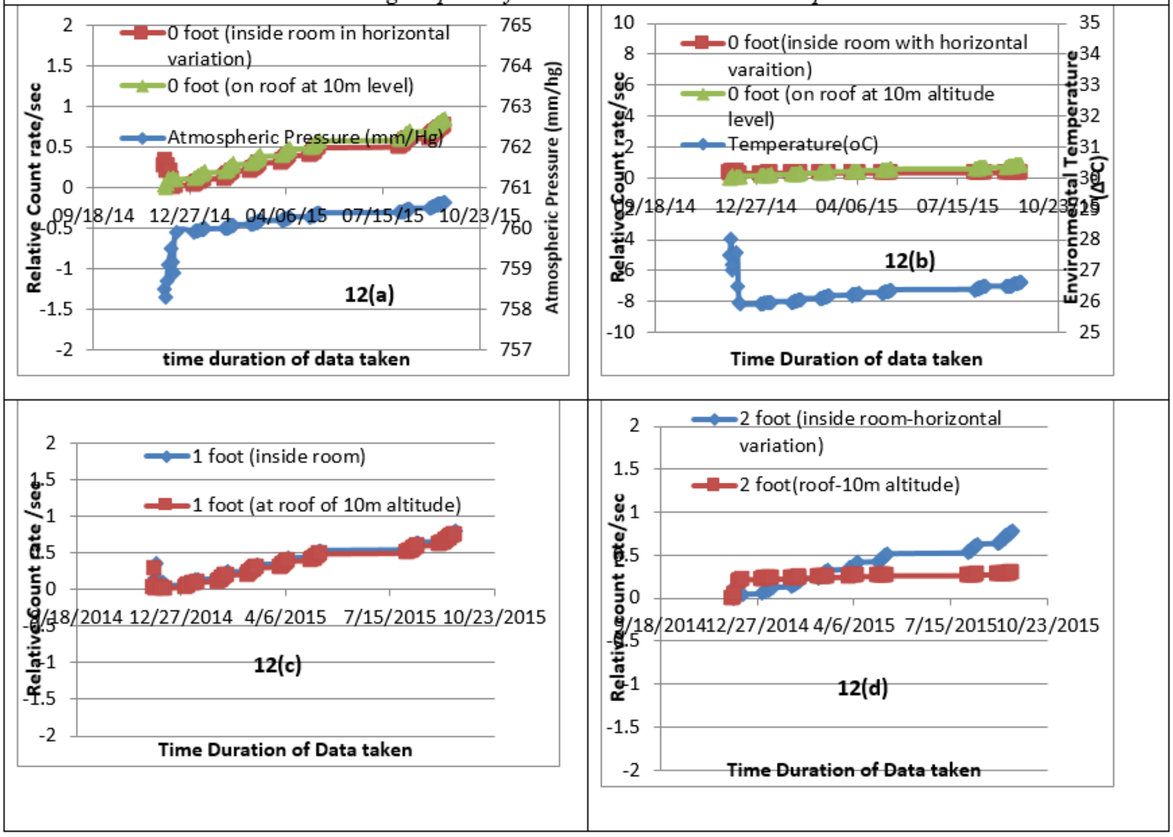

The count rate dependence on varying the detector distance horizontally is observed along with its effect on laboratory environmental factors and is also shown in figure 12 (a, b, c, d). It is observed that the count rate is less while compared to vertical separation due to less probability in existence of vertical slant muons while passing through both the detectors.

2.3 Summary

A versatile detector for cosmic ray mon flux measurements is setup and studied in this work. The concepts of scintillating, light collection and signal processing using Nuclear Instrumentation Methods (NIM) are discussed at a post graduate level by performing an educational activity. It is demonstrated by a good agreement from students feedback through a questionaire (Appendix I). The geomagnetic cutoff rigidity of primary source for particular location i.e. Agra (28.12^0 N latitude, 78.09^0 E longitude and 169 m altitude above the sea level). The effect on cutoff rigidity on varying the azimuthal ($0\text{-}360^0$) and zenith angle ($0\text{-}80^0$) is observed to be asymmetry from figure 1. The telescope is characterized on computing its solid angle and efficiency. In the present studies, for a detector area of 564 cm^2, the solid angle obtained is 0.15 radians and it is subjected to decrease exponentially from figure 3 on increasing the distance among the detectors. Further in Table 2, a correlation among muon intensity and differential energy spectrum is also computed to observe its change on varying distance among the detectors. The muon flux obtained from a coincidence rate is $9.16\pm0.31/cm^2$.str.sec. the efficiency of the telescope is further determined within 60-80%.

The muon flux measurements are also computed for the setup at different altitudes on varying the distance between them. The data is taken for a duration of 1 Dec. 2014 – 16 Sep. 2015. It is also an important application for estimation of water equivalent depth for different under ground locations to characterize the back ground rate for neutrino physics like SuperKamiokanda **(B´en´, 2013)**. The application also widens in use of muon tomography technique to search the hidden rooms in pyramids or in vocabulary. There are also many applications like the detection of unknown sources to increase safety procedures such as custom check posts, scanning in vehicle transport etc. The variation of muon flux with respect to temperature, pressure and humidity possibly direct us to a new path to understand the global climate warming trend. It could also indirectly impact the solar irradiance at ground level. This may leads to catastrophic weather, crop failures, disease outbreak and impact on plants, wild life and humans. Measurement of muon flux at different heights with change of distance in detectors helps to find the primary particle source information form the obtained decoherence curve.

Chapter 3

Study the lepton and gamma interactions in detector and to observe the effect of multiple scattering phenomena in Geant4 physics models based on QED approach

(This chapter is based on the following published papers)

- S.N.L Sirisha, Sonali Bhatnagar ***"Geant4: GATE and GAMOS – A systematic Implementation of HEP Simulation toolkit to oncology therapy",*** presented in ***"IEEE Student's technology Symposium – 2014"***, IIT Kharagpur, 28Feb-2March, 2014 organized by IEEE Student Branch, IIT Kharagpur and IEEE Kharagpur Section and published in IEEE Xplore, ISBN 978-1-4799-2608-4/14©2014 pp.25 – 30.

- Kajal Garg, S.N.L Sirisha, Sonali Bhatnagar ***"The energy spectrum and Rotational matrix based study of gamma rays",*** ICTCS '14 Proceedings of the 2014 International Conference on Information and Communication Technology for Competitive Strategies, Article No. 24 ACM, New York,USA ©2014 ISBN: 978-1-4503-3216-3 doi:10.1145/2677855.2677879.

- S.N.L Sirisha, Kajal Garg, Sonali Bhatnagar ***"Study the correlation of muon paddle efficiency with temperature, pressure, decoherence curve and effect of Multiple Scattering Physics in Geant4 based detector simulation" ,*** International Journal of Current Research Vol. 8, Issue, 09, pp.39537-39545, September, 2016.

3.1 Phenomenology of particle interactions

The standard model of elementary particles is a well-established theory on combination of electroweak and QCD based strong interactions **(Amaldi, 2014)**. The phenomena of electroweak and strong interactions are unified forming Grand Unified Theory (GUT) **(Most Revered P.S.Satsangi, 2016)**. The LHC experiments at CERN mainly focus on study of electroweak physics and quantum chromo dynamics at energies around electroweak scale (~100 GeV). The particle detection in these fields presents a challenge in finding the origin of highest energy cosmic rays, correlation with active galactic nuclei **(S.K Gupta, 2014)**. Particles and radiation can be detected through their interaction with matter. The main interactions of charged particles with matter are ionization and excitation. For relativistic particles, bremsstrahlung energy loss also must be considered. In case of photons, they undergo photoelectric effect, Compton scattering and pair production of electrons. The electrons produced in these photon interactions are observed through their ionization in the sensitive volume of the detector.

Monte Carlo simulations of the showers and detector are developed by the TOMUVOL (Tomography with Atmospheric Muon Volcanoes) **(K.Jourde, 2016)** collaboration. The atmospheric showers were simulated using GEANT4 to study the spatial distribution and energy spectrum of the muons **(Clarkson, 2014)**. The CMS (Compact Muon Solenoid, Switzerland) used a object oriented Geant4-based program to simulate the complete central CMS detector (over 1 million geometrical volumes) which utilizes the full set of electromagnetic and hadronic physics processes provided by Geant4 and detailed particle tracking **(Sonali Bhatnagar, 2014)**. A scintillation detector was simulated in Geant4 for study of physics processes that may affect the transport and collection of optical photons through it **(Clarkson, 2014)**. The processes such as ionization, direct production of electron, positron pairs, bremsstrahlung and inelastic muon interaction with nuclei which are studied for muon interactions with low-Z materials was discussed **(Cecchini, 2012)**. The properties of wavelength shifting fiber were studied which tends to decrease the self-absorption of detector to propagate maximum light that reaches the PMT as possible **(Riggi S, 2011)** .

The motivation behind the aim to study particle interactions in matter is a Monte-carlo simulation tool i.e. Geant4 – an application is a concept of Quantum field theory. It helps to study the models based on Quantum Electro Dynamics (QED) and Quantum Chromo Dynamics (QCD) phenomena which has an extended application for study of quantum unified theory approach. The contribution to differential cross-section of the muon interaction processes in relation to the relative energy transfer function is discussed in section 3.2. The effect on muon interaction length and total cross-section due to multiple scattering in high and low density materials also observed. The methodology of the simulation studies performed will be discussed in section 3.3. A muon paddle is simulated using Geant4.9.4.p04. In continuation of the work reported in the paper *(Sirisha et.al.2011)* , in section 3.4, the response of the telescope is observed for incident muon energy. The influence of various surfaces such as polished, etched, rough-cut surfaces for each individual reflector (Teflon tape, ESR film, Lumirror, TiO_2 paint and Tyvek paper) is observed w.r.t response of the muon telescope. In section 3.5, the phenomena of Compton scattering is discussed on varying the angle between a scatterer and a plastic scintillator corresponding to G4Rotational matrix of Geant4 simulation toolkit.

3.2 Analytical calculations of physical parameters based on QED models for study of muon interactions:

Muon detection is important due to its electromagnetic or weak interactions and produced from decay of Z, $W^{\pm}$ and heavy particles. The four basic processes of muon interactions that may lead to computer muon energy loss and for further decay into secondaries in matter are: ionization (including production of high energy knock-on electrons, or δ-rays), direct production of electron-positron pairs, bremsstrahlung, and inelastic muon interaction with nuclei. Since the main contribution is given by low-Q^2 region which is usually defined in terms of nuclear absorption of virtual photons, which is also called "photonuclear" muon interaction. Muons when passes through matter lose its energy due to excitation of bound electrons and by ionization. Excitation processes leads to low energy photons and are therefore useful for particle detectors studies. The muon scattering during interaction with matter also plays an important role for transfer of a certain amount of their energy to atomic electrons.

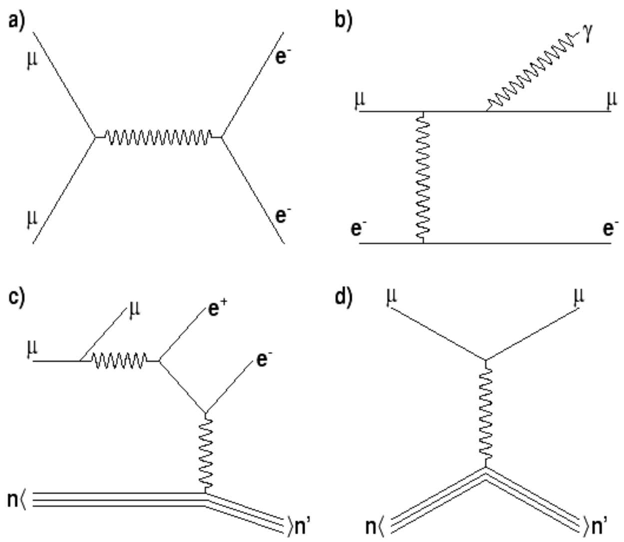

Figure 13(a,b,c,d): Muon Interaction Processes through Feynmann diagrams

[Ref:http://antares.in2p3.fr/users/bailey/thesis/html/node73.html]

The ionisation process is a continuous energy loss of muons passing through a medium as relatively low energy transfers to atomic electrons that ionize along the muon path in the material. The energy loss is calculated using the Bethe-Bloch formula and the basic process is shown in diagram (a) in Figure 13. In the electric field of a nucleus or atomic electrons, muons can radiate high energy photons as shown in Figure 13(b). A muon can radiate a virtual photon which, again in the electric field of a nucleus, can convert into a real pair. This process is shown in Figure 13(c). A muon can radiate a virtual photon which directly interacts with a nucleus in the muon propagation medium. It can be either and electromagnetic interaction or the fluctuation of the photon into a quark-antiquark pair (i.e. a virtual vector meson) which can be observed in Figure 13(d). The energy loss for heavy particles follows Bethe-Bloch equation where the average energy loss dE per length dx is given by

$$-\frac{dE}{dx} = 4\pi N_A r_e^2 m_e c^2 z^2 \frac{Z}{A}\frac{1}{\beta^2}\left(\ln\frac{2m_e c^2\gamma^2\beta^2}{I} - \beta^2 - \frac{\delta}{2}\right) \quad (16)$$

The energy loss decreases corresponding to ${}^{1}/_{\beta^2}$ in the low-energy domain and reaches a broad minimum of ionization near $\beta\gamma \approx 4$. There are also minimum-ionizing particles (MIPs) which are considered to be relativistic $\beta \approx 1$ corresponding to a minimum energy loss. The energy loss is approximately $-\,\mathrm{dE/dx}|_{\mathrm{min}} = 2\mathrm{MeV} - \mathrm{g/cm^2}$ with ratio of $\mathrm{Z/A} \approx 0.5$ for MIPs in light absorber materials. The energy loss by ionization and excitation for muons in iron is shown in Figure 14. At high energies, radiation losses become more and more important. Figure 15 shows the ionization energy loss for electrons, muons, pions, protons, deuterons and α particles in air **[James E, 2011]**.

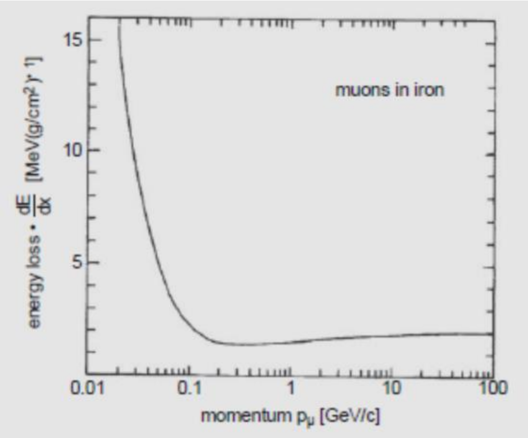

*Figure 14: Energy loss by ionization of muons in iron corresponding to its momentum **[PDG et.al, 2015]**.*

The equation (16) gives only the average energy loss of charged particles by ionization and excitation. For thin absorbers, the strong fluctuation exists around the average energy loss. The distribution is also strongly asymmetric for thin absorbers **[C.Grupen, 2012]**. This behavior can be parameterized by a Landau distribution.

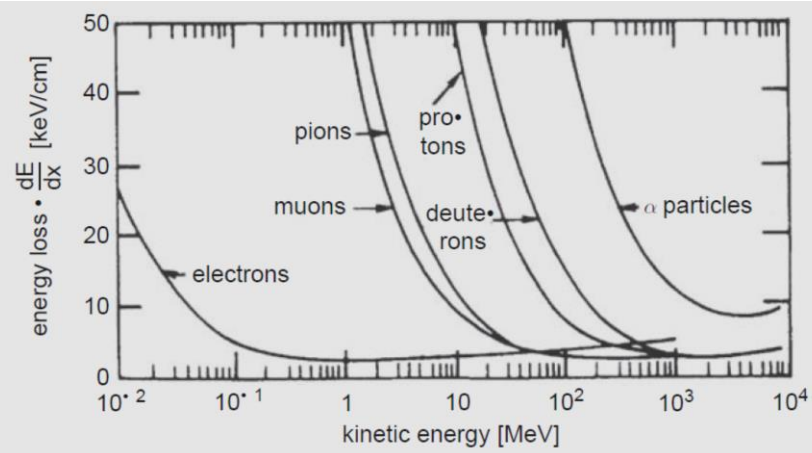

*Figure 15: Energy loss of various particle in a medium **[PDG, et.al, 2016]**.*

The approximation of this distribution is given by

$$L(\lambda) = \frac{1}{\sqrt{2\pi}} \exp\left[\frac{-1}{2}\left(\lambda + e^{-\lambda}\right)\right] \tag{17}$$

Here λ characteristics the deviation from most probable energy loss. The scattering of charged particles off atomic electrons when interacts with a material occur due to ionization process. The total cross-section is written as follows

$$\sigma(E,\varepsilon) = \sigma_{BB}\,(E,\varepsilon)\left[1 + \frac{\alpha}{2\pi}\ln\left(1 + \frac{2\varepsilon}{m_e}\right)\ln\left(\frac{4m_e E(E-\varepsilon)}{m_\mu^2(2\varepsilon + m_e)}\right)\right] \tag{18}$$

Where, $\sigma_{BB}\,(E,\varepsilon)$ is differential cross-sections, m_e is the electron mass, m_μ is muon mass, E is muon energy, α is constant (1/137.056), ε energy transfer ranges from (0.2 GeV to T_{max}), T_{max} $=1+m_\mu^2/E$.

Multiple Coulomb Scattering (MCS) also plays an important role for particle scattering and its energy loss. In contrast to this, the energy loss due to the ionization process is caused by collisions with atomic electrons. These processes are dominated by deflections in the coulomb field of nuclei. This leads to large number of scattering processes with very low deviations from original path. The distribution of scattering angles due to MCS is described by Moiler's theory **(Sonali Bhatnagar, 2014)**. For small scattering angles it is normally distributed around the average scattering angle $\theta = 0$. Larger scattering angles caused by collisions of charged particles with nuclei are, however, more frequent than expected from a Gaussian distribution. A charged particle emits a photon when its path is bent by the electric field of the nucleus. It can be considered as Compton scattering by a virtual photon (γ*) produced by the nucleus:

$$\gamma^*(q) + e(p_i) \rightarrow \gamma(k) C\, e(p_f) \tag{19}$$

When the charged muon is decelerated in Coulomb field of a nucleus, a fraction of its kinetic energy will be emitted in the form of real photons or bremsstrahlung radiation.

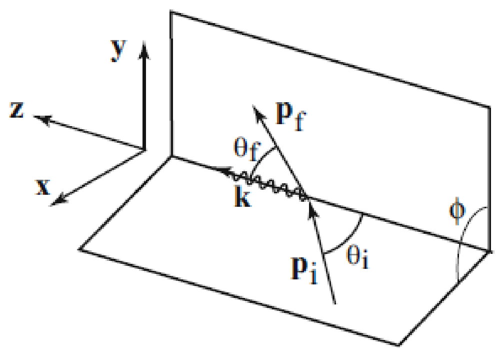

Figure 16: Diagrammatic representation of bremsstrahlung radiation in muon interactions. Here an emitted photon is in the z direction and electron is in the y–z plane. The incoming electron is in a plane rotated by angle φ from the y–z plane ***(Griffiths. D, 2008)***

The differential cross-section for muon bremsstrahlung (in units of cm^2/g) can be written as:

$$\frac{d\sigma(E,\varepsilon,Z,A)}{d\varepsilon} = \frac{16}{3}\alpha N_A \left(\frac{m}{\mu} r_e\right)^2 \frac{1}{\varepsilon A} Z(Z\phi_n + \phi_e)(1 - \nu + \frac{3}{4}\nu^2) \quad (20)$$

μ and m are the muon and electron masses, Z and A are atomic number and atomic weight of the material, N_A is Avogadro's number. The required terms i.e. contribution of nucleus (ϕ_n) and of electrons (ϕ_e) can be obtained from the Physics Reference Manual (G49.4.p04, 2012). ε is energy transfer ranges from 0.00204 GeV to 38.51 GeV. Here ν = ε/E is relative energy transfer.

The energy loss of heavy charged particles can be calculated from

$$\frac{dE}{dX} = -4\alpha N_A \frac{Z^2}{A} z^2 r^2 E ln\left(\frac{183}{Z^{1/3}}\right) \quad (21)$$

Where, $r = \frac{1}{4\pi\varepsilon_0}\frac{e^2}{mc^2}$. It is dominant process over all when compared with other muon interaction processes and its cross-section exceeds over a range of energy transfer between 100 MeV and 10 PeV. The average energy loss increases linearly with muon energy. The spectrum of total energy of directly produced e^-, e^+ pairs at high energy transfers is steeper than the spectrum of bremsstrahlung photon. The differential cross-section formula for muon pair production is:

$$\sigma(Z,A,E,\varepsilon) = \frac{4}{3\pi}\frac{Z(Z+\xi)}{A}N_A(\alpha r_0)^2\frac{1-\nu}{\varepsilon}\int_0^{\rho_{max}} G(Z,E,\nu,\rho)d\rho \tag{22}$$

Where $G(Z,E,\nu,\rho) = \phi_e + \left(\frac{m}{\mu}\right)^2 \phi_\mu$ and $\phi_{e,\mu} = B_{e,\mu}L'_{e,\mu}$

The energy loss of muon pair production follows the mathematical rule:

$$\frac{dE}{dX} = \int_{\varepsilon_{min}}^{\varepsilon_{cut}} \varepsilon\sigma(E,\varepsilon)d\varepsilon \tag{23}$$

Where, $\varepsilon_{cut} = 1+\mu/E$, μ is muon mass, and E is incident particle energy.

Charged particles can interact in elastically via virtual gauge particles with nuclei of the absorber material, there by undergoes energy loss via (nuclear interactions). This results in a proportional relationship to the particles energy

$$-\,\mathrm{dE/dx}|_{\mathrm{photonucl.}} = \mathrm{b_{nucl}(Z,A,E).\,E} \tag{24}$$

Nuclear interactions are also responsible for hadron cascade

$$\sigma(E,\nu) = \psi(\nu)\phi(E,\nu) \tag{25}$$

The relative terms i.e. $\psi(\nu), \phi(E,\nu)$ are reported in the Physics Reference Manual (G4 9.4.p04, 2012) and the energy transfer, ν ranges from 0.2 GeV to E-M/2 , E is kinetic energy of incident particle.

The contribution to differential cross-section of the muon interaction processes studied in relation to the relative energy transfer is shown in Figure 17[a], [b]. The calculations are performed analytically using Matlab 7.1. The study is performed initially to understand the muon interaction phenomena with the materials polystyrene and iron which are used in the detector setup.

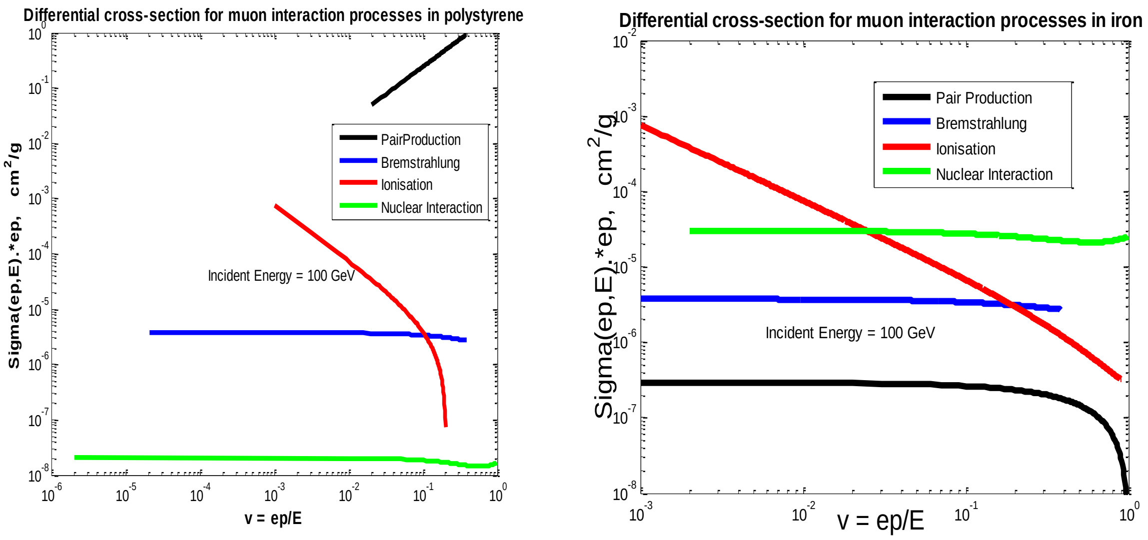

Figure 17[a], [b]: Muon Differential Interaction Cross-section in Polystyrene and Iron.

At moderate muon energy i.e. at E=100GeV, the main interaction process in both iron and polystyrene materials is production of knock-on electrons. But when we consider at high energies (E=10 TeV), the production of neutral particles and hadronic cascade is dominant in case of polystyrene, where as in case of iron the electron pair production is dominant process during muon interaction. The result for differential cross-section of muon interaction in iron is also comparable with the literature et.al **A.G Bogdanov, 2004**.

Two principle features mainly distinguishes the passage of charged particles i.e. a) energy loss by the particle and b) deflection of the particle from its incident direction. Inelastic collisions are mostly responsible for energy loss of heavy charged particles in matter. The energy transferred in each collision is small in fraction of particle's kinetic energy. When charged particle enters through a dense material, the number of collisions per unit length is so large that a subsequent cumulative energy loss is observed even in thin layers resulting in ionization process. The range of muon bremsstrahlung, electron pair production by muons and of inelastic muon interaction with nuclei corresponds to relative energy transfer can be represented as

$$\varepsilon\sigma\,(E, \varepsilon) = v\sigma\,(E, v) = f\,(v) \qquad (26)$$

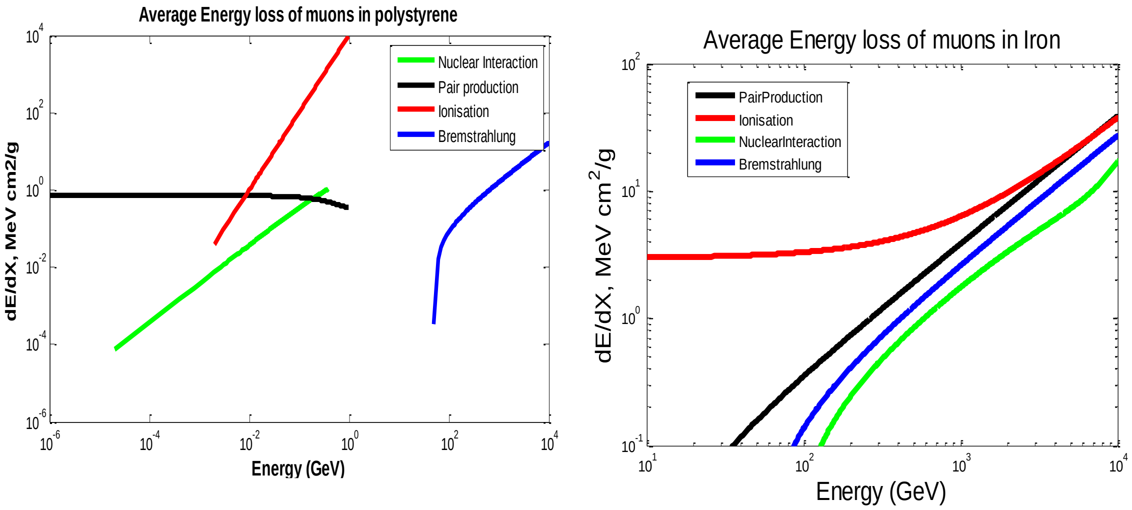

Figure 18[a], [b]: Average energy loss of muon in polystyrene and iron.

Consequently the muon energy loss associated with these processes varies linearly with muon energy as shown in Figure 18[a], [b]. It is to be observed that bremsstrahlung process gets suppressed due to mass of muon. The electron pair-production and bremsstrahlung processes increases as function of muon energy in case of iron and are dominant in case of higher energies lead to expansion of muon calorimeters. For polystyrene material, the proportionality of energy loss w.r.t muon energy in case of bremsstrahlung process is very less comparable to iron.

3.3 Methodology

The muon telescope was simulated using Geant4 toolkit. The purpose of this simulation was to better understand the interaction mechanism and phenomena of multiple scattering of muons in different material densities. The entire program is executed with required modification in an application of extended category i.e."TestEm17" of Geant4.9.4.p04. In the following subsections i.e. from 3.3.1 to 3.3.5, the structure of the Geant4 coding while simulating a detector required in the present study is discussed. The procedure mainly deals with Geant4 Run Manager which controls the simulation through user initialization classes and action classes for acquiring a desirable output.

3.3.1 Run manager

The Run Manager is a main source file which uses different object types in terms of header and implementation files. The header files have an extension of '.hh' and are stored in '/include' directory whereas implementation files have extension '.cc' are stores in '/src' directory. All these files under goes initialization and action classes. The former is used to customize the user requirements such as geometry, particle kinematics and physics. The latter is used to perform the run and event processing, verbosity to control the primary and secondary tracking in detector.

code - 1

```
#include Particle.hh
#include Detector.hh
 int main()
{
 Particle Electron;
Electron.SetMass(0.51);
int echarge = Electron.GetCharge();
 // some other commands
 return 0;
}
```

A function begins with its type, name and arguments, e.g.
int main()

Figure 19: G4RunManager Class

The commands follow braces {} that follow the enclosed function. We can define the 'body' of the main ( ) method within the braces. We should also define some 'include statements', which connects the classes. The class is same as the name of the header file and also implementation file in which the user can do their coding. For example, the Particle class is coded in the files /include/Particle.hh and /src/Particle.cc.

3.3.2 Detector construction*:*

The geometry and the materials of the detector are defined in a XXXDetectorConstruction class file i.e. /include/XXXDetectorConstruction.hh and /src/XXXDetectorConstruction.cc (here XXX is a prefix that requires the main program). In order to run a simulation with Geant4, one has to do the following:

1. While programming in detector construction class, we should remember mainly about 'volume'. They can be parameterized within a larger volume which is called the 'world volume'. Each volume required to be defined by its geometrical shape, dimensions, position and material.
2. While defining material concept, we need to state elements or compounds which are required for simulation. The G4Element class describes the following properties of an element: atomic number, number of nucleons, atomic mass, etc. The G4Material class defines a material by its macroscopic properties: density, state, temperature, pressure, etc.
3. Specify the physics of particles and their respective processes which are included in the simulation.
4. Outline the beam function for particle generation.
5. Initiate the program with certain actions that should be taken during the simulation (user action classes).

Steps 1 and 2 can be achieved by modifying the geometry and through material selection even after the program is compiled. The definitions in steps 3 and 5 can be only changed in terms of batch code (i.e. before the program is compiled). The beam is usually defined by compilation (for a program which is run interactively, as will be the case in the exercises that follow).

The structure code implementation in G4Detector Construction is shown here:

a. define atomic mass and atomic number
b. define elements *eg: H = new G4Element("h", "H", z=1, a=1.01*g/mole);*
c. define materials

```
code - 2
define atomic mass and atomic number
define elements eg: H = new G4Element( "h", "H", z=1, a=1.01*g/mole);
define materials
eg: Pstyrene = new Material("Polystyrene", density=1.03*g/cm3, 2);
    Pstyrene = AddElement (C,8);
    Pstyrene = AddElement (H,8);
```

Figure 20: G4 Material Class

d. add material properties i.e. define refractive index, absorption length, scintillation fast time component, scintillation yield, resolution scale, fast time constant and birk's constant **(Geant4 User manual, 2015)**.

e. now construct the volume we need i.e. logical and physical volumes which are further visualized using an interface of geant4.

```
code- 3
eg:exp_log = new G4logical Volume (box, Vacuum, "log", 0,0,0)
   exp_phy = new G4PVPacement(0, ThreeVecotr(0,0,0), exp_log,
                              "Hall", 0, false, 0)
it is further visualized by defining as
 exp_log->set VisAttributes (G4VisAtt:Invisible)
```

Figure 21: G4Detector Construction Class

f. Now set the surface properties

```
code-4
eg:G4OpticalSurface ScintWrap = new G4OpticalSurface ("ScintWrap")
```

Figure 22: G4Surface Property Class

here we need a logical border surface for which we set its type of wrapping as dielectric_dielectric (or) dielectric_metal with polished surface finishing. The entire feature corresponds to glisur/unified model.

The detail description of these parameters is given in paper **(Sirisha, 2011)**. Now the detector which is constructed can be visualized by a G4interafce in the form of OpenGL/HepRep driver. To initialize this phase, the following steps should be defined in a macro file.

```
code-5
/vis/scenehandler/create
/vis/viewer/create
Create for OGLIX driver
/vis/viewer/set/style wireframe
/vis/viewer/set/viewpointvector 1 1.5 1.1
/vis/viewer/set/viewpoint/ThetaPhi       90 180 deg
/vis/viewer/zoom 1.4
Now create an empty space and add the detector
geometry
/vis/scene/create
/vis/scene/add/geometry
Creat an empty space and add detector geometry
/vis/drawVolume
```

Figure 23: Visualization Macro

The detector geometry can also be controlled via Messenger class i.e. it is shown in Table 4

Table 4: Set command description and their function	
1. Detector geometry	*/Pwls/detector*
2. Enable/Disable Volumes	*/Pwls/detector/volume*
3. Set dimensions of detector	*/Pwls/detector/dimensions scint_x,scint_y,scinti_z*
4. Set thickness of housing	*/Pwls/detector/housingthickness*
5. Set reflectivity of housing	*/Pwls/detector/reflectivity*
6. Number of WLS fibers in slab	*/Pwls/detector/nfibers*
7. Set scint_yield of volume	*/Pwls/detector/MainscintYield*

A box with dimensions of 24x23.5x2 cm^3 is constructed. It is assigned with material properties of different densities such as hydrogen, carbon, polystyrene and iron. Now place the detector in a coordinate system of mother volume. The bulk material properties of polystyrene with its elemental composition of hydrogen and carbon were defined. Scintillation yield is one of the important optical properties of the polystyrene. This can be adjustable using G4UImessenger class. The yield of polystyrene based plastic scintillator is 100 photon/MeV deposited energy **(P.K Mohanty, 2014)**. The simulated plastic scintillator is shown in figure 24:

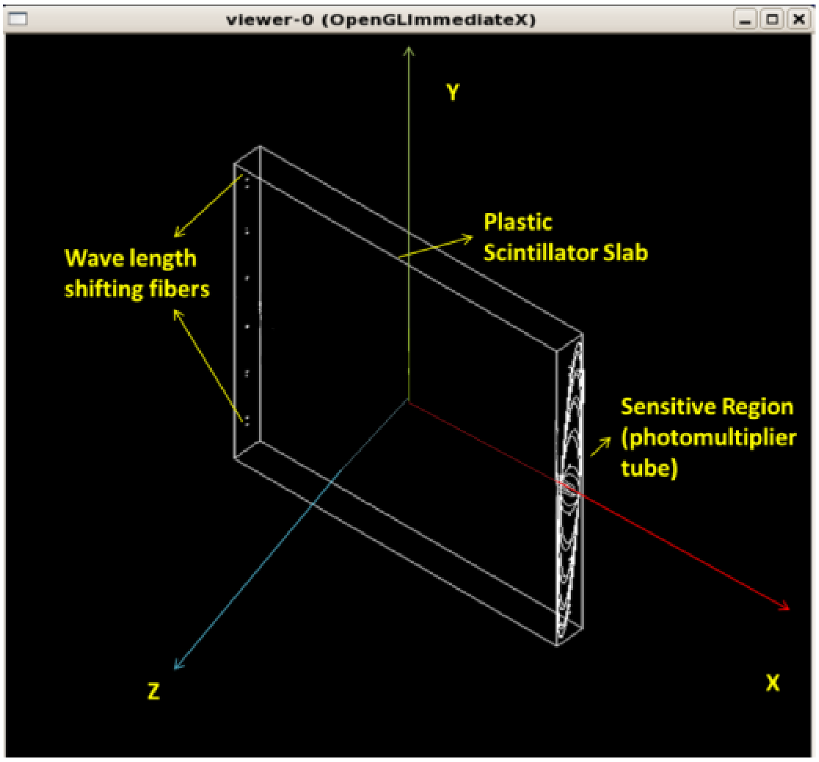

Figure 24: Plastic Scintillator designed using Geant4

The detail description of the parameters is given in paper **(Sirisha, 2011)**. The characteristic light yield i.e. SCINTILLATIONYIELD, and an intrinsic resolution i.e. RESOLUTIONSCALE are defined in program which generally broadens the statistical distribution of generated photons. The relative fast time component as fraction of total scintillation yield is given by the YIELDRATIO. Scintillation process can be executed by stating these practical constraints for each material. A relative spectral distribution as a function of photon energy for the scintillating material is defined in the Detector Construction class. The optical boundary processes are based on the concept of surface and its needs to be implemented in the form of border surface used for physical volume and skin surfaces used for logical volume of the geometry. There are also various surface properties along with interfacings such as

Table 5: Models for surface characteristics

Model	Surfaces	Interfacing
Unified	Polished, Etched, Ground	dielectric_metal, dielectric_dielectric

The UNIFIED model **(Sirisha, 2014)** provides a range of different reflection mechanisms such as specular lobe constant which represents the reflection probability about the normal of a micro facet, specular spike constant that illustrates the probability of reflection about the average surface normal.

A sensitive detector is implemented in G4UserSteppingAction class to count the number of photons emitted from the scintillator that hit the photocathode of the PMT. Initially the scintillator logical volume acts as a sensitive detector which yields the total energy deposited and the average position of the hit. The sensitive detector then stores the obtained values using G4VHit hits collection class. For each photon that arrives at sensitive region of PMT, the program stores the following parameters to G4UserActionClasses: the photocathode hits, number of reflections and absorptions it undergone at boundary surface of detector. The detection efficiency of the PMT photocathode is defined in terms of “quantum efficiency and “wavelength” of incident photons for a realistic case of PMT.

3.3.3 Primary generator:

The second significant extension of Geant4 capability is to define the necessary volumes in an experimental setup and also different particle production threshold in each region for their characterization (for eg: a muon detector with a layer of germanium detector that wraps the volume). This feature helps in improving the accuracy in simulation for high resolution detector that helps to save time while computing. The user can also efficiently generate charged particle propagation within a field that is associated with geometrical volume. The General Particle Source is a subsystem of Primary Generator Action class has a feasible functionality to implement the particle distribution in terms of x-, y-, z- direction.

The primary generator action class mainly deals with particle gun or particle general source where we can define it energy, position and momentum

```
eg:  particle Gun -> SetParticleDefinition ("mu-")'
                        Set ParticleENergy (110*MeV)
   Set ParticlePosition (G4ThreeVector(0,0,-3*cm)
    Set Momentum (G4ThreeVector(0,0,1))
The function of the primary generation can also be defined at the
beginning of the event as follows:
G4double Halfsize = 0.5*(detector->GetSize())
The beam can be randomized further in relative to its coordinates i.e.
      G4double Xo = -halfSize
G4double beam = 0.8*halfsize
      G4double Yo = 2*Xo
      G4double Zo = 2*Yo
```

Figure 25: G4Particle Source Class

The function of the beam is distinct in the main program or in.mac file. In the exercises, we will use the latter. The following commands are available

```
code- 7
Command /gun/List
Guidance: lists available particles.
 Command /gun/particle
Guidance: sets particle to be generated.
Candidates: proton, neutron, gamma, e-.

Command /gun/energy
Guidance : sets kinetic energy.
Candidates for the unit: eV, keV, MeV.

Command /gun/position x y z
Guidance: sets starting position of the particle.
Default value for unit: cm
Candidates: m, cm, mm, µm, nm, angstrom, fermi

Command /gun/number N
Guidance: sets the number of particles to be generated.
Range of parameters: N>0

In order to run for an ion beam, we have to give the following commands
/gun/particle ion
/gun/ion Z A Q
where Z is the atomic number, A is the number of nucleons and Q is the charge of the ion.
```

Figure 26: Particle Gun Macro Commands

3.3.4 Physics list:

There are abundant functionalities that are available in Geant4 “Physics List” to define the electromagnetic and hadronic processes **(Geant4 Physics Reference manual, 2015)**. A separate G4VPhysicsConstructor is used to define the optical physics in a module i.e. G4OpticalPhoton class. It includes the following processes: scintillation, Cerenkov, optical absorption, optical Rayleigh scattering and optical boundary processes.

In the physics list implementation class we need to define the necessary physics models, particle definitions and their tracking nature.

```
                         code- 8
Define the cut value
Current default cut value = 1.0 * mm
Physics models
emName = G4String (“standard”)
emPhysicsList = new PhysicsList Emstandard
Construct the particle
G4leptonconstructor     pLeptonConstruct
pLepton Constructor     Construct Particle ()
Construct process
Transportation: Add transportation ()
Add physics list
if(verbose level > 1) {
G4cout << “Physics List :: AddPhysicsList
                        < “<<name>>”> <<G4end
if(name = = “standard” && name 1 = emName)
Set cuts for gamma, e-, e+
Set cut value (cut for gamma, “gamma”)
Now construct the em interactions of mu-
Particle = G4MuonMinus :: MuonMinus();
pManager = particle -> GetProcessManager
pManager = AddProcess (new G4MultipleScattering (-1,1,1))
pManager = AddProcess (new G4MuIonisation (-1,2,2))
pManager = AddProcess (new G4MuBremstrahlung (-1,3,3))
pManager = AddProcess (new G4MuPairproduction (-1,4,4))
```

Figure 27: G4Physics Class

The muon interaction processes are simulated by implementing the necessary physics classes i.e. G4MuIonization (deals with ionization process), i.e. it provides the continuous energy loss due to ionization and simulates the discrete part of ionization i.e. delta rays produced by muons. G4Bremstrahlung dominated the other muon interaction processes in the region of catastrophic collisions ($\nu \geq 0.1$) i.e. at moderate muon energies above the kinematic limit for knock-on electron production. At ($E \geq 1$TeV) this process contributes about 40% of muon energy loss. G4MuPairProduction is one of the most important processes. At TeV muon energies, the pair production cross-section exceeds over an energy transfer range 100 MeV – 0.1 E_{μ} **(Geant4 Physics Reference Manual, 2015)**. The G4MuPhotoNuclearInteraction is important at high muon energies ($E \geq 10$GeV) and at relatively high energy transfer. The following models are used for the process :

Table 6: Muon High Energy Physics Ionisation Models

Model	Energy Range
G4BraggModel	T < 0.2 MeV
G4BetherBlochModel	0.2 MeV < T < 1 GeV
G4MuBetherBlochModel	T > 1GeV

As a next step in this simulation study, we intended to observe the effect of multiple scattering w.r.t muon interactions in different density materials. The Multiple Coulomb Scattering (MCS) model used in GEANT4 uses the Lewis theory to simulate the transport of charged particles. In this approach model functions are used to sample the spatial and angle distributions after a step, the theory gives constraints for these model functions (the model functions should give the same moments of the distributions then the theory).The details of the MSC model can be found in the GEANT4 Physics Reference Manual. The physics model “Wentzel VI” of G4Physics List is also included along with electromagnetic interactions in present study for accurate simulation of muons and determining the energy loss in matter. This mainly helps in implementing the multiple scattering physics and also tests the scattering angle and the tangential displacement of a particle in each step.

Steps of MSC algorithm (are essentially the same for many condensed simulations):

1. Selection of step length ⇐= physics processes + geometry (MSC performs the $t \Longleftrightarrow l$ transformations only)

2. Transport to the initial direction: (not MSC business)

3. Illustration of scattering angle θ

4. Work out on lateral displacement in order to relocate particle

The visualization of muon interaction is viewed using HepRep Visualization Driver of Geant4.

Figure 28(a-h): Visualization of Muon Interaction with different density materials on including Multiple Scattering Physics

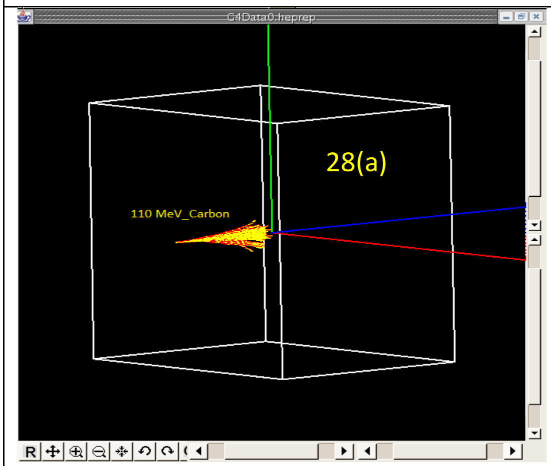

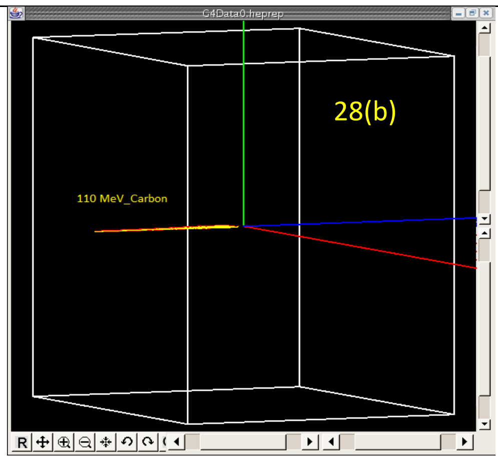

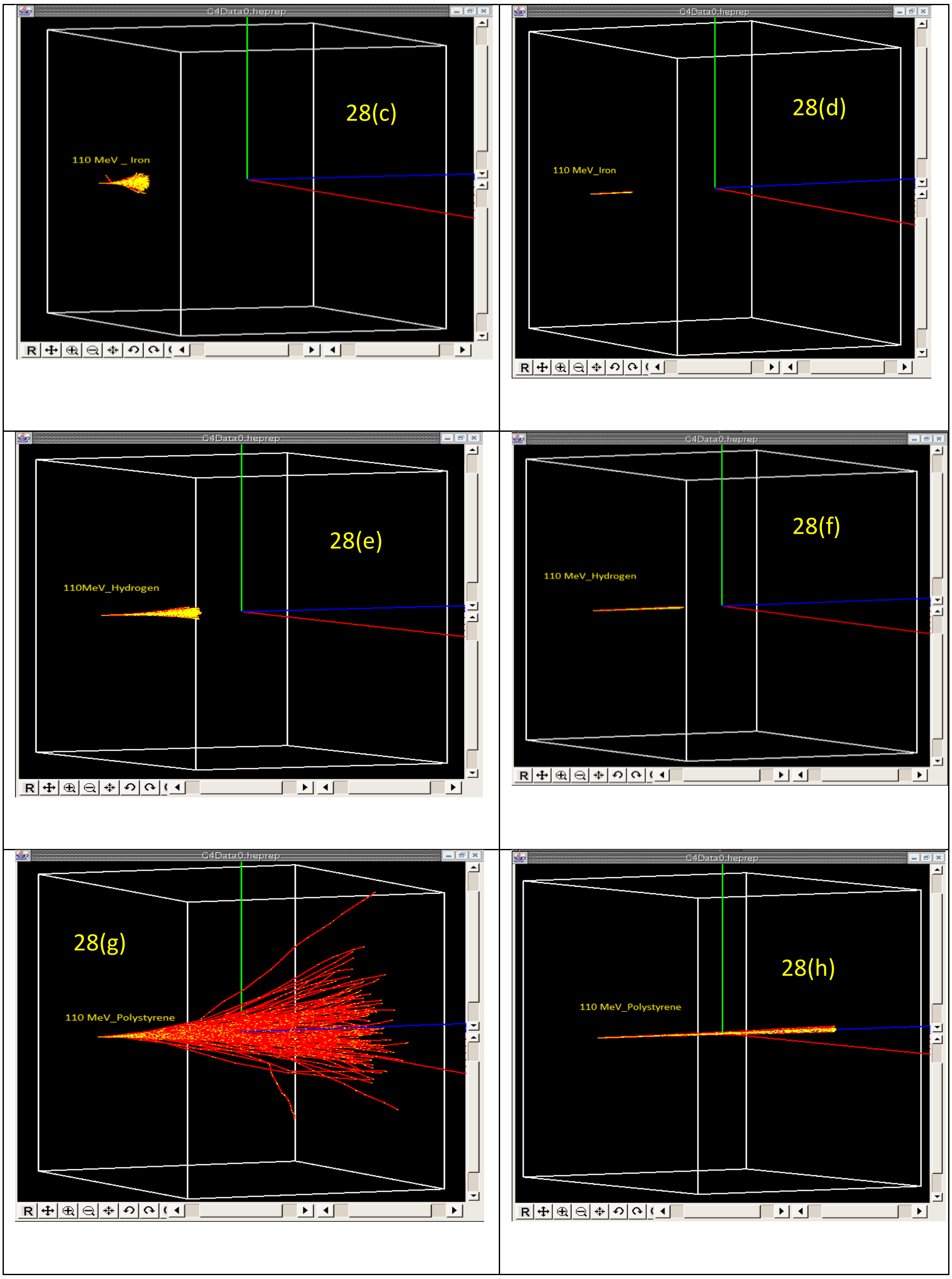

In figure 28(a-h) shown earlier, we can observe the muon scattering in with and without implementation of MCS physics for different material densities such as carbon, hydrogen, iron and polystyrene. The scattering of the muon in materials can be clearly seen in figures 28 (a,c,e and g) on including multiple scattering while compared to the cases in figure 28 (b,d,f and h) where the multiple scattering is not considered. The effect of MCS on total cross-section and interaction length of muon w.r.t different density material is also studied. The study is conducted by observing the dependence of total cross-section and interaction length as function of incident muon energy. This is shown in figure 29 and table 7.

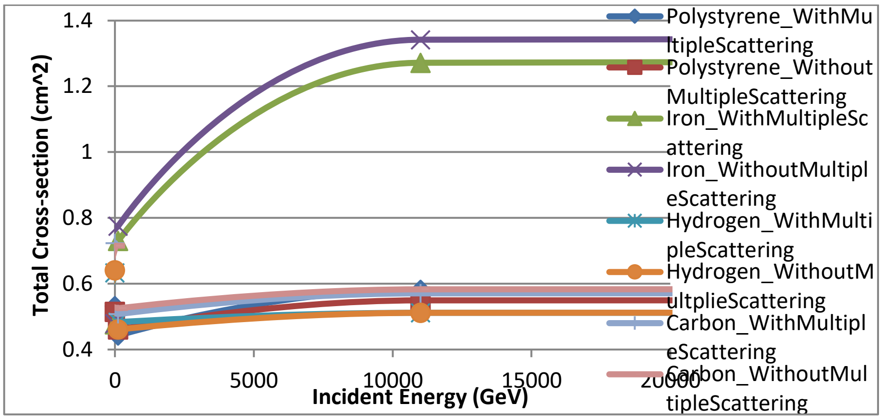

Figure 29: Effect of Multiple Scattering on Total Cross-section w.r.t Muon Incident Energy

Table 7: Effect of Multiple Scattering on Interaction Length w.r.t Muon Incident Energy

Energy (GeV)	*Polystyrene*		*Iron*		*Hydrogen*		*Carbon*	
	With Multiple Scattering	*Without Multiple Scattering*	*With Multiple Scattering*	*Without Multiple Scattering*	*With Multiple Scattering*	*Without Multiple Scattering*	*With Multiple Scattering*	*Without Multiple Scattering*
0.011	0.53	0.51	0.47	0.47	0.63	0.64	0.72	0.71
0.1	0.44	0.46	0.73	0.77	0.48	0.46	0.50	0.52
1.1	0.58	0.54	1.27	1.34	0.51	0.51	0.57	0.58
11	0.49	0.47	0.95	0.93	0.49	0.51	0.53	0.55

3.3.5 User actions (run, event, track):

There are also further advanced techniques which are defined in User Action Classes. The particle tracking is developed within the stepping action class to improve the performance of CPU. It doesn't depend on the particle type or specific physics processes. It is categorized as at rest, energy loss of primary, secondary production due to decay or interaction. The status of the simulation is also performed at three levels i.e. run, event and track. A 'run' is a simulation that includes a certain number of events. These are begin and end of event action in each step i.e.

```
code - 9
void RunAction::Begin of RunAction
{
}
void RunAction::End of RunAction
{
}
```

Figure 30: G4RunAction class

An 'event' is an interaction between particle beam and the detector which includes the primary and secondary particle production that may be obtained from a reaction. Here in this code we will collect the photons emitted during scintillation process and also hit the PMT base.

```
code - 10
void PwlsEventAction :: Begin of EventAction (const. G4Event* anEvent)
{
G4SDManager * SDman = G4SD manager :GetSDMpointer();
if (scintiCollID < 0)
Scint CollID = SDman -> GetCollection ID ("scintcollection")
Pmt CollID = SDman -> GetCollectionID ("pmtcollection")
void Pwls EventAction ::End of EventAction(const. G4Event* anEvent)
{
G4TrajectoryCounter * trajectory Container = anEvent ->
GetTrajectoryCounts();
G4int n_trajectories = 0;
if (trajectory Container) n_trajectories = trajectoryContainer -> entries ( );
}
```

Figure 31: G4EventAction Class

- Scintillation Hit Collection (SHC): it is implemented by initially gathering the information of hits in scintillator and the energy deposition obtained after each particle tracking.

```
code - 11
Edep = (*SHC) [i] -> GetEdep (); // hits in scintillator
Event Information -> IncEdep(edep)
If (edep > edepMax)
edepMax = edep;          // to store maximum energy deposited
```

Figure 32: G4HitCollection Class

- PMT hit collection (PHC): the reconstructed position of photons that hit the PMT will be collected along with its respective fraction of photons

```
for G4int(i=0; i<pmts; i++)
event information -> IncHitCount ((*PHC[i] -> GetPhotonCount())
```

Figure 33: G4PMT Hits Collection Class

The kernel also provides various ways to control the order of particle tracks. The event information can also be stored in a file to observe the interactions for each particle and its energy lost by it during tracking in field. To obtain the information in detail, it can be set through verbosities of each run, event and tracking. It can be defined in the following manner in a macro file

```
/run/verbose 1
/event/verbose 1
/tracking/verbose 1
```

Figure 34: G4Verbose Macro commands

Here these commands generate the required information of track / step for each particle at three levels in the simulation. The G4Track in the kernel keeps the information of the particle such as energy, momentum, position, time, mass, charge, life etc. it keeps the information at the beginning of the step while AlongStepDoit is invoked for the step in progress. It is further updated after each invocation of post step do it.

```
code-14
void PwlsTrackingAction :: PreUserTrackingAction
{
fpTrackingManager -> StoreTrajectory
                    -> Set trajectory (new Pwls trajectory)
                    -> SetUserTrackInformation
It is only relevant to the photons. Now create the tracking process:
Void LXeTrackingAction :: G4OpticalPhotons :
OpticalPhotonDefinition ( ))
```

Figure 35: G4Tracking Action Class

It is only relevant to the photons. Now create the tracking process:

Void LXeTrackingAction :: G4OpticalPhotons : OpticalPhotonDefinition ( ))

Now construct the wave length shifting process for photon trajectory information. G4step stores the transient information of a step. This includes the two end points of the step, presteppoint and poststeppoint which contains the coordinates and the volumes. It also stores the change in track properties such as energy and momentum. G4Tracking Manager acts as an interface between event, track and tracking categories. It aggregates the pointer to G4Steppingmanager, G4trajectory, G4TrackingAction while stepping manager takes care of the information relevant to particle interactions with matter. The tracking of the particle in each volume is defined as:

```
code - 15
G4StepPoint *Prepoint = step -> PreStepPoint();
PhysicalVolume *PrePV = GetPhysicalVolume()
Similarly the structure is implemented for PostStep. Now the boundary
process is obtained by implementation of the following code:
for (i=0; i<nprocesses; i++)
{
if ((*pv) [i] -> GetProcessName() = = "OpBoundary")
{
Boundary = (G4OpBoundaryProcess)(*pv) [i];
break;
}
```

Figure 36: G4SteppingAction Class

Now we should obtain certain conditions while tracking particle within the detector volume. This includes:

```
code - 16
Optical Photon definition i.e. if(particle type = = optical)
Track the photon in WLS slab.
If (the PrePV -> GetName() = = 'Slab')
Kill photons that enter the experimental hall other than the detector region
else if(the PostPV -> GetName = = exp_Hall
        the track -> setTrackStatus ();
Photon absorbed with in the process
If (post pt -> Get StepStatus( ) = = f Geom Bound)
Absorption: track the status and get the event information
Detection: now trigger the sensitive region of detector since the photon is absorbed
Get process hits( )
```

Figure 37: G4photon Absorption Physics

The hits and digitization are further recorded where the paths of primaries get verified for each event. The biasing techniques are used in order to facilitate the usage of variance reduction methods which are applicable in radiation shielding studies results to obtain high gain efficiency. For each run, the whole event processing is customized by a run action class where for each begin of run, a histogram can be defined and it stores at the end of each run. They are further analyzed with the help of analysis tool i.e. ROOT which is an interface in analysis manager. It is implemented in the following manner:

```
code - 17
Define root histogram
ITreeFactory* treefact -> create TreeFactory ( );
std::string filename = "wls.root"
the Tree = treefact -> create (filename, "root", false, true);
delete tree fact;
hist fact = afact->Create Histogram ( );
Define the parameters that to be stored
void PwlsAnalysisManager :: book ()
{
h1= histfact -> CreateHistogram 1D ("10", "EnergyDep(MeV)", 500,0,5)
here we define the histoID, histoname, bins, number, xmin, xmax)
The obtained data to fill the histogram
if (i = = 1)
 h1-> fill (f);
Now write the histogram to a file i.e.
the tree -> commit ( );
```

Figure 38: G4Histomanager class

3.4 Muon telescope simulation and to observe the effect of surface characteristics on photon yield in Geant4:

There is an exponential decrease w.r.t muon interaction length corresponding to the incident energy of muon. While total cross-section has a linear increase w.r.t energy of muon. But after a certain cut-off region of muon energy at 12E-11 eV, it is observed that both the parameters remain constant. The significant energy loss of relativistic muon is independent of the energy of the muon as per the Bethe-Bloch formula. It is relative to the thickness of the scintillator. There is also large variation of energy loss from muon to muon which is illustrated by Landau distribution. The precise energy loss meant for any given matter and particle rate:

$$\Delta E = \xi \left[\boldsymbol{\lambda} + \ln\left(\frac{5.5967.7 \times 10^{9} \beta^{2}}{(1-\beta^{2}) Z^{2}} \xi \right) \right] + 1 - \beta^{2} - \gamma_{E} \tag{26}$$

$$\text{Where } \xi = \left(\frac{0.1536}{\beta^{2}} \right) \left(\frac{Z}{A} \right) S \ \mathrm{gm/cm^{2}}$$

Z and A are the atomic and mass number of material. S is the mass thickness of material and γ_E is Euler's constant = 0.577. Here a polystyrene based plastic scintillator material is considered for an influential muon energy threshold where it can start interacting with material. So, A = 104, Z = 56, S = 1.03 gm. /cm^2 and β^2 = 0.9934 for 4 GeV muon. Thus a 4 GeV muon with velocity 0.99c when passes through a polystyrene losses an energy of 2 MeV. The mean rest mass energy of muon is 105.7 MeV. In this study, the muon energy threshold is determined by considering two factors i.e. rest mass energy and mean energy loss of muon i.e. $E_{threshold}$ = 110 MeV.

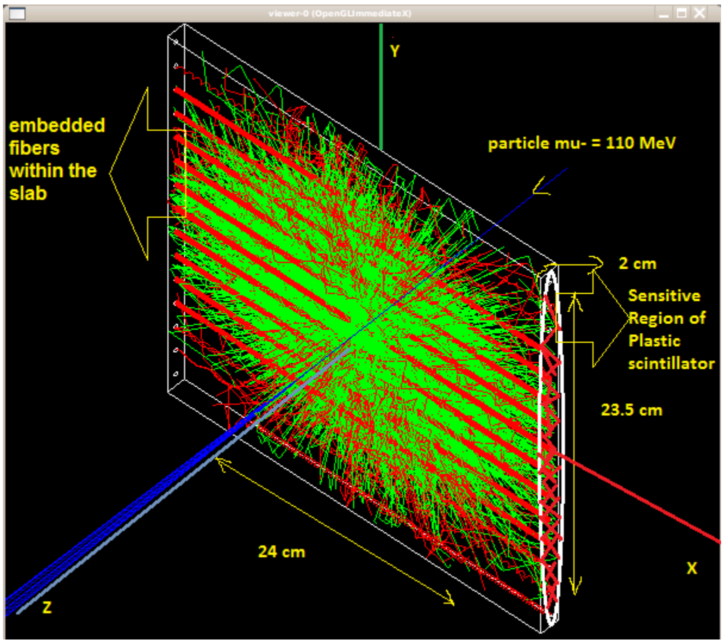

Figure 39: Response of Muon telescope for a muon of incident energy 110 MeV.

The detector simulated while muon interacting with it is shown in figure 39. The energy deposited in detector w.r.t incident muon energy is observed as shown in figure 40 given below. The average light yield is observed to have a linear dependence on the energy deposition of muon. But this may differ in case of non-minimum ionizing particle (MIP) whereas it is vice versa in case of muon.

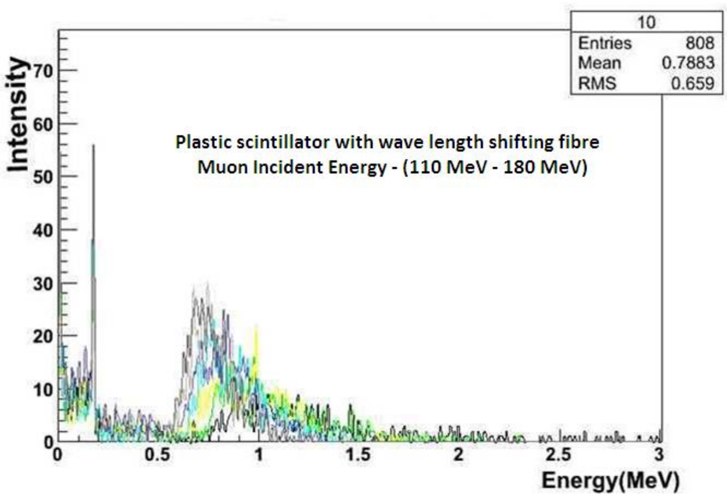

Figure 40: Plastic scintillation Detector Response for Muons from 110 MeV – 180 MeV.

Geant4 has different reflectors **(Agostinelli, 2006)** available i.e. Lumirror air, Lumirror glue, Teflon air, TiOair, Tyvek, vm2000air and vm2000 glue are implemented for polished, etched and ground surfaces with an interface of dielectric_metal and dielectric_dielectric to observe their effect on photon yield for incident muon.

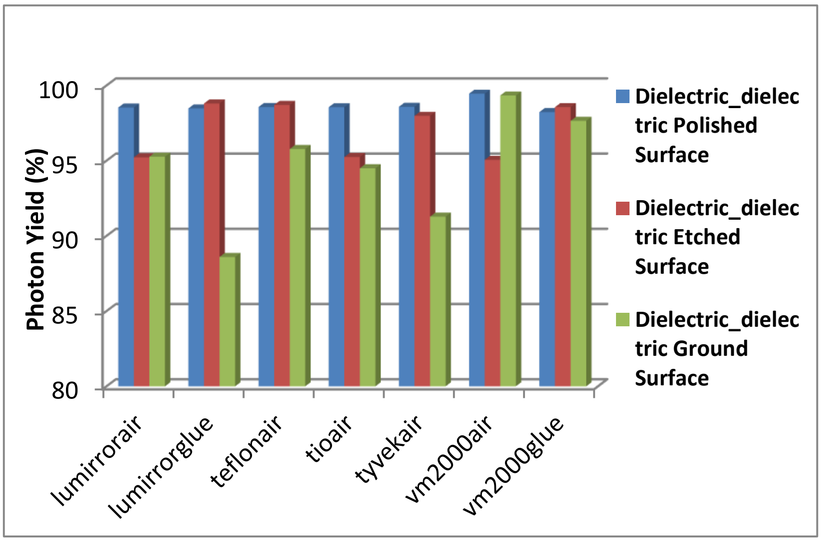

Figure 41: Photon yield for polished, etched, ground surface finish in Unified Model in dielectric_dielectric interface.

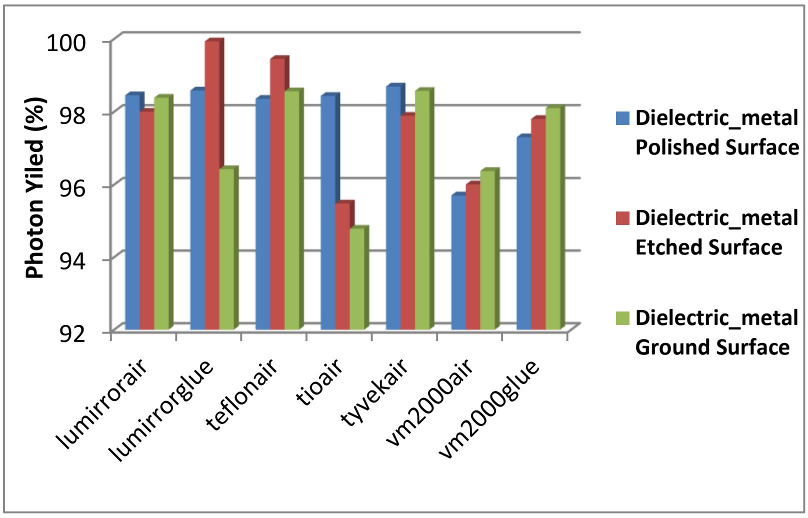

Figure 42: Photon yield for polished, etched, ground surface finish in Unified Model in dielectric_metal interface

The simulated photon yield is displayed for polished, etched and ground surface for dielectric_dielectric and dielectric_metal interfaces in figures 41-42. Each plot corresponds to the reflector materials that are simulated with their attachment combinations. The parameter represents the light collected from the medium which is further normalized. The optical boundary process design is based on the concept of *surfaces* where the physical properties of the surface need to be defined a *border surface* for the relevant physical and *skin surface* for logical volumes of the geometry. There are combinations of surface finish properties, such as *polished* or *ground* and etched are available for medium boundaries (dielectric_dielectric, dielectric_metal) to study its effect on the detector response. In these conditions, the photon undergoes total internal reflection, refraction or reflection, depending on the photon's wavelength, angle of incidence, and the refractive indices on both sides of the boundary but the reflection and transmission probabilities are sensitive to the state of linear polarization.

3.5 Study the energy spectrum of a radiation gamma source based on the concept of rotational matrix in Geant4

Whenever a high energy photon or charged particle incident on the scintillator, the energy of the particle gets converted to a visible energy. This visible light which is produced from a scintillator is proportional to the amount of energy deposited by the particle. These particles get completely absorbed as soon as the energy is deposited in the detector. A NaI scintillation detector is used for study of energy deposition and its relative intensity of Compton Scattered gamma ray. These are detected indirectly via interactions in the medium of detector. The photon interactions are fundamentally different from ionization processes of charged particles because the photon will be either completely absorbed (photoelectric effect, pair production) or scattered through a relatively large angle (Compton Effect). For low energies i.e. $\left(100\mathrm{keV} \geq \mathrm{E}_\gamma \geq \mathrm{Ionisation\ energy}\right)$ photoelectric effect dominates. At medium energy range ($\left(\mathrm{E}_\gamma \cong 1\mathrm{MeV}\right)$, the Compton Effect occurs whereas at higher energies, $\left(\mathrm{E}_\gamma \gg 1\mathrm{MeV}\right)$, the cross-section of pair production arises **(Garg, 2014)**. Illustration of these processes are shown in Figure 43.

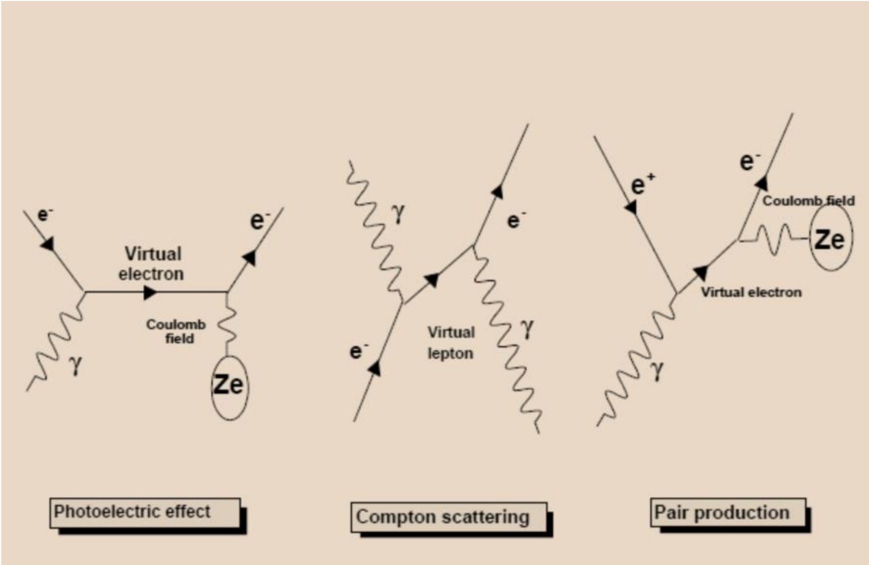

Figure 43: *Interaction of gamma-ray process: Photoelectric, Compton scattering and Pair production* ***(Griffiths, 2008)***

Photoelectric effect occurs when a photon scatters with an electron. These electrons are tightly bound to the nucleus, e.g, in K-shell. After scattering has occurred a virtual lepton is produced, which is then converted into a real electron through interaction with the nucleus by Coulomb field. The kinetic energy of ejected electron through the photoelectric effect is

$$T = E_{\gamma} - E \tag{27}$$

E is the ionization energy, i.e., the energy required to remove the electron from the shell. E_{γ} is the energy of the photon.

Compton Effect is dominant at regions at high energies or short wavelengths in contrast to Rayleigh process. It also has proved Einstein’s light quantum hypothesis. The process can be calculated in application to QCD **(Griffiths, 2008)** as shown in figure 44:

$$\gamma(k) + e(p) \rightarrow \gamma(k') + e(p') \tag{28}$$

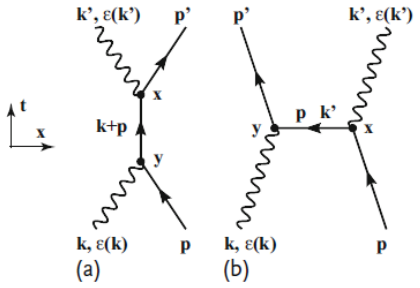

Figure 44: Contribution of Compton Scattering in QED phenomena ***(Griffiths, 2008)***

At these energies, and in general, nuclei are not needed since the binding of the electron can be ignored. A photon scatters with an electron resulting in a photon with different energy and direction. The energy of the photon scattered off an electron is

$$E' = \frac{E_\gamma}{1+(1-\cos\theta)\frac{E_\gamma}{mc^2}} \tag{29}$$

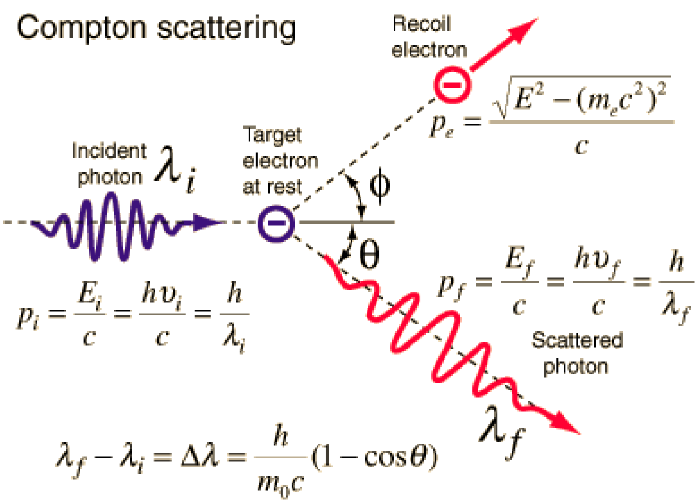

Figure 45: Angular distribution in Compton scattering [Source: hyperphysics.phy-astr.gsu.edu]

In Compton scattering, the incident gamma-ray photon is detected at an angle Θ from its original direction. This detection results in a decrease in energy (decrease in photon's frequency) of the photon and is called the Compton effect.

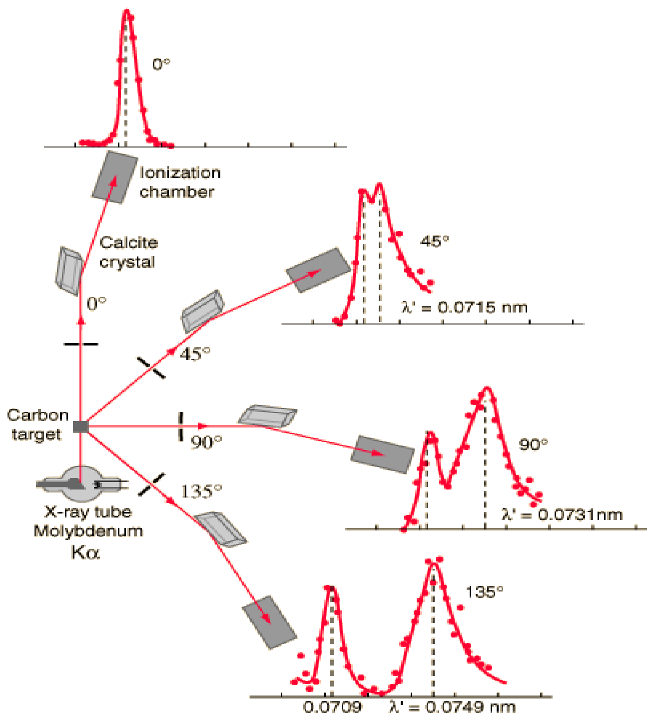

Figure 46: The change in wavelength of scattering depends only target particle. [Source: hyperphysics.phy-astr.gsu.edu/]

The Compton scattering in the scintillator or detector is due to the compton edge in the spectograph. This feature is due to photons that undergo Compton scattering at 180^0 scattering angle and then further escape from the detector. Only a fraction of initial energy of gamma source can be deposited in the sensitive layer of the detector when a gamma ray scatters off the detector and escapes from it. It depends on the scattering angle of the photon, how much energy will be deposited in the detector. This leads to a spectrum of energies. The Compton edge energy corresponds to full backscattered photon.

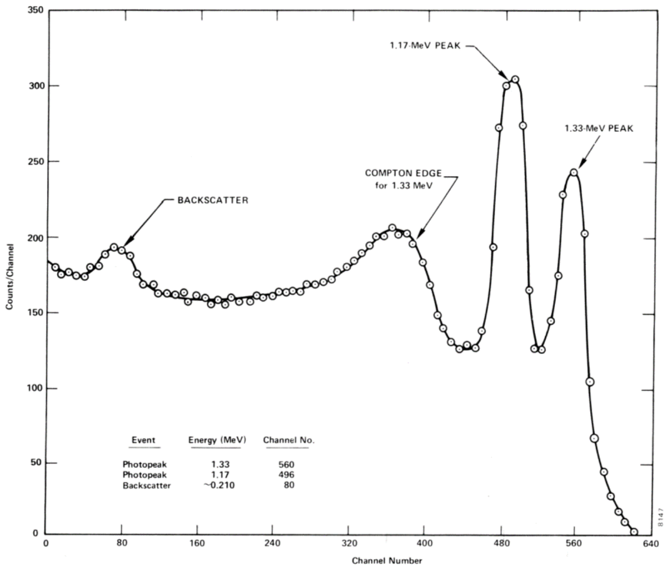

Figure 47: Compton edge of 60Co on gamma spectrometer Na(Tl) (Amaldi, 2014)

The energy of a photon scattering backwards $\theta = 180^0$ is

$$E' = \frac{E_\gamma}{1+2\frac{E_\gamma}{mc^2}} \tag{30}$$

This energy is carried by the photon. Therefore, the energy given to the electron must be

$$E_{edge} = E_\gamma - \frac{E_\gamma}{1+2\frac{E_\gamma}{mc^2}} = \frac{E_\gamma}{1+\frac{mc^2}{2E_\gamma}} \tag{31}$$

Which is called compton edge **(C.Grupen,2014)**

The photon is converted into a positron and an electron while undergoing pair production. Conservation of energy requires the minimum energy carried by photon to be $2m_ec^2 = 1.02$ MeV or a wavelength of 1.02 MeV or a wavelength of 0.012 A°. Since all of these interactions are present according to different ranges of energy carried by γ-ray, we expect the probability of having a certain range of energy to be more than that of another interaction. This also varies with different materials with which photons interact depending on the atomic number of the materials.

This simulation has been done in rdecay02 because it shows the energy deposition in detector. The detector has been constructed with a dimension $\mathbf{2'' \times 2'' \times 2}$" which is of NaI material. A scatterer has also been designed of cylindrical shape (0.1 cm in radius and 0.1 cm in length) and it is of lead material. It has been defined as

```
fTargetRadius = 0.1*cm;
fTargetLength  = 0.1*cm;
fDetectorThickness = 5.12*cm;
fDetectorLength = 5.12*cm;
fDetectorWidth = 5.12*cm;
```

Figure 48: Detector Construction class

The detector has been rotated with some angles. It has been done using rotational matrix

```
G4RotationMatrix* rm = new G4RotationMatrix();
rm->rotateX(-90*deg);
physiDetector = new G4PVPlacement(rm, G4ThreeVector(0.*cm,0.*cm,0.*cm),
logicDetector, "Detector", logicWorld, false, 0);
```

Figure 49: G4Rotation Matrix Class

With the help of rotational matrix, the position of detector can be calculated at different angles in 3-dimension. This can be calculated with

$$\begin{bmatrix} x' \\ y' \\ z' \end{bmatrix} = \begin{bmatrix} cos\theta & sin\theta & 0 \\ -sin\theta & cos\theta & 0 \\ 0 & 0 & 1 \end{bmatrix} \begin{bmatrix} x \\ y \\ z \end{bmatrix} \tag{32}$$

Table 8 shows the calculation of co-ordinates for detector at different angles when the detector was initially at (3, 3 and 3).

Table 8: Calcuation of position of detector for different angle in 3-dimension.

Angle	*New position (x', y', z')*	*Angle*	*New position (x', y', z')*
-90	(-3,3,3)	15	(3.66, 2.1,3)
-75	(-2.1,3.66,3)	30	(4.11,1.11,3)
-60	(-1.11,4.11,3)	45	(4.26,0,3)
-45	(0,4.21,1)	60	(4.11,-1.11,3)
-30	(1.11,4.11,3)	75	(3.69,-2.13,3)
-15	(2.13,3.66,3)	90	(3,-3,3)

The detector is making these angle θ with respect to scatterer. Figure below shows the setup.

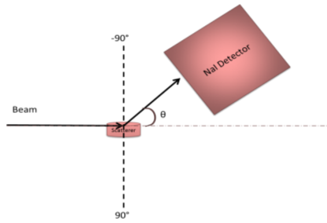

Figure 50: Setup designed for simulation of Compton scattering

It can be observed from figure 50 that when a beam fall on Lead (which can be called as scatterer because beam get scattered as falling on this), it gets scattered. When a photon/gamma ray particle hit the scatterer it get scattered by depositing some of its energy in that scatterer and some scattered photon will then fall on detector with an angle θ. deposited energy in the detector can be seen in a spectrum (Griffiths, 2008). This scattered energy of photon can be calculated by the formula given below:

$$E' = \frac{E}{1+\frac{E}{m_e c^2}(1-cos\theta)} \tag{33}$$

This equation shows the relation between transfer energy and scattering angle. Here $m_e c^2$ is rest mass energy of electron and this is equal to 0.511 MeV (Griffiths, 2008). E' is energy of scattered photon, E is energy of incident photon and θ is scattering angle.

Energy of recoil electron (E_e) can also be calculate with the formula

$$E_e = E + m_e c^2 - E' \tag{34}$$

$$\text{Or } T_e = E - E'$$

Here T_e is its Kinetic energy and can be given by $T_e = E_e - m_e c^2$. It can be seen from this equation that whenever photon will backscattered the electron will get maximum energy.

Pulse height spectra of four sources (Cs-137, Co-60, Ba-133, and Mn-54) have been recorded. The value of photo peak energy was not so closed from expected. In Table 8, the second column shows the expected value of energy of the sources and column shows the energy which has been got from the simulation. It shows that the energy resolution of plastic scintillator is very weak. By varying distance of the source from the detector, it can be conclude that on varying the distance of the source from the detector, there is no effect on peak energy but intensity of the peak decrease exponentially. Counts versus distance curve has been plotted here:

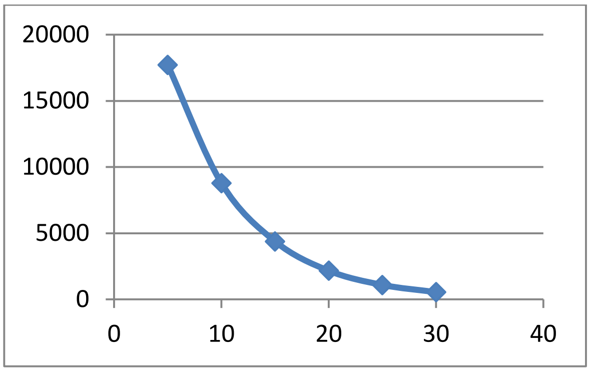

Figure 51: Distances versus intensity graph.

It can be observed from Figure 51 that on doubling the distance between source and detector, intensity goes down by a factor of four. On tripling the distance, intensity would decrease by the factor nine. On taking quadruple distance, the intensity would decrease by a factor 16 and so on. As a result, on moving the source at a distance ‘d’ away from the detector, then the intensity of radiation decreases by a factor $1/d^2$. The radioactive counts decays by a factor of $1/r^2$ with an inverse proportionality w.r.t distance of the source from the detector. The Compton scattering experiment has been performed with Co-60 (gamma source). The angle and position which have been calculated from rotational matrix has been changed. As the photon fall on the scatterer it deposits some of its energy in that scatterer and then it get scattered and then rest of energy deposited in detector. 10000 particles have been selected. Almost all particles hit the scatterer but some of them got scattered and reach to the detector. As can be seen from the data the maximum number of photon that reaches to the detector is 66-70 out of 1000 particles. From here it can be concluded that angle and position of detector also affect the intensity of the particles.

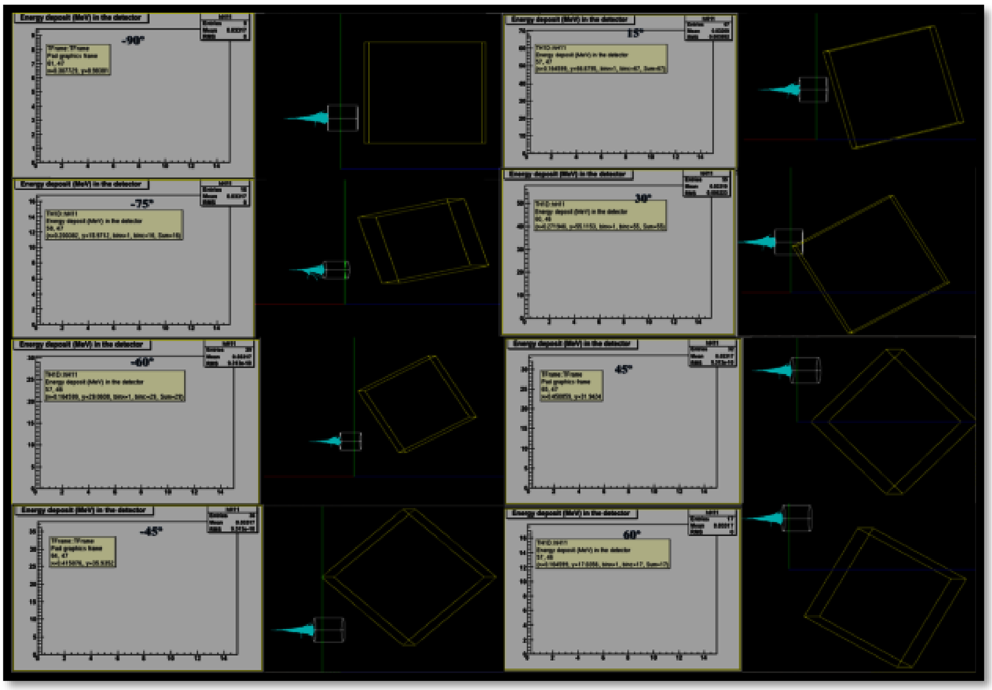

Figure 52: Energy deposition in scintillator at different angle visualization and result.

Table 9 shows the calculated scattered energy and scattered photon energy that have been got from simulation at different angles.

Table 9: Comparision between calculated and simulated scattered energy at different angles and its relative intensity.

Angle	*Expected scattered energy*	*Simulated scattered energy*	*Counts*	*Error*
-90	0.27	0.2	8.98	±0.26
-75	0.99	0.2	15.97	±0.80
-60	0.213	0.164	29.064	±0.23
-45	0.5607	0.41	35.93	±0.27
-30	0.3984	0.23	46.27	±0.42
-15	0.2326	0.164	70.14	±0.29
15	0.2326	0.164	66.87	±0.29
30	0.3984	0.27	55.1153	±0.32
45	0.5607	0.45	31.94	±0.20
60	0.213	0.164	17.035	±0.23
75	0.99	0.164	10.021	±0.83
90	0.27	0.23	9.94	±0.15

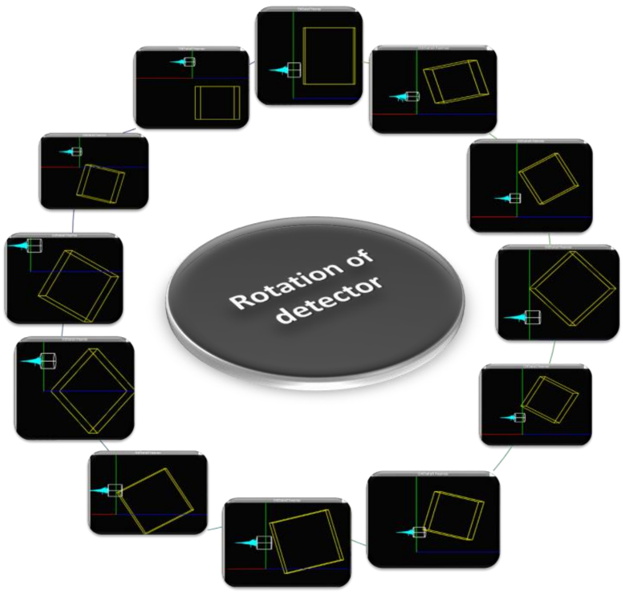

Figure 53: Visualization of gamma radiation at different angle versus intensity and energies.

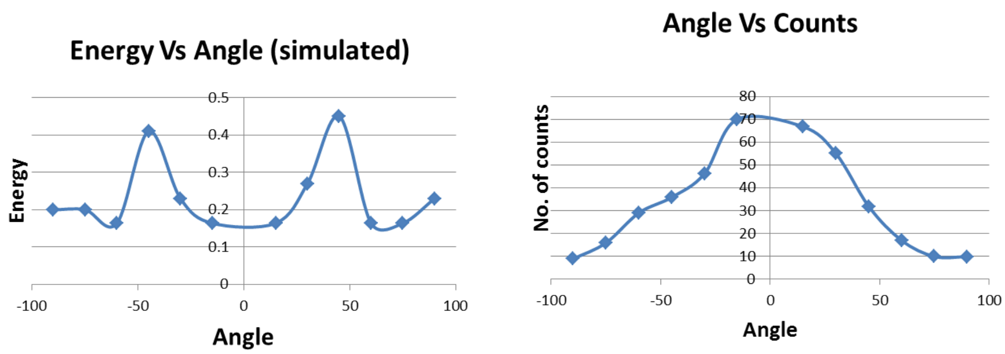

Figure 54: Graph for different angle versus intensity and energies.

The figure 53 and 54 shows the result that have been computed from simulation. From this result we can conclude that when detector is at 45º and -45º, energy of scattered photon is maximum. It has maximum intensity when detector has scattering angle between 15º and -15º, i.e. the number of photon that hit the scintillator will be large at this angle.

3.6 Summary:

The factors influencing the detector sensitivity such as cross-section and surrounding material of the sensitive region of muon telescope are studied. The muon interaction processes in different materials was studied in this paper using Geant4 simulation toolkit. The importance and procedure in calculation of total cross-section, interaction length and energy loss of muons was discussed. Dependance of muon cross-section mechanisms on relative energy transfer of muon to secondaries was studied. The significance of physics processes necessary for implementation of electromagnetic interactions in Geant4 using Standard EM Package is discussed. This is done in different bulk density materials like iron, polystyrene, hydrogen and carbon. The effect of multiple scattering on muon interaction length and total cross-section within these materials is studied. The interaction length of muon is observed to have an exponential decrease in nature w.r.t energy of incident muon. While total cross-section has a linear increase w.r.t incident energy of muon. After a certain cut-off region of muon energy, both the parameters remain constant. Muon has its total cross-section relative in behavior with iron where as its interaction length is maximum for carbon. For determining the accuracy in results, step cut of incident muon is varied to observe its effect on total cross-section and interaction length. Optical photon transport is used to predict the light distribution in scintillating materials. The surface characteristics of the muon telescope based on UNIFIED optical model characterized with different properties such as specular spike, specular lobe, backscatter, and Lambertian are implemented to observe the photon yield of the plastic scintillator for polished, etched, and rough-cut surfaces. The parameter is observed for various reflectors such as Teflon tape, ESR film, Lumirror, paint, and Tyvek paper.

Chapter 4
Applications of Hadronic interactions in Cancer therapy using particle detectors

(This chapter is based on the following published papers)

- S.N.L Sirisha, Sonali Bhatnagar ***"Bragg Peak Curves of proton beam in Water Phantom – A Geant4 based Simulation",*** presented at National Seminar on ***"Applications of Isotopes and Radiation Technology for Societal Benefits" (AIRTS– 2012,*** Abs. Vol. pp 45***)***.
- Vibhuti Yadav, S.N.L Sirisha, Sonali Bhatnagar ***"Stopping Power of Proton in different materials – A Geant4 based Simulation"*** at ***"DAE Symposium on Nuclear Physics***", Dec (03-07)2012 and published in symposium proceedings Vol. 57, pp: 734-735.
- S.N.L Sirisha, Sonali Bhatnagar ***"Stopping Power of Proton beam in water Phantom – A simulational study"*** published by Springer in the Lecture Notes in Electrical Engineering, Volume 188: titled ***"Recent Advancements in Systems Modelling Applications"***, page no. (79-88), ISBN: 978-81-322-1034-4.
- S.N.L Sirisha, Sonali Bhatnagar ***"Geant4: GATE and GAMOS – A systematic Implementation of HEP Simulation toolkit to oncology therapy",*** presented in ***"IEEE Student's technology Symposium – 2014"***, IIT Kharagpur, 28Feb-2March, 2014 organized by IEEE Student Branch, IIT Kharagpur and IEEE Kharagpur Section, Kharagpur and published in IEEE Xplore, ISBN No. 978-1-4799-2608-4/14©2014 pp 25-30.
- S.N.L Sirisha, Sonali Bhatnagar ***"Geant4 - Study of Dose Curve Parameters of Tumour in Human Tissues Using Passive Proton Beam"***, *published by* ***IEEE computer society*** with ISBN no. 978-1-4799-6929-6/14, DOI 10.1109/.50 pp: 178-185.
- S.N.L Sirisha, Sonali Bhatnagar ***"Determination of Equivalent Dose of Specific Organs in computational age dependent phantoms using proton therapy in Geant4",*** International Journal of Bio-Science and Bio-Technology Vol.7, No.5 (2015), pp.247-258.

4.1 Introduction

Radiotherapy is the most important technique which is implemented after surgery in a cancer treatment. Protons and light nuclei are mostly used for curing tumors. The heavy charged particles are advantageous than X-rays due to their improved biological efficiency and finite range of precise ballistics while preserving the healthy tissues with maximum dose deposition in the Bragg Peak region. Initially for treating the cancer tumors, different therapeutic approaches are developed for surgery, chemotherapy and X-ray therapy. But due to lack of control on tumor and also development of metastatic, these cancerous tissues are aimed to destroy by using ionizing particles while preserving the surrounding healthy tissues. The most crucial stage in this therapy is to accurately sight tumors which are deeply located in body while preserving simultaneous the surrounding tissues. This is not possible for X-ray therapy because of its ballistics. Thus the original ^{60}Co source is replaced by a compact linear accelerator to deliver high energy X-rays undergoing bremsstrahlung process that induces high energy electrons in the target. There are also different irradiation procedures such as Intensity Modulated Radio Therapy (IMRT), the cyber knife and tomotherapy which are developed to improve in efficiency.

Unlike photons, charged particle beams have a well-defined ballistics with a maximum dose deposition that may be defined as the end of its path with a sharp peak defined as a Bragg Peak. Its location is dependent on the particle incident energy. This feature can accurately sight the tumor with a weak dose deposition on the tissues located before Bragg Peak and with very weak dose deposition after Bragg Peak. Different energies are required for painting a tumor which results in a plateau spread from the combination of different energies. This plateau is termed as Spread Out in Bragg Peak (SOBP). This depends on the size of tumor and number of beams used to paint it.

The advantage of proton beam over the photon is due to their high and low energy interactions. At higher energy range, the energy transfer in protons undergoes via several processes such as direct inelastic collisions by proton, delta rays where elastic and non-elastic nuclear reactions may also occur. Here the ionization and excitation of atomic electrons are considered to be electronic interactions whereas Coulomb scattering, elastic collision and non-elastic nuclear collision undergoes nuclear reaction interactions. Secondaries are also significant in these interactions due to their considerable range of scattered energy. It even show a low dose rate with characteristic depth dose curve at the entry region whereas high dose at a precise depth. But while comparing to photons or neutron, it (proton) has a maximum energy deposition near the end of its range (the Bragg peak).

The primary protons mainly lose their energy due to Coulomb interactions at the entry region of the outer shell electrons which are emitted because of excitation or ionization processes (Fig. 3). Inelastic collision does not lead to any proton energy loss in this region. But there is no significant deflection of proton at this area due to its negligible energy loss. While considering the range of secondary electrons, it is less than 1 mm where most of the dose is absorbed within the neighboring regions. While the proton beam penetrates through the tissue medium, the incident energy gets lowered so that the events occurred due to presence of ionization rapidly increases and reaching to a maximum value known as a Bragg peak. The energy loss of the proton beam mainly depends on the charge and velocity of the projectile charged particles and the atomic number and electron density of the target material as per followed from the Bethe formula $-\frac{dE}{dx} = \frac{4\pi e^4 N Z_2}{m_e v^2} Z_1^2 L$

Where N is the target density, Z_2, m_e, v , Z_1, and L are stated as target atomic number, the electron the mass, the velocity, the charge and the stopping function. As the energy decreases, the velocity reaches to a 0 level which results in a peak (the Bragg peak) to occur. The Bragg peak width depends on range straggling in medium and its initial energy spectrum while the peak to plateau (P-P) ratio depends on the energy spectrum. However, at lower energy range (<10 MeV/A), the Bethe-Bloch model becomes invalid.

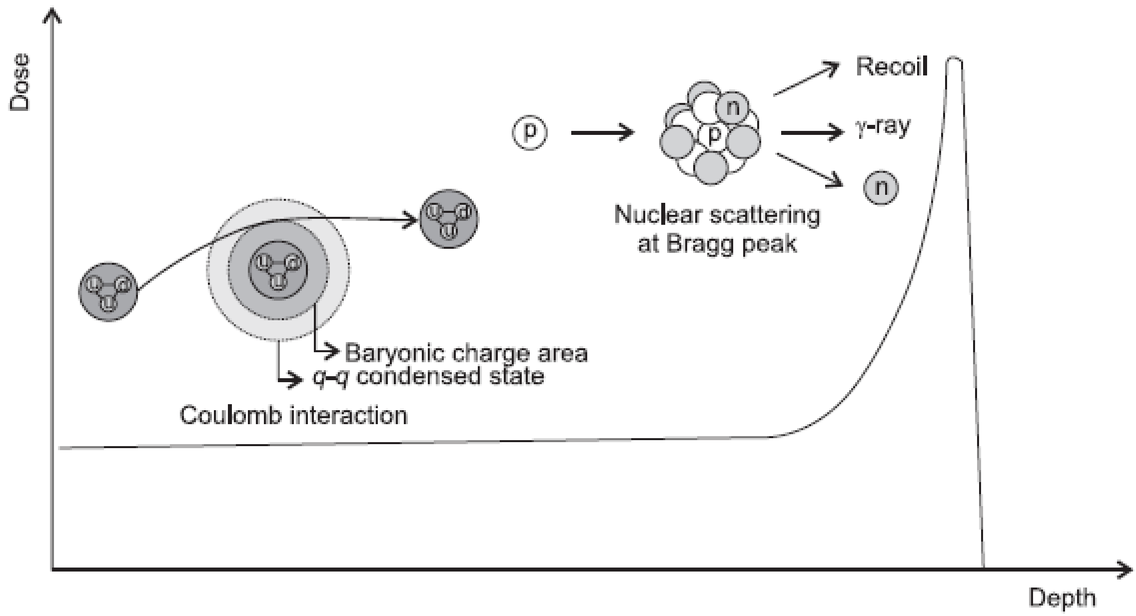

Figure 55: The Coulomb interaction reduces the velocity of protons initially at the entrance region of Bragg peak. But as proton energy lowers down, the stopping power increases at the Bragg peak where it emits secondary neutron and γ – rays upon its interaction with nuclei.

At higher energies, the protons undergo non-elastic interactions and produce secondaries which usually end up in the surrounding area of the interaction with a relatively high biological effectiveness. But the primary protons lose their energy impact during non-elastic nuclear interactions. But it contributes to the absorbed dose nearly 5% in 100 MeV, 10% in 150 MeV, and 20% in 250 MeV. For a proton of 250 MeV incident energy, there exists 20% probability to generate charged particles such as proton (*p*,*p*), deuteron (*p*,*d*), alpha particles (p,α) or recoil protons (*p,p'*) while undergoing a non-elastic nuclear interaction with the target nuclei. These secondaries further undergoes interaction to generate non-charged particle such as neutron (*p*,*n*) or γ -rays (p,γ) (i.e., 12C(p,γ)13N). They are relatively longer ranged constituents to get absorbed within the surrounding region of tumour. The resultant absorbed dose by the n-secondary particles due to neutrons ranges within 70–80% of the total absorbed dose, where it is observed behind the distal endpoint of the Bragg peak. Even though the low energy protons of (~ few 100keV) contribute only 5% of its dose, it is not that easy to understand the biological consequences of this interaction.

The proton gradually increases its interaction with orbital electrons as it slows down only to make maximum of its interactions at the end of its range. The energy finally reaches to its lower range of stopping power in order to exchange electrons with the target of hydrogen atoms which is also defined as a charge-changing process where we get two different processes i.e. electron capture p + $H_2O \rightarrow$ H + H_2O+ and electron loss H + $H_2O \rightarrow$ p+e- + H_2O processes. Despite of its contribution to dose, bio-cells confronts with biological damage which is induced by ions and radicals. These electrons which are almost the same scale of a chromosome in the cell nucleus, moves only a few micrometers. The spatial distribution of ions and radicals may even lead the low energy proton beams to form clusters and also can attack bio-molecules such as DNA. Thus, the significant factor of secondary production i.e. RBE increases in a depth (cm) which is beyond the endpoint of the Bragg peak. The ratio of the effective dose was found to be increased to 20:140:180 for each secondary particle which is increased by a factor of absorbed dose which is observed in the report by Matsuzaki et al. But the radiation weighting factors for electrons, protons, and alpha particles are 1, 2, and 20, respectively which are defined in the International Commission on Radiological Protection (ICRP) 2015. Thus this concludes that the dosimetry is difficult to evaluate an accurate method beyond the Bragg peak.

The biological effect induced by the charged particles also plays a crucial role in particle therapies. This biological response depends on radiation and tissue weighting factors of radiation protection. The radiation weighting factor / quality factor accounts for biological effect of different radiation qualities. For heavy ions, it is 20 whereas tissue weighting factor considers the radio-sensitivity of different organs. To determine the equivalent dose, both weighting factors are necessary to consider the radiation risk in the most conservative way. But in case of Relative Biological Efficiency (RBE), it compacts with the radiation quality and its specific response of a tissue along with radiation at biological end point and the dose level. RBE is the ratio of dose of the source radiation (e.g. X-rays or γ-rays) to the dose of charged particle to produce an identical biological effect (iso effect),

$$RBE_{iso} = \frac{D_{\gamma}}{D_{ion}} \tag{35}$$

It requires both the specification of reference radiation and the level of biological effect. The biological dose quantifies the dose of conventional radiation which yields same biological effect as the applied radiation. It can also be used for many biological end points such as DNA strand breaks, mutations or transformation. The treatment of hypoxic tumor also poses a significant challenge in this field. When tumor grows in its size, there is a need of new blood vessels to supply oxygen to the cells in the tumor core. They are of minor quality and also result in lower oxygen level as compared to healthy cells. In case of large tumors, this hypoxic condition is centered and also leads to a larger radio resistance. This effect is explained by oxygen enhancement ratio:

$$OER = \frac{D_{hypoxic}}{D_{aerobic}} \tag{36}$$

$D_{hypoxic}$ & $D_{aerobic}$ are doses with reduced & normal oxygen supply which results in same biological and clinical effect. It is quite different from RBE i.e. OER is a dose-modifying factor and is independent of dose. The RBE value increases with size of ion & ORE decreases with size of ion. OER=1, for ions heavier than neons i.e. the oxygen effect almost disappears.

For conventional therapy, the initial dose buildup by high energy photons is caused by forward scattered Compton electron which shifts the peak dose by a few centimeters away from the surface of patient’s body. In contrast to photons, the position of this peak can be precisely adjusted to a desired value in depth of incident ions. But protons and heavier ions also differ in two features essentially: Protons have a similar biological effect as photons (at the same absorbed dose) while heavy ions show high effectiveness, ranging from low RBE values in plateau region to a significant enhancement in Bragg Peak. Unlike proton, heavy ions exhibit a characteristic dose tail behind the Bragg peak, which is caused by secondary fragments produced in nuclear reactions along the stopping path of the ions, resulting in a complex radiation field. In the upcoming section 4.2, we will study the importance of Bragg curve and its corresponding parameters.

4.2 Bragg Curve - Parameters in Hadrontherapy

In radiotherapy, one needs to study about the dose deposition which is the most important physical quantity. Thus, absorbed dose (Gray Gy) can be expressed as the amount of mean energy deposited by ionizing radiation obtained in a medium,

$$D = \frac{d\epsilon}{dm}\ [1Gy = \frac{1J}{kg}] \quad (37)$$

The physical processes responsible for dose deposition are necessary to be understood for computing the stopping power for a particle. Inelastic is the significant process which results in collision of nuclei on the electrons of atoms present in target matter. Thus the projectile of kinetic energy E_c loses energy.

$$\delta E_c = e_c + I \quad (38)$$

where $e_c$energy of is out coming electron and I is Ionization potential of that electron.

The radiation quality refers to the features that influence the effectiveness of an irradiation. For constant physical factors such as dose, dose rate and fractionation, the effectiveness of an irradiation may vary, because of changes in the spatial dose distribution and energy transfers along and within the particle tracks. However, ionization is difficult or impossible to measure or even to define in solids and liquids. In 1952, Zirkle et al introduced the concept of Linear Energy Transfer (LET), which is also related to radiation quality and is easier to measure. The LET is often expressed in MeV/mm (or keV/μm). Linear energy transfer is the energy transferred by the material to material per unit length

$$LET = \left(\frac{dE}{dx}\right) - \sum E_c\ (e\delta) \quad (39)$$

Where $\sum E_c(e\delta)$ is total kinetic energy of δ electrons having energy above a given threshold. If some δ electrons are coming from an elementary volume depositing their energy in the volume consideration. This can balance the energy of δ electrons produced in that volume. Also in first approximation we can identify the stopping power, LET and absorbed energy in elementary volume of thickness dx,

$$dE/dx = LET = E_{dep}/dx. \tag{40}$$

Elastic Coulomb Scattering is another process which can slow down particle penetration in matter. It induces range end lateral spreading. The elastic collision with target nuclei is significant at low energies $E_c < 10\ keV/u$. But this process is neglected for hadron therapy applications. Electron capture leads to an effective charge of projectile. The term Z_p is replaced by $Z_{eff} = Z_p\,[\,1 - exp\,(-\,125\beta\, Z_p^{-2/3})]$. This is important at $E_c < 10MeV/u$. Bremstrahlung process is also neglected in hadron therapy application. The nucleus-nucleus collisions which produce secondary particles with longer ranges than the projectiles range. For protons, the inelastic collision on electrons is the most dominant one for all energies. For carbon ion this process is dominant except for last few µm in path.

The penetration depth of ions in matter is characterized by the range, defined as the depth for which half of the primary ions that did not undergo a non-elastic nuclear interaction stop. Range measurements are possible using a fluency meter such as a Faraday cup. As depth-dose profiles are routinely measured, it was necessary to link the range with a specific dose point. It has been shown that the range corresponds to the distal 80% dose point, as illustrated in Figure 54(a) for protons. This point is almost independent of the energy spread, which makes it very useful. When treating patients, physicians want to adjust the Bragg Peak range defined as the distal 90% dose point (clinical range), for safety. Therefore, one has to be careful when talking about “range”, as two different definitions are used.

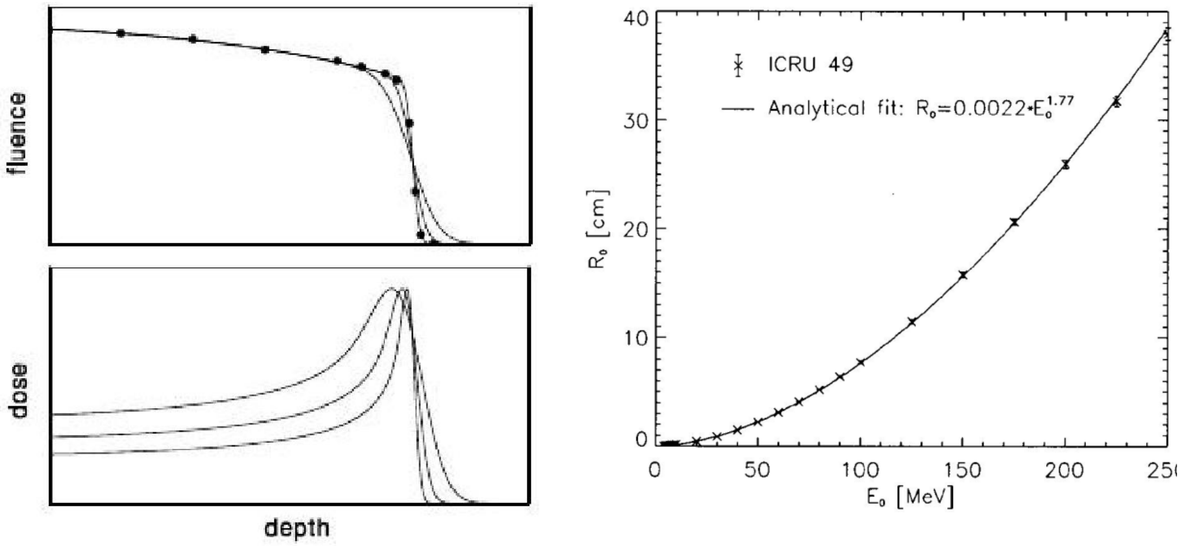

Figure 56: This figure shows a correlation factor within the parameters i.e. particle fluence and their dose. Here (a) Top: depth-fluence measurement for a proton beam of fixed mean energy, using 3 different energy standard deviations. (a) Bottom: depth-dose profile of proton beam. (b) Range energy relationship.

As physical interactions are stochastic, the number of collisions along the ion range varies, so that all ions do not stop at exactly the same depth. This effect is known as range straggling (or energy straggling). The most probable proton energy loss in individual collisions is of the order of 20 eV. Straggling depends almost only upon the inelastic coulomb interaction with atomic electrons. However, at low energies below about 1 MeV, elastic nuclear collisions and charge exchanges start to significantly contribute to the range straggling. The total energy loss Δ, in a track segment of length s, is a stochastic quantity, whose distribution is described in terms of Straggling function $f(\Delta, s)$. The straggling distribution is often modeled using a Gaussian, considered as a good approximation. For a given energy per nucleon, the range of a projectile is proportional to the ratio A/Z^2 where A is projectile number of charges. The corresponding energy range for protons is 0 to 220 MeV and from 0 to 425 MeV/υ for ^{12}C ions. The inelastic collisions leads to a straggling function which can be parameterized the following way

$$f(\Delta E) = \frac{1}{\sqrt{2\pi\sigma}} exp \frac{(\Delta E - \overline{\Delta E})}{2\sigma_E^2} \tag{41}$$

Here $\sigma_E = 4\pi Z_{eff} Z_t e^2 N \Delta x \left[\frac{1-\beta^2/2}{1-\beta^2}\right]$, Z_t is target number of charges, Z_{eff} is projectile effective charge, β is the projectile velocity in (units E projectile kinetic energy.) and x is unit path length.

Range straggling increases with the particle path length and has an impact on the Bragg peak width. Its standard deviation is material dependent and depends almost linearly on the range, as illustrated in Figure 55. In water, the range straggling is approximately equal to 1.2% of the mean range.

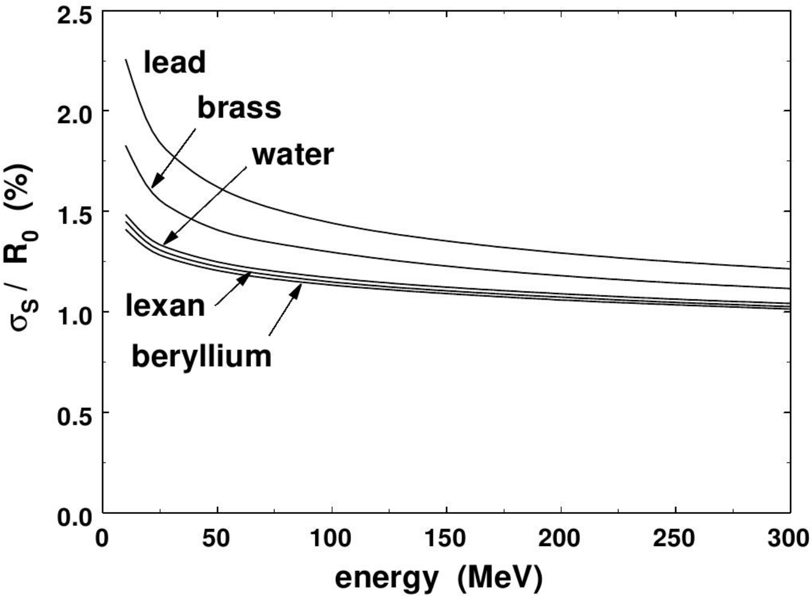

Figure 57: Range straggling of a passive proton beam in various materials

The nuclear stopping power deals with Coulomb scattering interactions with atom nuclei screened by atomic electrons. It has to be differentiated from nuclear (elastic and non-elastic) interactions. Usually, the nuclear stopping power is obtained by calculating the elastic Coulomb scattering cross-section and then the energy transfer to recoil nuclei. The elastic scattering cross-section is a function of the center-of-mass deflection angle θ and impact parameter p. Such interactions are described by a potential function, which takes into account the Coulomb potential for two bare nuclei (nucleus free of orbital electrons) and the screening potential from atomic electrons. Interactions within the electromagnetic field of nuclei screened by atomic electrons are responsible for most of the scattering undergone by incident particles.

Relativistically, the maximum energy that can be transferred from an incident ion to the recoiling atom, with appropriate ion and target nucleus masses replacing the electron and proton masses, respectively.

Proton scattering is mainly the result of deflections by atomic nuclei. The heavier ions like carbon ions are deflected much less than protons, which lead to a better penumbra for clinical practice. Multiple Coulomb Scattering (MCS) theories allow computing the mean scattering angle which results from many single scattering collisions. They are derived from elastic scattering cross-sections by means of numerical integrations. The most important role of multiple coulomb scattering theory was initially developed by Molière in 1948. The theory shows an accuracy rate which is better than 1% on average for protons. Other scattering theories were also developed as for instance by Hanson, Highland, Lynch or Rossi, as presented in the review from B. Gottschalk.

For practical purposes, as for instance patient dose calculation, it is of interest to be able to compute the mean scattering angle or transverse dose spreading of a proton beam at every depth in heterogeneous geometries. This approach is not directly available in multiple Coulomb scattering theories and step-size dependent approximations were developed. Similarly to the stopping power, the scattering power of ion and proton beams have been investigated recently in order to compute multiple Coulomb scattering angle variations at every depth without step-size dependence. Lateral spreading of beam is mainly due to Multiple Coulomb Scattering. This is smaller for heavy ions than for protons. For small deflections, the angular distribution of projectile after passing through a distance'd' of absorber can be described by Gaussian distribution.

In contrast with the nuclear stopping power, which results from interactions in the electromagnetic field of the target nuclei screened by atomic electrons, nuclear interactions are due to nucleus-nucleus collisions and deal with the strong interaction force. Nuclear reactions can be split into two main categories according to ICRU'63:

- Elastic: the incident projectile scatter off the target nucleus with the total kinetic energy conserved (the internal state of the target nucleus and projectile are unchanged).

- non-elastic: as opposed to elastic, the total kinetic energy is not conserved. The target nucleus may undergo break-up, excitation to a higher quantum state or particle transfer.

In the case of ions heavier than protons, the projectile may also be fragmented. A third category called inelastic has been defined as a special type of non-elastic reaction, in which the final nucleus is the same as the bombarded nucleus. The term nuclear interaction is important nuclear process.

The main effect of nuclear interactions is due to non-elastic collisions, which reduce the primary fluency of particles with depth. The probability that a stopping proton undergoes a non-elastic nuclear interaction increases with beam energy and about 25% of the incident protons undergo nuclear interaction at 230 MeV. Proton non-elastic nuclear interactions are responsible for nuclear build-up at the phantom entrance. But nuclear interactions are complex to understand and also suffer from higher uncertainties. Several models have been proposed to describe non-elastic nuclear interactions as for instance: the compound nucleus theory with pre-equilibrium de-excitation stage, the Intra-Nuclear Cascade (INC) with evaporation or Fermi-break-up equilibrium decay and the quantum mechanical multi-step approach. An important part of nuclear interaction models is the de-excitation stage, including secondary fragments and isotope production. In carbon ion therapy, these interactions are more important than for protons and account for up to 40% of the energy loss. The accuracy of the nuclear models is very important for therapy, because it impacts on particle and LET spectra distributions in the patient and therefore on the RBE.

The spatial dose distribution from clinical proton therapy beams is quite similar to those from photon and electron beams. At central high dose region, the lateral profiles are in flat manner after which they fall off in the penumbral region. But its width gradually increases with the tumor depth in the patient. But protons have a similarity in their central – axis depth dose curves from electrons and differ apart at sharper distal falloff. The proton beams can treat a wide variety of tumor sizes along with their sizes such as a relative low entrance dose, enormous and identical amount of dose to cover the tumor, and a quick falloff dose to spare normal tissues near the end of range which can have a uniform lateral dose profile and a sharp penumbral width. These types allows the beam to cure tumors while sparing the surrounding tissues. We can now examine their nomenclature and the physical processes that govern the shape of these regions. Figure 56 shows a pristine proton peak along with labels identifying several regions. In order of increasing depth, these are the regions of electronic buildup, protonic buildup, sub-peak, peak, and distal falloff. The figure also shows several characteristic depths (e.g. the depth at which the peak occurs) and various characteristic lengths (e.g. the 80%-to-20% distal-falloff length and the proximal-80%-to-distal-80% pristine-peak width).

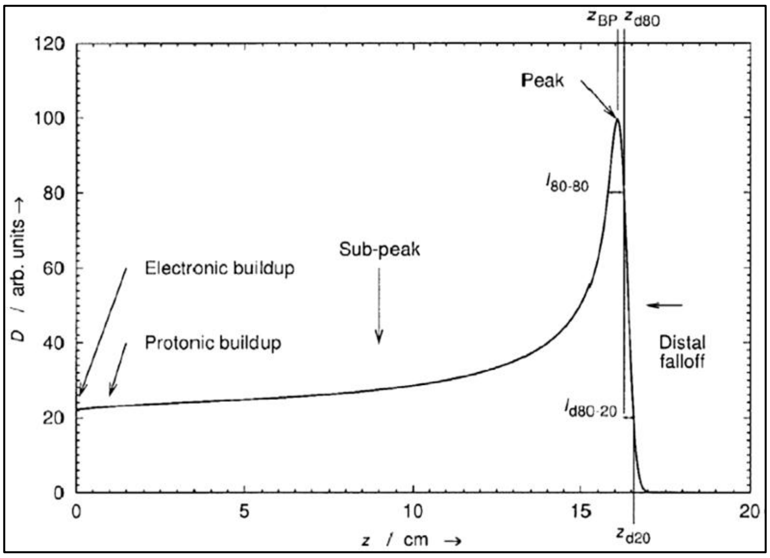

Figure 56: Absorbed dose D as a function of depth z in water from an unchanged (pristine) proton Bragg peak produced with an initial energy of 154 MeV.

The definitions of regions labeled in the figure 56 are discussed in this section below. Initially the electronic buildup of the Bragg peak is not visible in the plot but clinically it is useful to study the low dose rate relatively that are delivered to normal tissues in the sub-peak and distal-falloff regions. Their positions are relative to the target where the dose delivered.

When a depth-dose distribution in an absorber is irradiated with a monoenergetic proton beam, it helps in modulation of the proton fluence resulting in a region called '**Pristine Bragg curve'.** The proton beam after it incident on the surface of the absorber, it emits delta rays with a minimum amount of kinetic energy necessary to penetrate at least few mm into the tissue medium. But this region also exhibits an increase of dose relative to tumor depth which finally gives the absorbed dose which corresponds to the range of recoil electron that penetrates within the medium. But this **electronic build up** region is not seen in some cases which may be due to presence of any kind of device which can enhance a electronic charged particle equilibrium with a combination of proton buildup. The absorbed dose further increases due to secondaries which attributes towards non-elastic nuclear interactions. But this **protonic buildup region** cannot be observed at low incident proton beam energies. The physics processes involved beyond the region extending from surface of absorber to the depth have their dependency of stopping power on the inverse square of proton's velocity, influence of nuclear reactions on protons and its secondaries and the addition of lateral deflections due to multiple coulomb scattering which leads to disequilibrium in its fluence. This can be calculated from z_m- 2σ, where z_m is the depth at the pristine Bragg peak and σ is the width of the peak. The parameter σ can be computed from the spectral fluence of the incident proton beam and the range straggling which is stored in the absorber. The maximum dose deposited near the end of proton range is computed from the parameter i.e. **pristine Bragg peak** which is located at $z_{BP.}$ This is due to the proton stopping power and energy straggling where nuclear reactions have a lesser influence for very small fields. The maximum dose deposited by proton beam with a diameter which is > 6 mm is shown in figure 56 where it is located near the end of the proton range. But the dose deposited at the end of range is less for smaller beams where it reaches only till a center of the tumour region. But it restricts only till region of the $R \pm 4\sigma$, where σ is the distal falloff width, which prevents possible conditions, and makes *the Bragg peak* to be independent of the cross-sectional area of proton beam. This distal falloff region is greater than that of the pristine Bragg peak depth, z_{BP}. In many practical situations, however, the distal falloff region can be reduced to a depth where the dose falls below a threshold value, $D(z_{BP})$.

In a **distal-50%** depth i.e. (z_{d50}), the amount of dose absorbed would be equal to its own half at the pristine Bragg peak depth. In many cases, the dose varies with depth within the modulated peak region where the user can choose the absorbed dose value required for a modulated peak. The distal depth of the proton beam is almost equivalent to its CSDA range i.e., R_{CSDA} where the value of the mean proton energy correspond to its peak in the SOBP. The other distal depths can be similarly defined, as distal-90% depth z_{d90} and z_{d20}. Proximal-50% depth is the second distal depth, (z_{p50}), which is defined as the absorbed dose would be equal to half of the dose absorbed at the original Bragg peak depth, or $D(z_{BP})/2$. It occurs within the absorber. It is defined as the most proximal depth at which the absorbed dose is equal to half of the absorbed dose in the peak region in some cases for SOBP.

Treatment Planning System is designed to measure the parameters required to study using accelerator for development of 3D dose map. There are many features which includes within this design among which clinical images, organs identification through graphical approach for irradiation of beam in the injured or tumour effected area. A model is developed at Heidelberg Ion therapy (HIT), to observe the impact of biological effects from physical dose. Let us understand its concept in 1 dimension where the proton beam used to irradiate an l cm long slice in water medium. The corresponding depth dose profile $D_i(x)$ for an incident energy E_i can be represented in the form of factor of energy

$$D(x) = \Sigma_i N_i D_i(x) \tag{42}$$

Thus biological dose can be computed from $D(x) = \Sigma_i N_i D_i(x) BF(x)$, where $BF(x)$ is the biological factor. In order to determine N_i to deposit a wanted biological dose $D_{wanted}(x)$ at depth x. Thus,

$$\chi^2 = \int D_{wanted}(x) - \sum_i N_i(x) D_i(x) BF(x) \tag{43}$$

While considering the computation of biological dose, it results in

$$\chi^2 = \int \left(D_{wanted}(x) - \sum_i N_i(x) D_i(x) RBE_i(x) \right)^2$$

$$\frac{\partial \chi^2}{\partial N_i} = 0 \Rightarrow \int D(x) D_i(x) RBE_i(x)^{dx} dx$$

$$= \sum_j N_j \int D_j(x) RBE_j(x)\, D_i(x) RBE_i(x) dx \qquad (44)$$

Thus efficiency to treat relative biological issues are dependent on the energy transfer by proton to secondaries. It is similar to the concept of particle's stopping power dE/dx in a material. When the biological dose of proton beam is equal to physical dose, its linear energy transfer ranges in 0.5 MeV/mm to 3 MeV/mm with an efficiency of 1. But in case of carbon-ion beam it is from 20 MeV/mm. to 250 MeV/mm with a varied efficiency between 1.3 and 3. For an uniform distribution of particle beam to the tumour region, it is necessary to consider a treatment system which basically follows passive and beam modulated at fixed position or an active beam which can fully scan the tumour area.

In case of passive beams, the beam is adjusted to 3-dimensional form till the tumour region where a non-varied passive beam helps in shaping the element to collimate the beam. While active beams voxelised their target area and a pencil beam is used to kill the tumour cells. The beam is first delivered by broadening it with the help of a double scattering system which can efficiently causes a flat transversal contour region. The tumour can be further irradiated with a mono energetic beam which can be modulated further to cover the entire volume of the target region. Particle undergoes deflection further from its path in the field after passing through a collimator. The depth of the affected area and its pattern is adjusted by range compensator but with a fixed width and undergoing limitation of the system. The dose is consecutively distributed to the tumour region which is voxelised by use of an active beam scanning technique. It even helps in curing any kind of irregular tumour area without any implementation field or specific hardware. The beam loss while production of secondaries can be reduced with a stable beam position within the accelerator. This technique is been in use for curing tumors at the many proton and carbon-ion facilities.

The sensitivity of proton physical characteristics such as stopping power and depth-dose distribution of proton beams to observe the impact of adjacent material when present in the plateau and Bragg peak region were studied **(Suh, 2011)**. The dose profiles of deeply penetrating ion beams such as ^{3}He, ^{12}C, ^{20}Ne, ^{58}Ni were studied **(Burigo, 2013)**. The influence of production threshold on secondaries generated by carbon ion beam in a water medium was studied **(Zahra, 2011)**. The electromagnetic and hadronic processes which are necessary for energy transfer of proton beam in a water phantom is performed in the form of an application to oncological radiotherapy **(Depawn N, 2013)**. The impact of genetic effectiveness which helps in enhancing the physical dose profiles were computed and analysed **(Bourngaleb, 2011)**. **(Thompson, 2013) also** reported the dependence of Bragg peak on density of inhomogeneous medium. **(Fix, 2013) and (KGwosch, 2013)**, studied the effect of dose nuclear fragmentation reactions on the dose profile distributions by use of beams which are heavy and light nuclei.

In the upcoming sections i.e. in 4.3 a brief description of Geant4 and its application based on medicine oriented simulations i.e. GAMOS will be discussed. In section 4.4, the validation of Geant4 physics in hadrontherapy is presented. The effect of inhomogenities while beam irradiation in Bragg curve is observed for a passive proton beam in human phantom in section 4.5. An extension of the work discussed in section 4.5, i.e. to study the necessary dose equivalent in human phantom of different ages is presented in section 4.6. The chapter ends with a summary of the work in section 4.7

4.3 GEANT4 AND GAMOS

In radiotherapy, many treatment planning systems are developed for use of Monte-carlo technique in the field of radiotherapy. This leads to a successful opportunity for use of an interface which is a Monte Carlo in a viable systems of this area. Among these Geant4 is a toolkit developed for Monte carlo based applications in the field of high energy physics on implementation of object-oriented analysis and even extended with a diverse uphold of medical and astrophysics experiments. There are even wide variety of tools which helps for an accurate result where the user can provide a geometry and material definition; particles tracking and fields; physics processes, visualization (OPENGL, VRML, DAWN etc) interface and tools for analysis (ROOT, AIDA). Particularly in the field of medical physics, there are many functionalities which may provide extensions of electromagnetic processes even till low energies. There are also available hadronic physics models in this toolkit which are usable in treatment of Boron Neutron Capture Therapy or Hadron therapy.

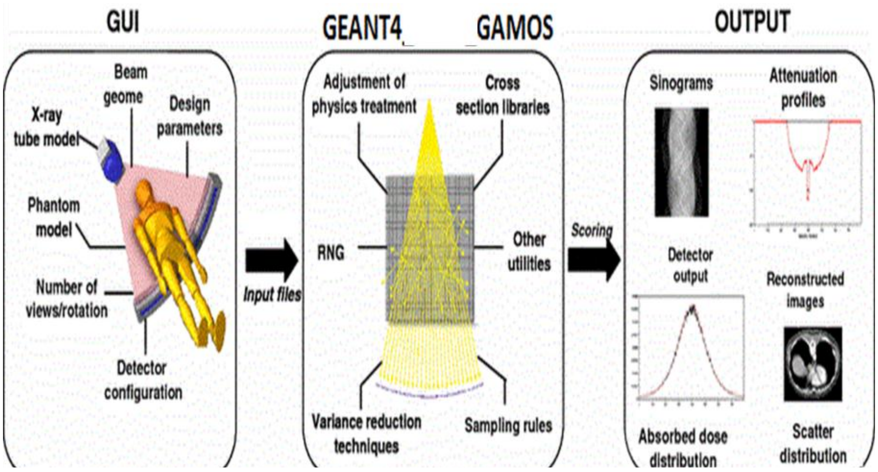

Figure 59: Step by Step methodology in simulation toolkits

There is an interface which is available for Geant4 simulation is GAMOS (Geant4 based Application for Medicine Oriented Simulations). There is no necessity to use C++ coding while compared to other codes which are based on Geant4 such as MULASSIS (MUlti-LAyered Shielding SImulation Software), GRAS (Geant4 Radiation Analysis Software), PTSIM (Particle Therapy Simulation) and TOPAS (Tool for Particle Simulation) ***(SNL Sirisha, 2014)***. It helps to overcome certain drawback which is in other codes such as irregular / complex shapes, primary generator source and its position distribution using physics processes. There is an advanced subsystem in each and every code i.e. random number generator which controls the probability distributions and its functions. It can also perform many realistic simulations such as dose deposition in tumours, imaging systems have been optimized.

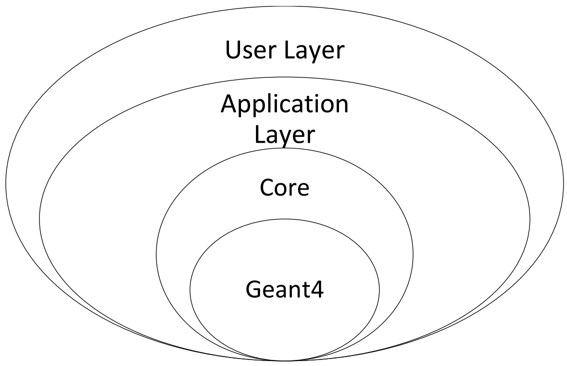

Figure 60: Core functionality in GAMOS toolkit.

The simulation can be performed even at nano-scale level for study of radiation in various scientific fields which involves medical, biology, genetics, physics, software engineering. There are also multiple categories which can be implemented with relative efficiency in Geant4 parameterisation, along with inclusion of biochemical processes. The other research areas include dosimetry, nanotechnology-based detectors, effect of radiation in space, high luminosity colliders, nuclear power, plasma physics etc. This interface not only provides functionality for new Geant4 physics but also introduces several methodological techniques that may help in simulation of radiation transport. There is feature in the available physics processes which may work at the nano-scale to even at micro-macro scale simulation.

The proton beam forms a Bragg curve at the end of its range where its location even depends on the biological effects induced by the charged particles. The proton beam undergoes multiple coulomb scattering and gradually slows down with an effective energy loss within the material. But its consistency may be influenced by inhomogenities that are available in surroundings within beam direction. They affect the Bragg curve and results in degradation of its peak position and range. This uncertainty has a greater impact on treatment system due to its maximum dose deposition of proton beam that delivers to healthy tissue. During beam irradiation, the particle range can be obtained from the measured distance between the entrance surface of beam and its 80% of distal point. The penumbra width is another characteristic that gives an absorbed dose in Bragg peak of distal region. Thus the effect of proton beam and its Bragg curve in a homogeneous medium is studied initially. The Geant4 toolkit, version

4.9.4.p04 was chosen to simulate a homogeneous medium that may depict the human phantom of dimension 100x100x100 cm^3 where the beam penetrates along x-direction which is in perpendicular to the human phantom as shown in Figure 61.

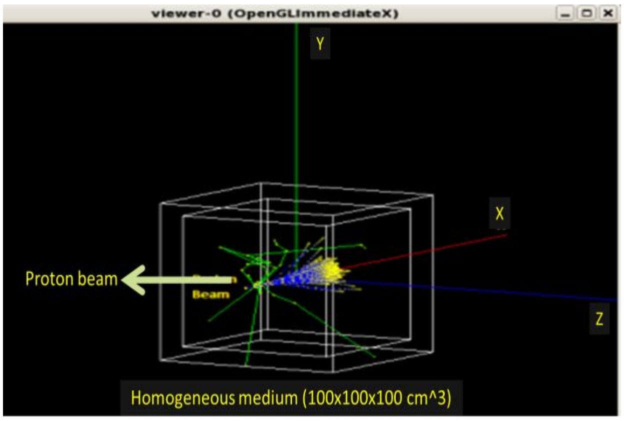

Figure 61: Homogeneous Medium used in study of Energy deposition of proton beam.

The electromagnetic and hadronic interactions are studied by implementing the physics models available in Geant4. They are given in Table 10.

Table 10: Models used	
Electromagnetic	standardem_opt3
Hadronic Elastic	G4HadronElastic (0-500GeV)
Hadronic Inelastic	Binary -Pre Compound(<100MeV)

The Bragg peak of proton beam within the energy range of 60-240 MeV was studied and is shown in Figure 62.

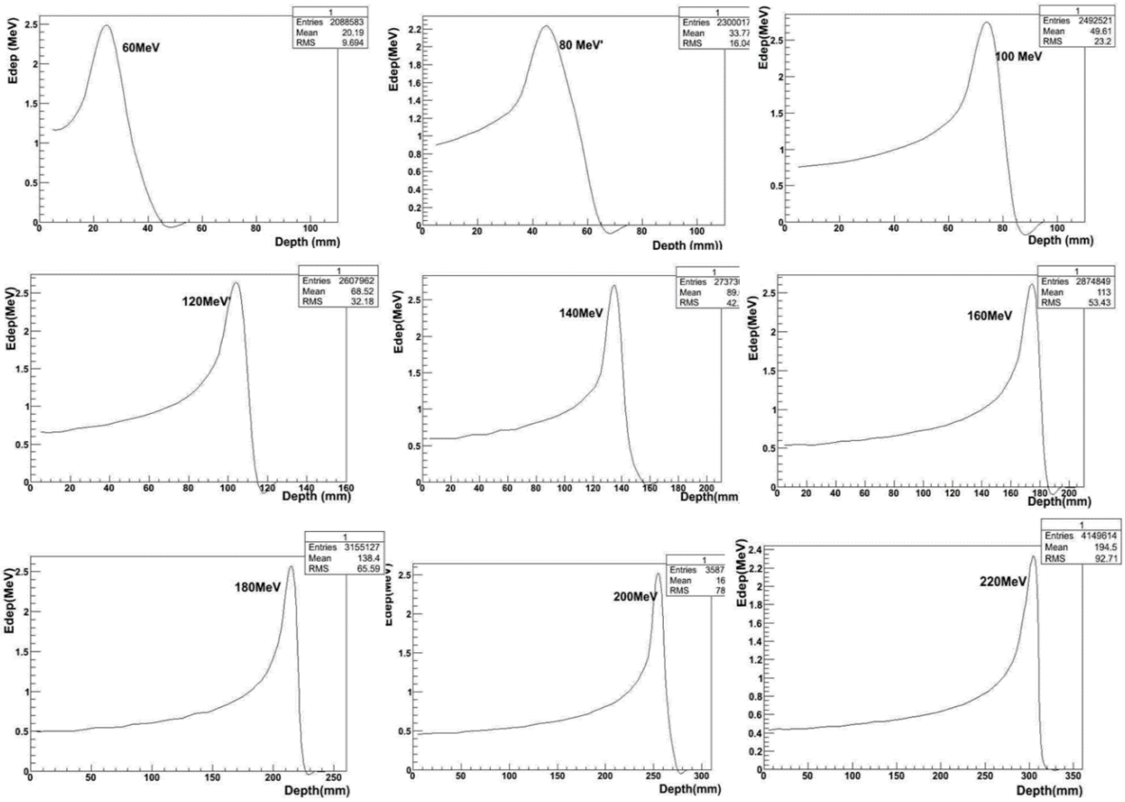

Figure 62: Energy Deposition of proton beam in a homogeneity medium.

The energy deposition with respect to depth in phantom is observed to increase gradually corresponding to its incident energy. The parameters obtained with respect to different proton energies are listed in Table 11.

Table 11: Bragg peak parameters of proton beam for energy range 60-240Mev.

Energy (MeV)	Bragg Peak Pos (mm)	Range (mm)	Penumbra (mm) (20%)	Penumbra Width
60	24.37	28.92	38.6	-9.68
80	44.43	51.34	61.02	-9.68
100	73.76	78.31	82.65	-4.34
120	103.86	108.39	112.16	-3.77
140	134.04	139.32	144.6	-5.28

160	174.09	178.54	182.31	-3.77
180	214.05	219.18	222.45	-3.27
200	254.1	259.11	266.15	-7.04
220	304.13	309.31	311.25	-1.94
240	352.27	358.89	364.08	-5.19

The energy deposition of proton beam while penetrates through a water phantom is compared with the available NIST data and ASO *et.al* for incident energies i.e. 150 MeV, 190 MeV and 230 MeV. The obtained proton range in water for different energies is given in Table 12.

Table 12: Proton range comparison within simulation and nist data, aso et.al.

Energy(MeV)	Depth (mm)		
	NIST	ASO *et.al* (GEANT4.6.0)	Present sim. (GEANT4.9.4.p04)
150	157.7	157.6	158.933
190	237.7	237.6	239.07
230	329.1	329.4	329.443

A human phantom is simulated using the builder design pattern. The 3D representation of the geometrical model and trajectories, etc; is generated using HepRepFile visualization driver and also shown in Figure 61. It generates files in the HepRep format, suitable for viewing with WIRED frame.

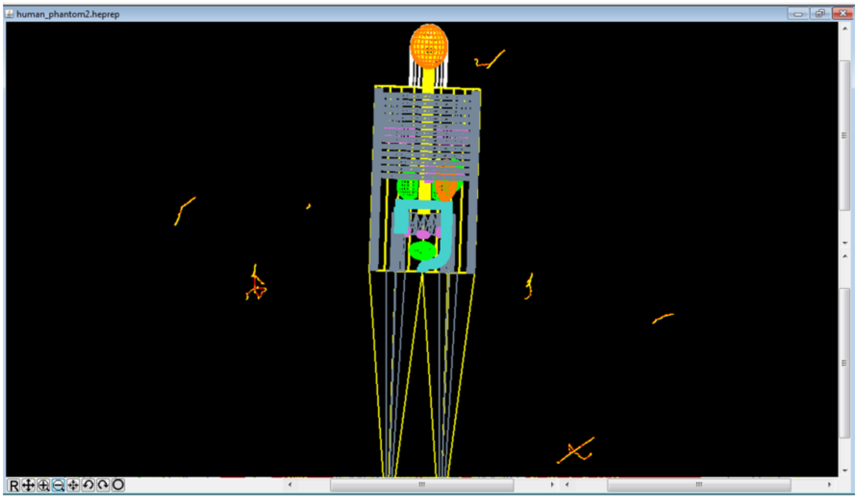

Figure 63: Human Phantom in Geant4

An electron beam of 50 MeV is incident on phantom and its energy deposition is calculated in the organs of the human phantom. In figure 64, it is shown another application i.e. Brachytherapy which is developed for an accurate evaluation of the anisotropy effects in the dose distribution. A thin volume is placed for obtaining gamma beam properties. The phantom is also used for computing the radial radiation dose distribution in the simulation.

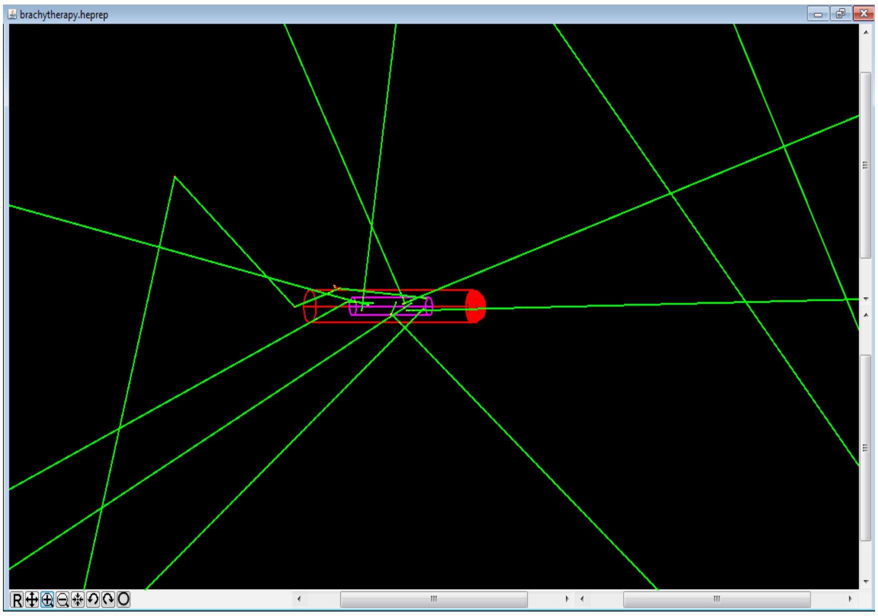

Figure 64: Brachytherapy simulation in Geant4

There are two phases in GAMOS for simulation i.e. PET & SPECT applications. In first phase, a simple ring detector is defined in the Geometry. The general setup is shown in Figure 65.

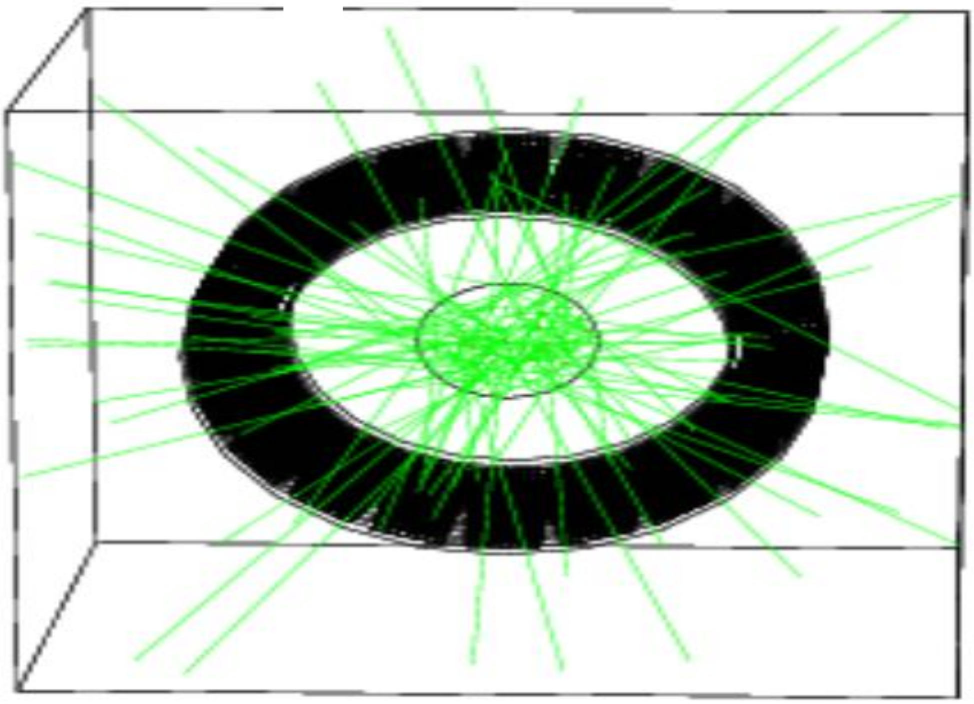

Figure 65: GAMOS simulation of a Simple Ring Detector

The parameters which are necessary to simulate the utility are number of crystals per block, no. of blocks of crystals per ring, number of rings of blocks, crystal size, trans-axial, crystal size, axial radial and diameter of detector ring. In second phase, there is an event classifier and histogram classes. The output includes the particle origin and its secondaries generated during annihilation process. The user can also compute the angle constructed between the secondaries and then hit the detector sensitivity. One can also define further physics parameters which helps in conversion of incident photons to photoelectrons undergoing photoelectric effect, Compton, Rayleigh process and energy lost by them at different positions also defined as a desired output.

The simulation of Compton camera includes rings of detectors or their stack which is defined as scattered detector where its scattering phenomena is the ideal mechanism that exists while the gamma rays incident on absorber detectors and undergoes photoelectric absorption. It is based on an algorithm i.e, Stochastic Origin Ensemble (SOE) developed for image reconstruction studies. The coincidence of a scatter and absorber detector tends to store in data files also can be performed using SOE.

The linear accelerator of electron or gamma rays is designed for transporting the initial beam of particles. This application can also be in use of dose computation in other techniques such as brachytherapy, X-ray CT, hadron therapy or dosimetry. The dose obtained from an accelerator can also be computed for several other voxelised phantoms. This framework also helps in the real phase movement of an accelerator where its phase space can be exiled or rotated in this framework.

4.4 Hadrontherapy and its validation in Geant4

This section gives an overview for the study of the validation of Geant4 based Hadrontherapy code which is developed by the group of Instituto Nazionale di Fisica Nucleare (INFN) at Italy. It is an ongoing experiment which is installed at laboratory of Nazionali del Sud (INFN-LNS), in Catania, which is the first Hadrontherapy facility i.e. CATANA (Centro di Adro Terapia ed Applicazioni Nucleari Avanzate).

The study includes simulation of a passive proton beam generated from a cyclotron. It is set for curing eye tumors. The functionalities of the corresponding elements present in the setup which are simulated are as follows:

1. A scattering system helps to spread the beam geometrically in the direction.
2. Set of collimators are used to avoid the scattering radiation during treatment.
3. The energy of the proton beam is modulated to a wide spectrum.
4. There is a special monitoring chamber which helps in transmission in order to control the particle flux during the beam irradiation.
5. A final collimator is defined for a tending shape of the beam before reaching the patient’s tumor.
6. Finally, a box of water phantom is placed to compute the energy deposited and dose is stored

The geometry setup used in the simulation for the study of proton beam characteristics in oncology therapy is shown below in figure 66:

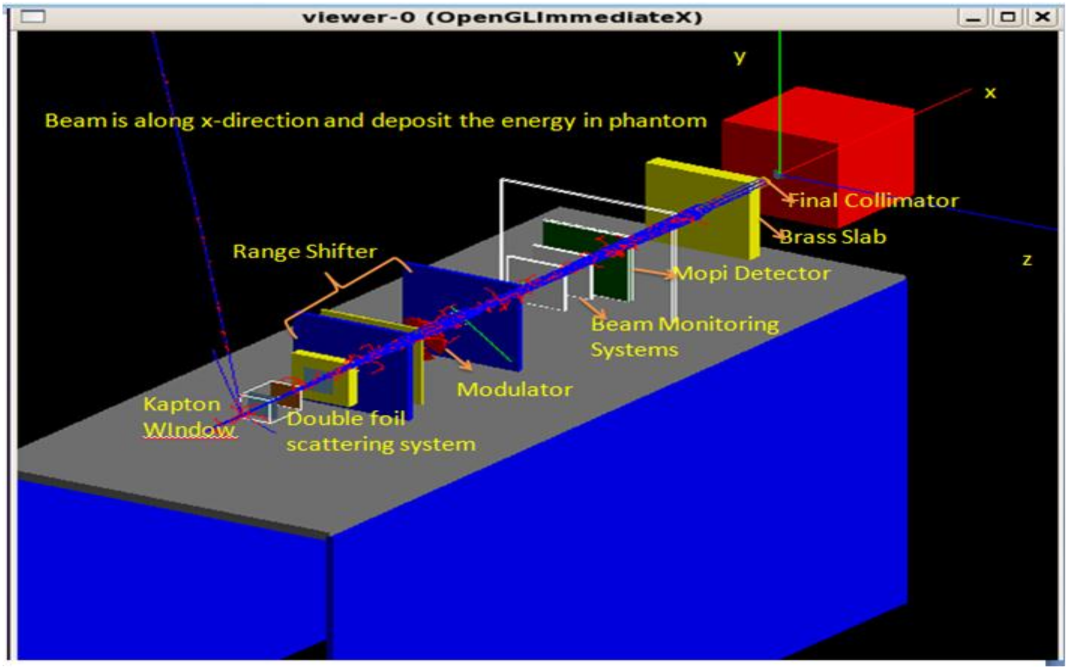

Figure 66: The visualization of the setup in Geant4 from the simulation of proton beam line during irradiation.

Before going to study the dose distribution in proton beam, it is necessary to check for the validation of code. A proton is allowed to accelerate through a cyclotron with incident energy of 62 MeV. The 3dimensional water phantom is voxelised into 200 slices with a thickness of 4cm in depth and is positioned in perpendicular to beam direction, where the total dose is stored. During this simulation, the user should also consider the transportation parameters of the beam. So the user should have to define the production threshold i.e., how many secondary electrons and gamma rays can be transported, which is set to 0.01 mm. this ensures that, the lower its value (production threshold), the larger would be the number of secondaries and also results in its total computational time. The simulated data of proton beam is also compared with experimental figures acquired at INFN-LNS, Catania. We found a satisfactory agreement among both the cases observed from figure 67 for the proton beams.

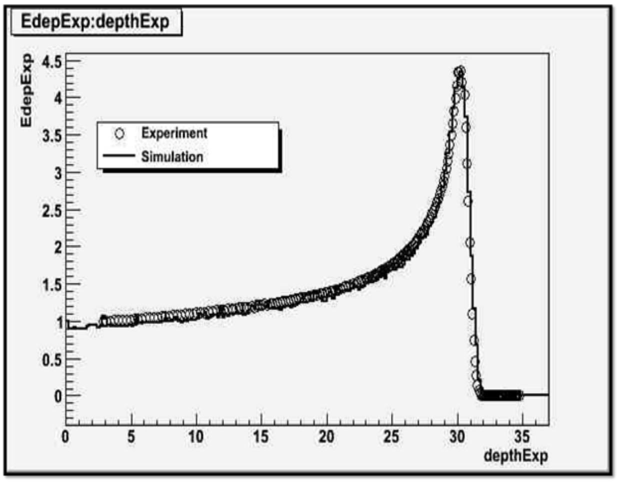

Figure 67: Simulated and Experimental depth dose profiles of a 62 MeV proton beam.

This can demonstrate its accuracy in formation of dose profile in Hadrontherapy based Geant4 simulation.

4.4.1 Proton beam stopping power in human phantom:

When we consider the case of fast charged particles such as protons which can ionize the atom or molecule while passing through matter, they gradually lose energy undergoing scattering phenomena. It results in maximum energy deposition in Bragg curve. This can be achieved only by obtaining the average energy loss of the particle per unit path length which can be denoted by $-dE\,/\,dx$ and is measured in MeV/cm. The stopping power of particle can be computed using Bethe-Bloch Formula:

$$-\frac{dE}{dx} = \frac{5.08\times10^{-31}\times Z^2\times N}{\beta^2}\left[F(\beta) - \ln(I)\right] MeV/cm \tag{45}$$

Where, $F(\beta) = \frac{\ln(1.02\times10^6\times\beta^2)}{(1-\beta^2)} - \beta^2,\ \ N = N_a\times\rho\times\frac{Z}{A}$

Here E is energy, ρ is density, I is mean excitation potential of target, β = v/c. The stopping power of proton in Brass, Al, Cu, Pb, Water, Plexiglas, Galactic materials is measured within the energy range from 0.01 to 10^5 MeV. It is performed using Geant4 toolkit. A dependency of stopping power on its incident particle energy is observed from Figures 68 and 69. Based on the theory of Thomas Fermi model of atom, Bohr proposed that the stopping power decreases as the particle velocity approaches the velocity of light for high energies above 100 keV region. When the particle's velocity is equal to the speed of light, its spherical field becomes distorted which results in higher energy loss at higher energies.

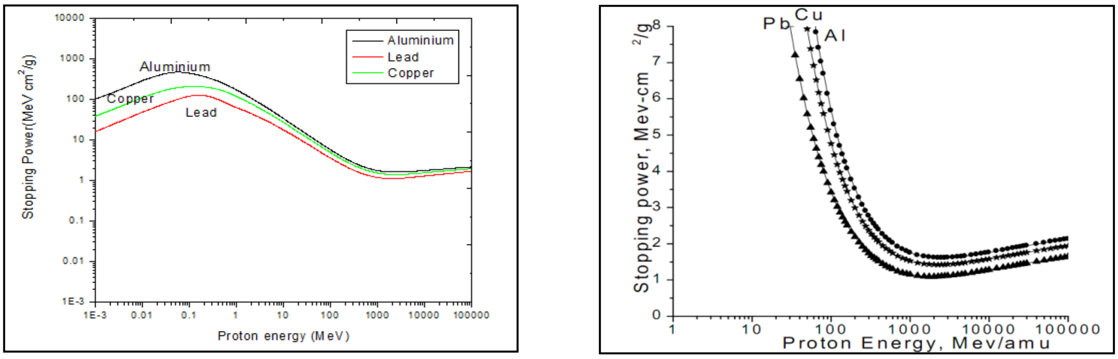

Figure 68 *Simulation result for stopping power of proton versus energy for Al, Cu, and Pb using Geant4. A satisfactory results for Al, Cu and Pb were taken from Literature Abebe Getachew, March 2007.*

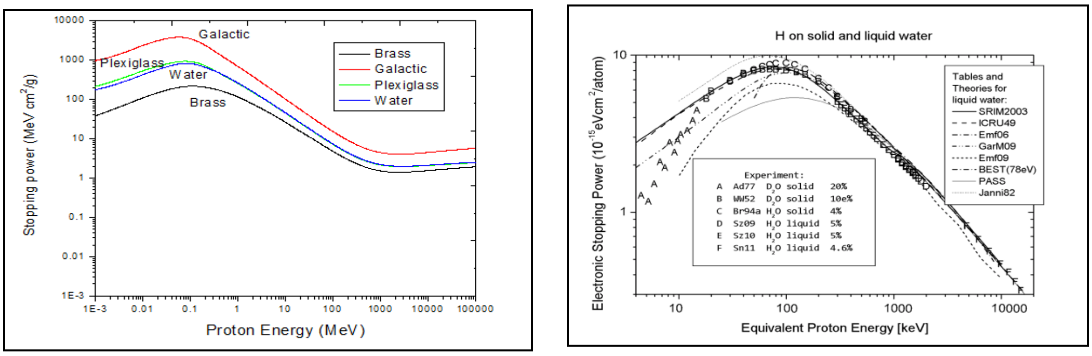

Figure 69 : Simulation result for stopping power of proton versus energy for Brass, Galactic, Plexiglass and Water using Geant4. It is compared from the literature by H.Paul – Nuc.Inst.Methods in Physics.res.d61(1991)26

The proton stopping power of proton is simulated in a water phantom and also compared with the analytical result within an energy range (0.001MeV to 100000MeV). It is compared between the result obtained from Geant4 and Matlab 7.0.1 which is shown in the figure 70.

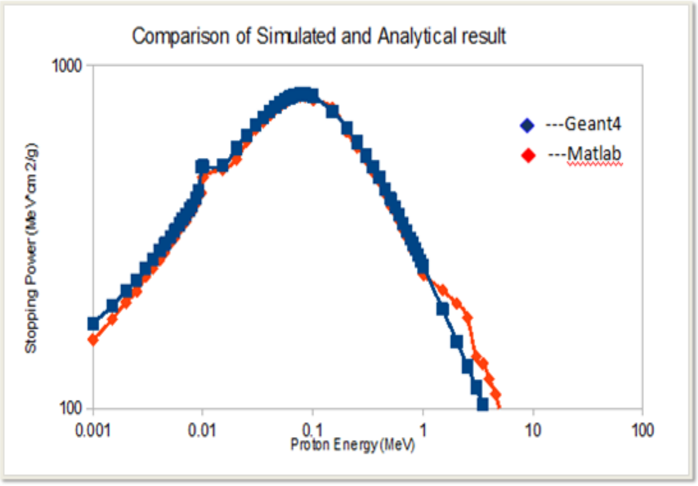

Figure 70: Comparison of the Stopping Power of proton in Water Phantom between the Geant4 simulation and Matlab result. It is also compared with ICRU Report 49, ICRU, Bethesda, MD, 1993.

Thus, stopping power has become an important parameter due to its various applications in the study of biological effects, radiation damage dosage rates and energy dissipation at various depths of an absorber. These studies are crucial in designing the detection systems, radiation technology etc.

4.4.2 Dose distribution profiles of proton beam at different energies:

The protons of energy ranges within 60-230 MeV is used for passive spreading of dose delivery in the patient's tumor region and its energy deposition in the water phantom is studied. The energy depositions of the proton beam in water phantom using Root 5.28.0 is illustrated in figure 71.

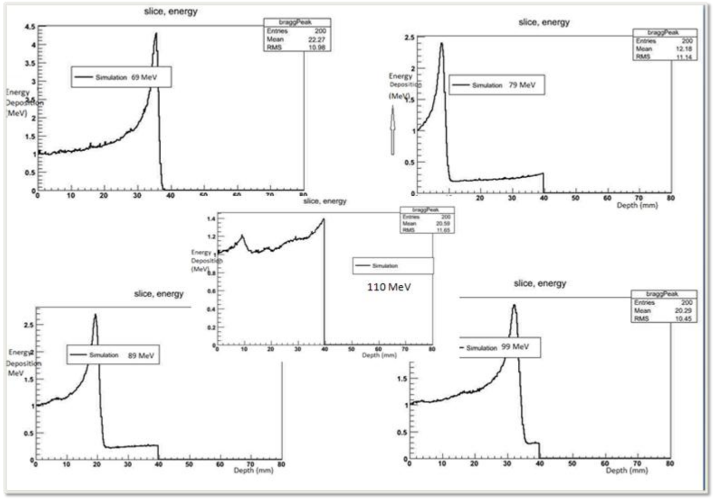

Figure 71: The proton dose deposition at different energies.

We observed a shift in the Bragg peak reaching lower depths from figure 71 at higher energies. It is not visible in clear at 110 MeV. We observed an effect of hadronic models for the peak distraction due to inelastic interactions at higher energies. The position of Bragg Peak obtained in the water phantom depth (mm) is illustrated in the figure 72. It is compared with the result obtained from report by G.A.P Cirrone et. al (2004). They also used a passive proton beam where the Bragg Peak position at 60 MeV is set to 32 mm depth of water phantom. In the present study the Bragg Peak position is at set to 29 mm depth. Secondly, an incident energy 98.71 MeV pencil proton beam is used from which a Bragg Peak position at 78 mm depth in water phantom is observed, whereas in the present work, a 31 mm depth of water phantom is obtained for 99 MeV proton energy. This variation obtained from the results even at same energies gives us a keen point to study the necessity for inclusion of hadronic models at higher energies.

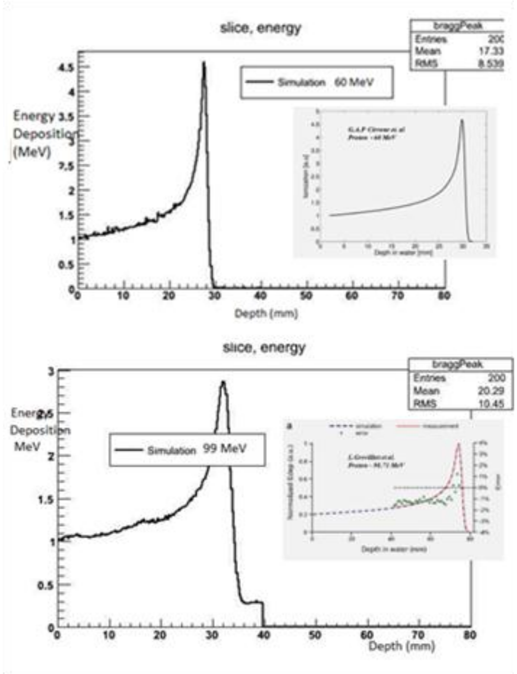

Figure 72: Comparison of the energy deposited in phantom corresponding to its depth with literature [G.A.P Cirrone et.al (2004), L.Grevilliot et.al (2010)].

To perform all these studies, the electromagnetic and hadronic interactions are activated following the second approach which are listed in table 13. An overview of the models used in this study are listed in table 13.

Table 13: Theoretical Models Used	
Electromagnetic Model	Emstandard_opt3
Hadronic Elastic Model	Elastic
Hadronic Inelastic Model	Binary

4.4.3 Significance of secondary distribution on dose profile:

The amount of dose which is a result of protons and its secondaries such as secondary protons, alpha, gamma, electron and deuteron are plotted on implementing the models using root as shown in figure 73.

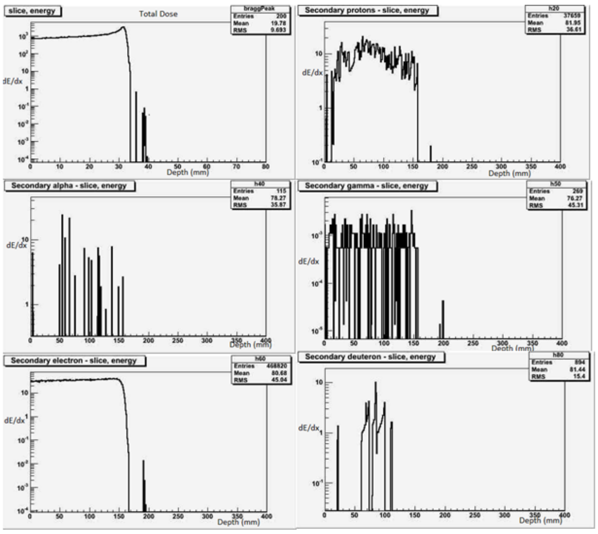

Figure 73: Particle dose that corresponds to the hadronic (binary) inelastic model.

The secondaries usually undergoes non-elastic interactions after generated from primary particle and also lead to a significant approach while delivering the required dose to their tumor region. Their yield also depends upon the beam delivery system. These parameters also helps to understand the impact of Radioactive Biological Efficiency (RBE) during energy transfer towards the tumor region. The dose of these secondaries also influences the peak-to-plateau region of an uncontrolled beam and the flatness of the Spread Out in Bragg Peak (SOBP).

4.5 Impact of Inhomogenities on Bragg curve and its parameters

A human phantom was simulated as a regular water medium with an aspect of 100x100x100 cm^3 geometry. The detector is located within a world volume of dimension 120x120x120 cm^3 which is of air medium. Inhomogeneous medium such as head, brain, thyroid and kidney of the human phantom are considered to insert in the tumor region for this study. They are simulated along with their positioning within the phantom. The material composition were taken from the NIST data base for an accurate result **(Sirisha, 2014)** and they are listed in Table 14.

Table 14: Compositions of Muscle, Skeletal and Soft Tissue			
Composition of MUSCLE,SKELETAL (ICRP) Density (g/cm^3) = 1.04 Mean Excitation Energy (eV) = 75.3		Composition of SOFT TISSUE (ICRP) Density (g/cm^3) = 1.000, Mean Excitation Energy (eV) = 72.3	
COMPOSITION			
Element	Fraction by weight	Element	Fraction by weight
H	0.102	H	0.102
C	0.143	C	0.143
N	0.034	N	0.034
O	0.71	O	0.708
Na	0.001	Na	0.002
P	0.002	P	0.003
S	0.003	S	0.003
Cl	0.001	Cl	0.002
K	0.004	K	0.003

The details of the beam used for irradiation in tumor and its physical characteristics are discussed here to implement in the present study. A Passive Proton beam is designed to study the effect of proton dose deposition while irradiates through the medium. The beam is in z-direction in which the phantom is placed. The study is carried out within valid experimental range of protons from 0 to 240 MeV. The beam follows Gaussian distribution of about 2.5 MeV in deviation along with its FWHM of 5.875 which is considered for the present study.

The proton range in a homogeneous water phantom is computed using Geant4.9.4.p04 and it is further compared with data available in NIST. The source of the proton beam was placed 10 cm away from the water phantom. Initial direction of proton source was also parallel to the beam axis along x-direction. The production threshold of the proton is set for 0.01 mm and the rest of all secondaries are subjected to get tracked if they have a longer range. The output obtained from homogeneous medium is also comparable with **T. Aso *et.al*** report (2010) which is listed in Table15.

Table 15: Proton Range Comparisons within simulation and NIST data, ASO et.al.			
Energy (MeV)	Water		
	NIST	ASO *et.al* (GEANT4.8.0)	Present sim. (GEANT4.9.3.p02)
210	187.7	187.6	188.9
230	217.7	217.6	219.0
250	229.1	229.4	229.4

4.5.1 Statistical Analysis of Bragg Curve

A Gauss fitting model is applied to the Bragg curve using ROOT data analysis of version 3.24. It is mathematically represented as: $p0*\exp(-0.5*((x-p1)/p2)^2))$. Where p0 = Constant, p1 = Mean, p2 = Sigma and the obtained values of these parameters ranges within: p0= (2.36e-00 to 3.55e+00), p1= (2.88e-01 to 2.97e+01), p2= (1.36e-01 to 1.54e+01). These values are fitted in ROOT 3.24 programming function.

4.5.2 Determine the Bragg curve and its paramters in presence of inhomogeneous medium during beam irradiation

The Bragg peak parameters computed in the present work also been compared with the report by **So-Hyun Park *et.al.* (2011),** where we have gone through several alterations to simulate our respective phantoms. The simulated phantom is represents an adult with inhomogenities that may resemble human organs such as kidney, human brain, thyroid. But their dimension and position differ from report of **S-H Park (2011)**. The dependence of Bragg peak region on density of inhomogeneous media is also mentioned by **Pflugfelder *et.al*** in his report. An innovative approach is designed by Sussanna Guatelli *et.al* for simulating a human phantom. It is performed to study the dose deposited in the organs for study of radiation exposure in the medium. T. Aso *et.al. also* estimated the dose that may influence the patient tumour by use of hadrontherapy in Geant4. The energies of 160 MeV, 190 MeV and 220 MeV for a proton beam is considered to determine the its peak in different materials such as water, lead and aluminium. It is also compared with NIST data base. The dose distributions for heavy and light nuclei beams were studied by Igor Pshenichov et.al, to observe the effect of nuclear fragmentation reactions on the dose profile. The physics models necessary for contribution to study electromagnetic and hadronic interactions for proton beam are analyzed by **Anthon Lechner *et.al***. The Bragg profile of proton beam at different energies in water phantom for radiotherapy applications was also studied.

The dose distribution of the proton beam in a human phantom for inhomogenities is measured and it is compared with the result for the homogeneous medium (water). Table 16-21 shows the calculated parameters of Bragg curve i.e. Bragg peak position, range, 20% - 80% position of penumbra and FWHM respectively for an inhomogeneous medium within the human phantom. The proton beam with a valid energy range which is to be used for study is also studied in each individual medium. The energy range suitable for proton beam corresponding to the dimension of a human brain is observed to be 65-123 MeV. The parameters associated with the Bragg curve of proton beam are also computed and shown in Table 16. There is a minor alteration in these values of the constraints when associated to homogeneous condition. This may be due to proton experiencing multiple coulomb scattering while relating with its material alignment i.e. soft tissue and muscular skeleton. There is also change in its Bragg curve when accumulation of a high density material i.e. muscular skeleton as shown in Figure 74. While considering for soft tissue, it is analogous as attained for water medium.

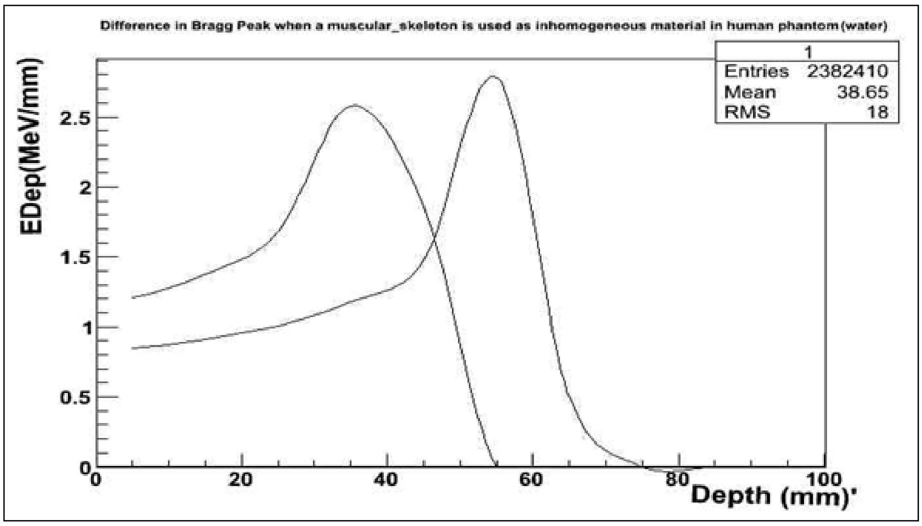

Figure 74: Change of Bragg Curve by inserting muscular skeleton when inserted in a homogeneous human (water) phantom

The variation within penumbra width of the Bragg curve for a human brain when compared with a homogeneous water phantom is shown in Figure 75.

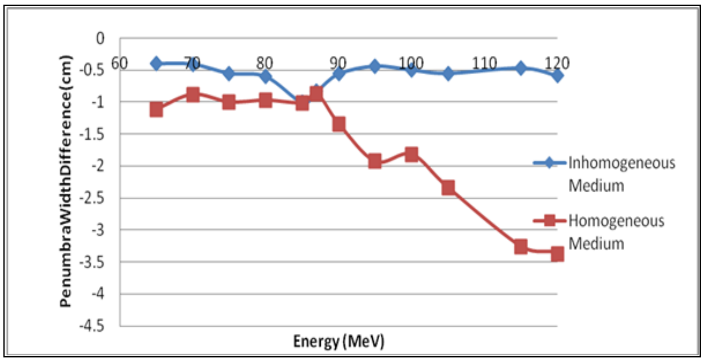

Figure 75: Penumbra Width Difference with respect to initial energy of proton beam case of Homogeneous medium in human brain

A variation of -0.8538% in significance of penumbra width for Bragg curve is observed for a proton energy range of 65 MeV – 120 MeV. The thickness of the inhomogeneity is also varied to study its effect on Bragg peak for an incident proton beam of 87 MeV where it deposits its maximum dose within the medium.

Table 16: The Bragg curve and its parameters calculated with respect to presence of human brain (soft tissue, muscular skeleton) medium in human (water) phantom. In the results given below INH: Inhomogeneous medium, H: Homogeneous condition, D: Difference among both the conditions.

Energy (MeV)	Bragg Peak (cm)			Range (Penumbra (80%)) (cm)			**Penumbra (20%) (cm)**			FWHM (cm)		
	INH	H	D	INH	H	D	INH	H	D	INH	H	D
65	2.2	3.2	1.0	2.4	3.5	1.1	2.8	4.6	1.8	1.2	1.3	0.1
75	2.5	3.8	1.3	3.3	4.6	1.3	3.9	5.6	1.7	1.3	1.4	0.1
85	3.4	5.3	1.9	3.7	5.2	1.5	4.7	6.2	1.5	1.4	1.5	0.1
95	4.4	7.3	2.9	4.9	6.0	1.1	5.4	7.9	2.5	1.4	1.6	0.1
105	5.4	8.5	3.1	5.7	6.6	0.9	6.3	9.0	2.7	1.5	1.6	0.1
115	6.2	9.4	3.2	6.7	6.8	0.1	7.2	10.1	2.9	1.5	1.6	0.1
123	7.0	11.0	4.0	6.9	8.0	1.1	7.6	11.9	4.3	1.6	1.7	0.1

Table 17: The Bragg curve parameters calculated with respect to presence of human brain (soft tissue, muscular skeleton) medium in human (water) phantom.

Thickness (cm)	Bragg Peak (cm)			Range (Penumbra (80%)) (cm)			Penumbra (20%) (cm)			FWHM (cm)		
	INH	H	D	INH	H	D	INH	H	D	INH	H	D
0.2	2.2	3.3	1.1	2.8	3.7	0.9	4.7	4.2	-0.5	1.4	1.5	0.1
0.4	2.2	3.3	1.1	2.8	3.7	0.9	4.7	4.2	-0.5	1.4	1.5	0.1
0.6	2.2	3.3	1.1	2.8	3.7	0.9	4.7	4.2	-0.5	1.5	1.5	0.0
0.8	2.2	3.3	1.1	2.8	3.7	0.9	4.7	4.2	-0.5	1.4	1.4	0.1
1	2.2	3.3	1.1	2.8	3.7	0.9	4.7	4.2	-0.5	1.4	1.4	0.1

Table 17 gives a detail discussion of the parameters obtained from Bragg peak which has their shift on varying the thickness of the medium. The Bragg curve and its parameters have less impact on the thickness variation of the inhomogeneous medium. A 2D scaling method has developed by **(Hanitra Szymanowski *et.al, 2013)*** for an accurate dose distribution with four different materials i.e. water; bone, fat and muscle are considered in a homogeneous media. This study even comprised with two different cases, where the former one is a simple combination of a water phantom along with a bone or an air slab placed and their thickness and position also varied. In this case the slab thicknesses considered are 3.0 cm and 1.0 cm. While in the other case, water phantom contains a 2 cm thick air slab between two 1.0 cm bone slabs. A deviation of 6% is observed in the dose distribution of 160 MeV proton beam when a 3.0 cm bone slab is placed. In case of 3.0 cm air slab when placed in the homogeneous medium, an 8% of underestimation from Monte-carlo result.

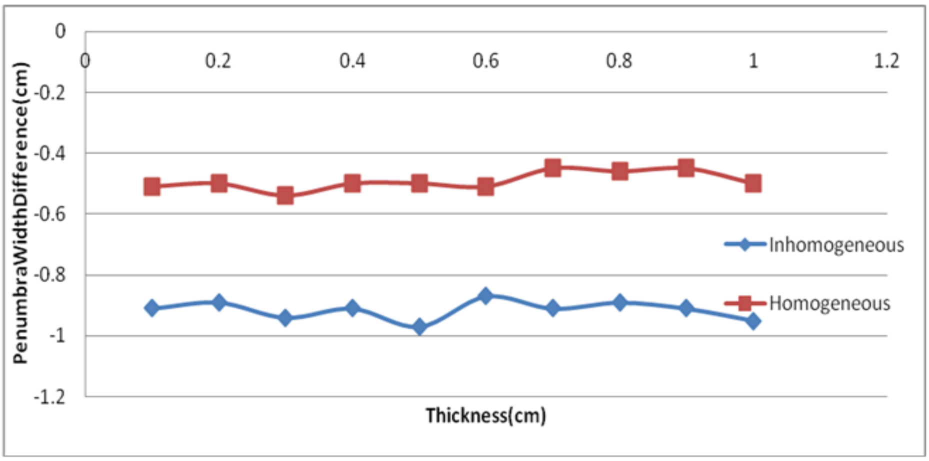

Figure 76: Penumbra Width Difference with respect to thickness of Homogeneous and Inhomogeneous medium in human brain

There is an -0.36% inaccuracy in penumbra width of Bragg curve is observed corresponding to homogeneous condition on varying the thickness from 0.1 – 1.0 cm for a inhomogeneous medium i.e. kidney is shown in Figure 76. The energy range of proton beam is observed to be 65 – 109.2 MeV which is suitable for irradiation in kidney. The obtained parameters from proton dose distribution when incident on inhomogeneity i.e. kidney are calculated and listed in Table 18.

A decrement in position of the Bragg peak is observed for a inhomogeneous medium when compared to the homogeneous medium. Similarly it is followed for range and penumbra width parameters.

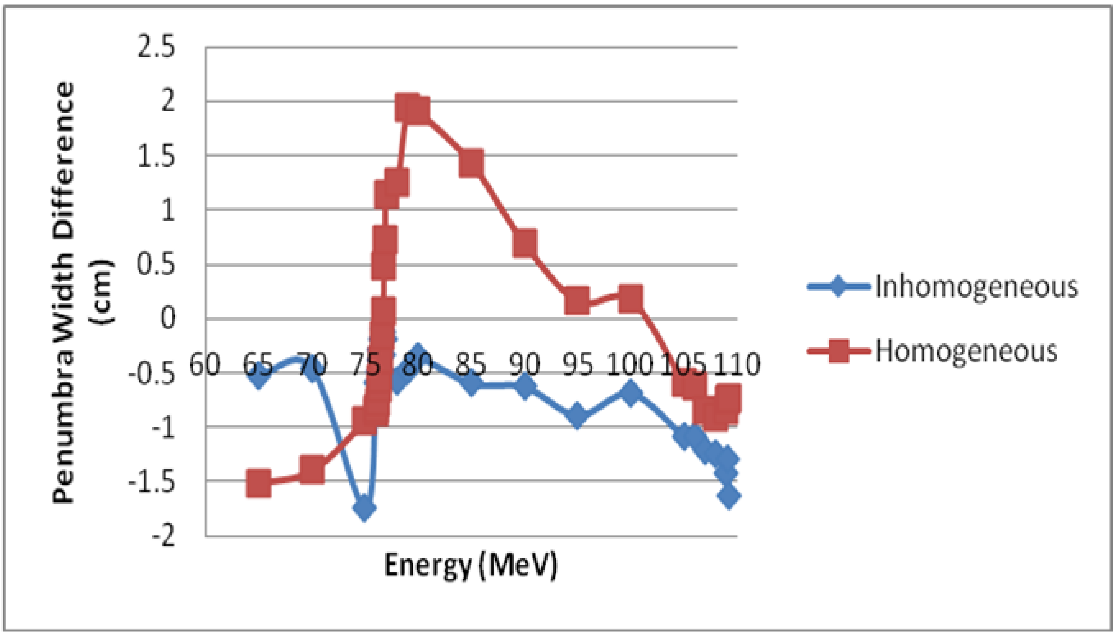

Figure 77: Penumbra Width Difference with respect to initial energy of proton beam in case of Homogeneous and Inhomogeneous medium in kidney

The proton energy of 76.3 MeV is set to incident on the inhomogeneous medium. The dependency of Bragg curve parameters associated with the thickness variation of inhomogeneous medium are listed in Table 19. It is observed that Bragg curve and its parameters are less dependent on the inhomogeneous medium. The change in penumbra width of the Bragg curve with and without presence of the kidney medium in human phantom is shown in Figure 77. A shift in 0.49 % is observed with an overlap in value of penumbra width of Bragg curve is observed for an proton initial energy range of 65 MeV – 109.2 MeV.

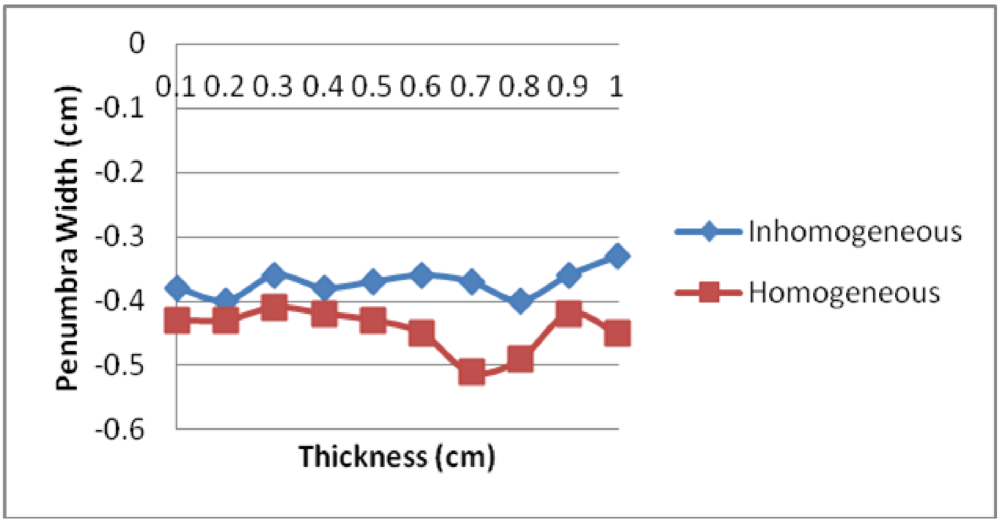

Figure 78: Penumbra Width Difference with respect to thickness of homogeneous and Inhomogeneous medium in kidney.

A deviation of 0.04% for penumbra width of Bragg curve is observed on varying the thickness of the inhomogeneous medium from 0.1-1.0 cm and is shown in Figure 78. It is also observed that the suitable energy range of proton beam in case of human brain is 65-100 MeV.

Table 20 also details the parameters computed from proton Bragg peak in human brain. A decrement in position of the peak is noted in case of inhomogeneous medium. It is similar in order in case of range and penumbra width. The figure 79 given below compares the variation in penumbra width of the Bragg curve with and without presence of the thyroid (soft tissue) medium in human phantom.

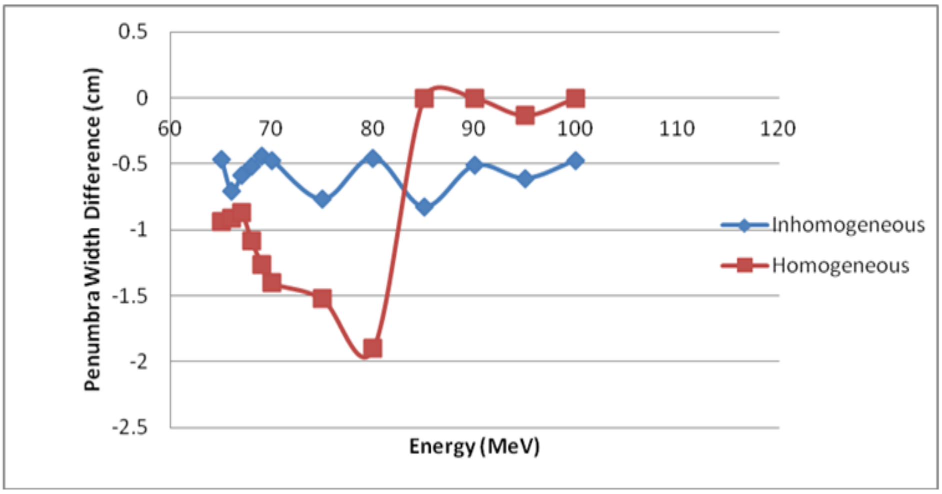

Figure 79: Penumbra Width difference with respect to initial energy of proton beam in case of homogeneous and inhomogeneous medium in thyroid

For a proton beam within an energy range from 65 MeV – 100 MeV, it is observed that there is a deviation of 0.44% in the penumbra width. The proton energy at which it deposits maximum dose deposition within the center of medium is considered in case of thyroid, for incident energy of 65 MeV of proton beam.

The dependency of Bragg peak parameters on thickness of inhomogeneous medium are given in Table 21. The Bragg peak position ranges from 1.05 cm to 0.89 cm for inhomogeneous medium. Thus, they are less influenced w.r.t thickness of the material. A gradual decrease has been observed in FWHM parameter with respect to thickness of both homogenous and inhomogeneous conditions.

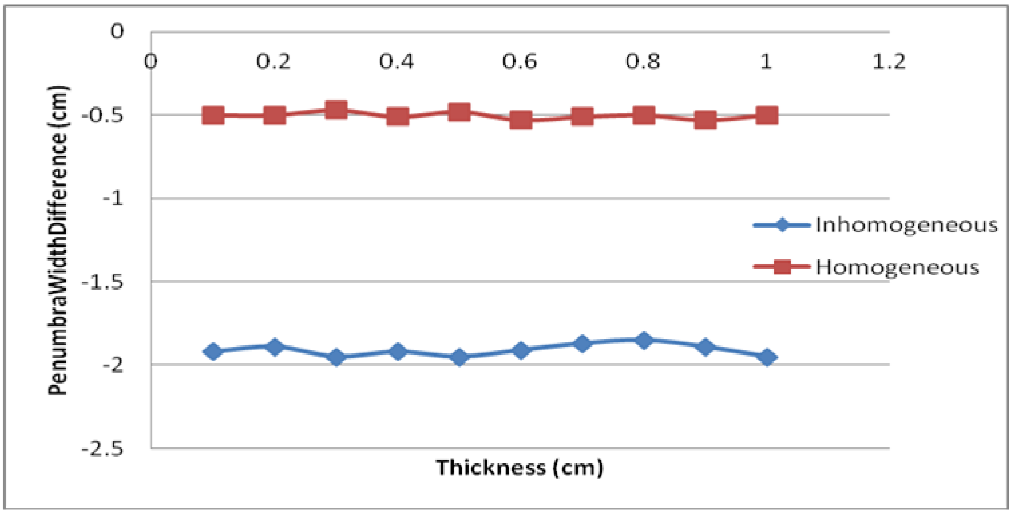

Figure 80: Penumbra Width Difference computed with respect to thickness of Homogeneous and Inhomogenities in thyroid (soft tissue) volume.

The penumbra width of the Bragg curve in both the cases, i.e. with and without presence of the thyroid medium in human phantom as shown in Figure 80 is observed to have a -1.5% shift in its value of with respect to thickness while changing from 0.1 – 1.0 cm.

4.5.3 Analytical result obtained for dose while tumor irradiation:

The effect of proton beam dose distribution to Inhomogenities existed in penetration path due to physical characteristics of proton have been computed. A slight change in its significance of dose associated with respect to the inhomogenities positioned in the volume. The dose with respect to the materials used for proton irradiation is also estimated here. So, these are analyzed by Bragg-Gray cavity theory **(Yun Ju, 2010)** which deals with stopping power of particles $D_{med} = J_g \times \frac{\overline{W}}{e} \times \left(\frac{\bar{L}}{\rho}\right)_g^{med}$, here $J_g \times \frac{\overline{W}}{e}$ is energy absorbed per unit mass, $\left(\frac{\bar{L}}{\rho}\right)_g^{med}$ is weighted ratio of mass stopping power. The stopping power is related to the electron density of media. We considered water, soft tissue and muscular skeleton materials which are having their mass stopping power values as 7.298, 6.095, 5.998 respectively.

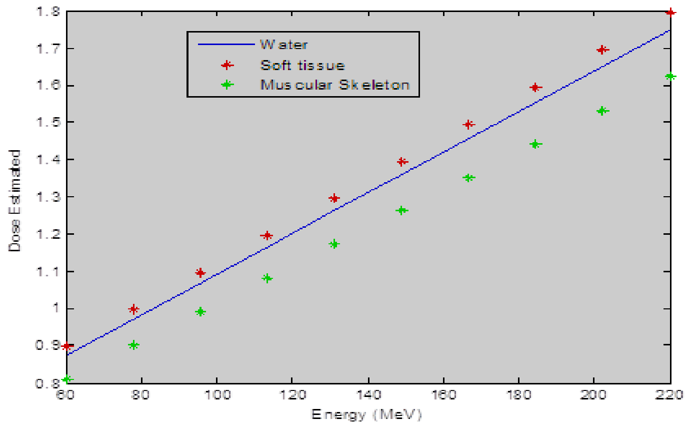

Figure 81: Dose estimated for proton beam in different materials with in an energy range from 60-220MeV

The amount of dose estimated for proton beam of incident energy ranges within 60-220 MeV in different materials i.e. water, soft tissue and muscular skeleton is shown in Figure 81. S.Guatelli *et.al*. also estimated the amount of dose deposited in human organs. But he computed for brachytherapy with a passive proton beam therapy. In order to study the high and low dose rate brachytherapy in different organs, sources like ^{192}Ir Amersham, Buchler G089 and ^{125}I were simulated.

Table 18: The Bragg curve parameters considered relative to presence of kidney (soft tissue) inhomogeneity in human (water) phantom.

Energy (MeV)	Bragg Peak (cm)			Range ((Penumbra(80%))			Penumbra (20%) (cm)			FWHM(cm)		
	INH	H	D	INH	H	D	INH	H	D	INH	H	D
65	2.2	3.1	0.9	2.8	2.9	0.1	3.3	4.4	1.1	1.5	1.2	-0.7
75	2.5	4	1.5	2.4	3.8	1.4	4.1	4.8	0.7	1.5	1.2	-0.7
85	4.5	5.3	0.8	7.2	7.6	0.4	7.8	6.2	-1.6	1.6	1.3	-0.7
95	4.7	6.5	1.8	7.7	8.1	0.4	8.5	7.9	-0.6	1.6	1.3	-0.7
105	5	8.1	3.1	8	8.4	0.4	9.1	9	-0.9	1.7	1.4	-0.7
109.2	5.9	8.9	3.9	8.7	9.1	0.4	10.3	9.8	-0.5	1.7	1.5	-0.8

Table 19: The Bragg curve parameters considered relative to presence of kidney (soft tissue) inhomogeneity in human (water) phantom. Initial energy of proton is 76.3 MeV. Thickness varied from 0.1-1.0 cm.

Thickness (cm)	Bragg Peak (cm)			Range (Penumbra (80%)) (cm)			Penumbra (20%) (cm)			FWHM(cm)		
	INH	H	D	INH	H	D	INH	H	D	INH	H	D
0.2	2.9	4.4	1.4	3.8	4.8	1	4.2	5.2	1	1.4	1.2	-0.1
0.4	2.9	4.4	1.4	3.8	4.8	1	4.2	5.2	1	1.2	1.3	0.1
0.6	2.9	4.4	1.4	3.8	4.8	1	4.2	5.3	1.1	1.3	1.3	0.1
0.8	2.9	4.4	1.4	3.8	4.8	1	4.2	5.3	1.1	1.4	1.1	-0.3
1	2.9	4.4	1.5	3.8	4.8	0.9	4.2	5.2	1	1.1	0.9	-0.2

Table 20: The Bragg curve parameters considered relative to presence of thyroid (soft tissue) inhomogeneity in human (water) phantom on varying energy												
Energy	Bragg Peak (cm)			Range (Penumbra (80%))(cm)			Penumbra (20%) (cm)			FWHM(cm)		
(MeV)	INH	H	D	INH	H	D	INH	H	D	INH	H	D
65	2.3	2.8	0.5	2.8	2.9	0.1	3.3	3.9	0.6	0.5	0.6	0.1
75	2.5	3.8	1.3	3.3	3.8	0.4	4.1	5.3	1.2	0.6	0.6	0
85	3.4	5.3	1.9	3.9	6.2	2.3	4.7	6.2	1.4	0.7	0.6	-0.9
95	4.4	6.5	2.1	4.7	7.5	2.7	5.3	7.6	2.2	1	0.7	-0.3
100	5.2	7.3	2.1	5.7	8.2	2.5	6.2	8.2	2	1.2	0.7	-0.5

Table 21: The Bragg curve parameters considered relative to presence of thyroid (soft tissue) inhomogeneity in human (water) phantom on varying thickness												
Thickness (cm)	Bragg Peak (cm)			Range (Penumbra (80%)) (cm)			Penumbra (20%) (cm)			FWHM(cm)		
	INH	H	D	INH	H	D	INH	H	D	IN H	H	D
0.2	2.2	3.3	1	2.8	3.7	0.8	4.7	4.2	-0.5	1.1	0.6	-0.5
0.4	2.2	3.3	1.1	2.8	3.7	0.9	4.7	4.2	-0.5	1	0.6	-0.4
0.6	2.2	3.3	1.1	2.8	3.7	0.8	4.7	4.2	-0.5	0.6	0.5	-0.9
0.8	2.2	3.3	1	2.8	3.7	0.8	4.7	4.2	-0.4	0.6	0.5	-0.9
1	2.2	3.3	1	2.8	3.7	0.9	4.7	4.2	-0.5	0.5	0.5	0

4.6 Dose estimation of a passive proton beam for a human phantom at different ages

This section is in continuation of the previous work discussed in section 4.5 i.e. the inhomogeneous medium impact is observed on the bragg peak and its respective parameters during proton irradiation during treatment in a tumour. The human organs which are assumed to be inhomgeneous in tumour region are positioned according to the location where the proton suitable energy range for each tumour was optimized. The significant effect of the absorbed dose of proton beam during treatment at different ages will be discussed here. The details of the phantom volumes are taken from the ***M. Cristy et.al*** report designed for OAK RIDGE NATIONAL LABORATORY (ORNL) for performing the simulation. The parameters such as dose equivalent, absorbed dose as function of depth to the target are computed. We observed that at younger age the dose deposition in the patient's tumour receives a higher dose rate whereas it gradually decreases for 10 year, 15 year and adult. In order to execute a limitation on particle interaction mechanism, one of the most important parameter i.e. step length in simulation is considered. The dose rate is observed for an accurate result w.r.t step length of the particle among the Geant4 9.3 and 9.4 versions.

The inhomogeneous medium plays an important role in effecting stopping power and range of proton beam during treatment. Proton therapy is developed for providing an improved treatment compared to IMR and other photon techniques. Protons are mainly used for curing head neck, ocular, breast and paediatric tumours (***Wilson et.al, 2005***). Due to the finite range of protons, they can deposit maximum energy at a depth in Bragg Peak for the treatment of deep seated tumours while sparing the healthy tissues surrounding it. The proton trajectories are measured under the influence of compelling field. The proton range is reliant on its incident energy and other physical characteristics of the tumour medium (***Stephen J. Dowdell et.al, 2011***). The energy loss of proton beam increases relative to the depth of the tumour volume. This leads to a form of peak at the end of its range where a high ionisation density is observed. There are also two different kinds of beam delivery techniques which involves use of active and passive devices that depends also on the geometry of the tumour. The confirmality in dose rate can be accomplished only by use of a passive proton beam where scatterer and their apertures (***S. Bhatnagar et.al***. ***2012***) but in case of active beam, the whole tumour volume is scanned. The biological efficiency of proton is higher in rate while compared to photons because of their dose rate. The energy transfer is generated by secondaries with an estimation of dose rate.

Several studies on dose deposited by these beneficial passive beams have been conducted by several groups. The dose rate of secondaries is measured by ***Binns and Hough et.al. 1997*** of a 200 MeV proton beam. **Yan *et.al.* 2002** measured the neutron equivalent doses of 1–15 mSv/Gy for a 160 MeV passive proton beam. ***Polf and Newhauser et.al. 2005*** studied the secondary neutron dose is observed to decrease from 6.3 to 0.63 mSv/Gy on a cumulative distance and the dose factor also gradually increased as function of its modulation in uncertainty. Secondary dose was measured using a passive proton beam on implementation of Monte Carlo techniques in the report given by ***Agosteo et.al. (1998)***. The neutron absorbed dose rate ranges within 3.7×10^{-7} to 1.1×10^{-4} Gy per treatment Gy. The dose deposited by secondaries i.e. obtained due to scattered photons and neutrons which is observed to be varied from 0.146 to 7.1×10^{-2} mGy. In the report by ***Roy and Sandison et.al, 2004,*** a passice beam of neutron is irradiated in an anthropomorphic phantom which is simulated in Geant4 to observe the scattered neutron equivalent dose for an incident energy of 198 MeV. A scattered neutron beam is used to compute its equivalent dose by simulating a human phantom (***Mesoloras et al 2006***). The neutron equivalent dose conducted by ***Mesoloras et.al. (2006)*** is observed to within 0.03 to 0.45 mSv/Gy and 0.1 to 0.87 mSv/Gy for a small and large field edge. ***Tayama et al (2006)*** measured neutron equivalent doses up to 2 mSv/Gy outside of the primary radiation field in a 200 MeV proton beam.

The consequence of physical and biological characteristic of proton beam irradiation radiation therapy is discussed in section 4.1. A proton beam with a passive technique which follows a Gaussian distribution (σ = 2.5 MeV) is chosen to study the dose absorbed in target volume. The beam penetrates along the z-direction in which the phantom is placed.

Energy deposition from radiation occurs as a random number of events and the measurement of such events may lead to an increased understanding of biological effect of radiation exposure. Energy deposition in this study is typically acquired as energy spectra (f (E) vs. E). These spectra can be used to determine the absorbed dose D at the point of measurement.

$$D = \frac{\int_0^\infty f(E)dE}{\rho V} \tag{46}$$

Here ρ is detector density and V is the volume.

A quality factor 'Q' is required for all ionising radiation which accounts for studying the impact of radiation on a tissue. This Quality factor (Q = 2) is used for protons in combination with the absorbed dose to give dose equivalent (H)

$$H = Q\,D \tag{47}$$

The values of Q or W_R selected by ICRP based on a review of available information regarding biology radiation exposure and calculation methods. This dose equivalent is expressed in Sieverts (Sv) unit. The quality factor is designed for radiation protection purpose. It is not intended to be used for risk assessment for radiation applications. From previous work done in section 4.4, we observed that dose distribution of proton beam in a phantom is dependent on the geometry of tumour. An equivalent dose due to secondary neutrons in pediatric and adult patients as function of patient's age, organ and field parameters are studied by ***Christina Zacharatou Jarlskog et.al.*** They observed the neutron dose to specific organs depend considerably on the patient's age and body stature. The younger the patient, the higher the dose is deposited due to neutrons. In this study as function of various ages, the dose distribution is not found for a new born (0 years) and 1 year. This is because of geometry factor. We observed that a finite Bragg curve can be determined from age of 5 year child whose volume is 22 cm^3. The dose absorbed in target volumes of phantom for various ages i.e. 5, 10, 15, and an adult are shown in Figures [82-85] given below.

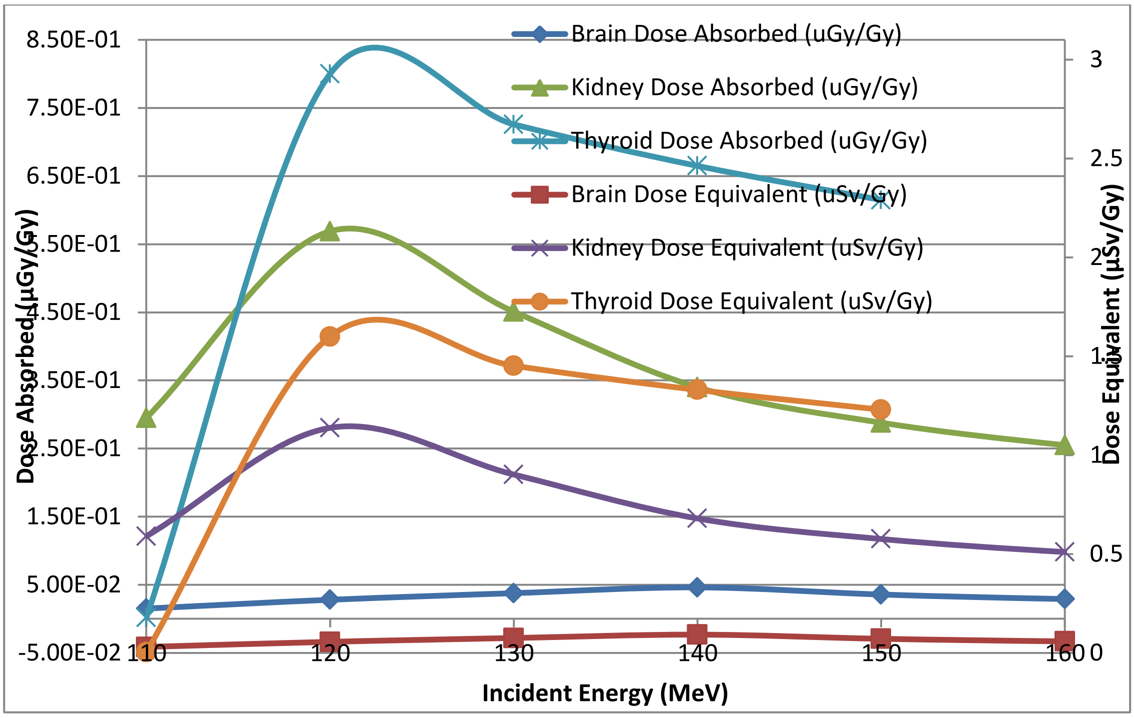

Figure 82: Absorbed Dose, Dose Equivalent as function of Incident Energy (MeV) in 5 year Child Phantom

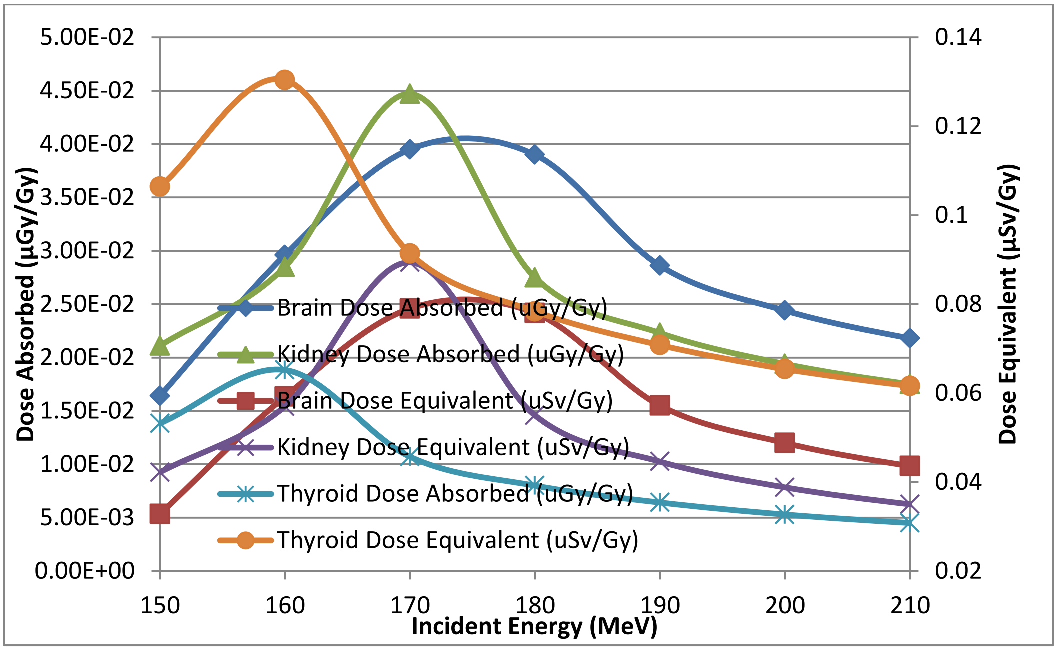

Figure 83: Absorbed Dose, Dose Equivalent as function of Incident Energy (MeV) in 10 year Child Phantom

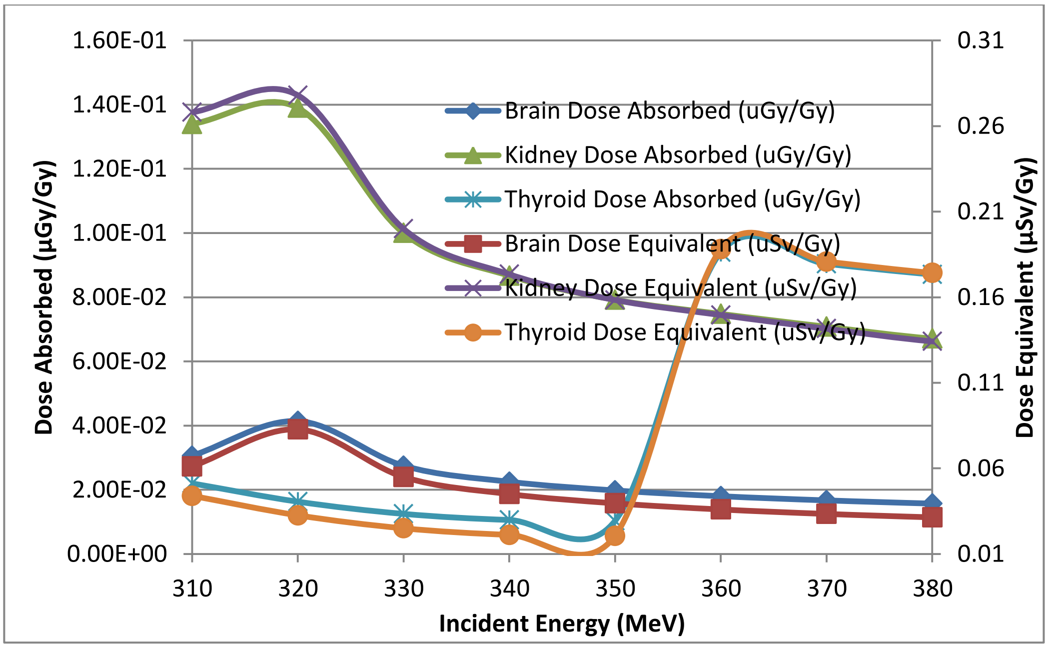

Figure 84: Absorbed Dose, Dose Equivalent as function of Incident Energy (MeV) in 15 year Child Phantom

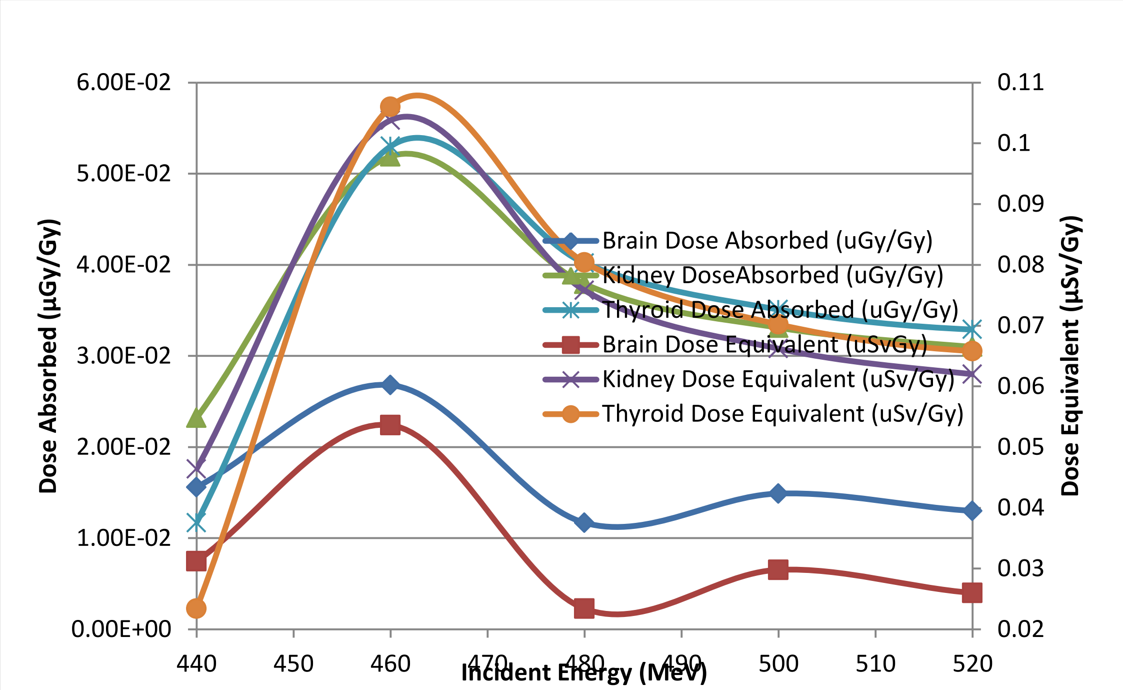

Figure 85: Absorbed Dose, Dose Equivalent as function of Incident Energy (MeV) in Adult Phantom

Two factors are considered while determining the energy range i.e. Dose Absorbed (Gy) and proton range traversed within the target volume of depth (cm). The dose equivalent parameter is also determined for each target volume using Quality factor of proton and dose absorbed in target volume as discussed in next section. The relation between absorbed dose and dose equivalent as function of depth (cm) is observed. It is shown in Figures [86-89] :

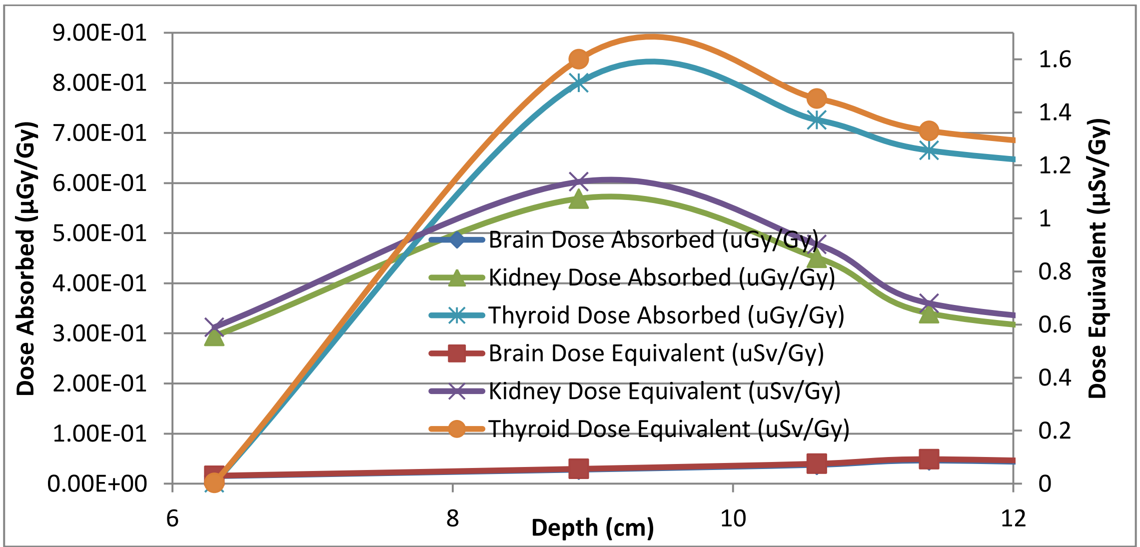

Figure 86: Absorbed Dose, Dose Equivalent as function of Depth (cm) in 5 year Child Phantom

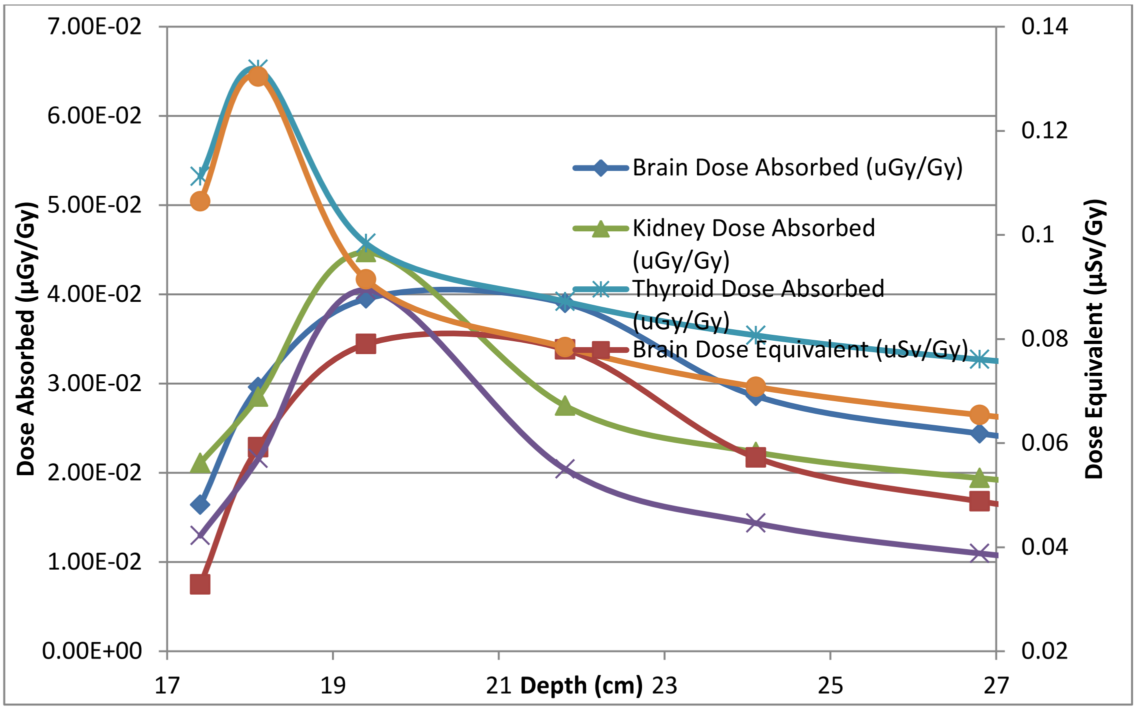

Figure 87: Absorbed Dose, Dose Equivalent as function of Depth (cm) in 10 year Child Phantom

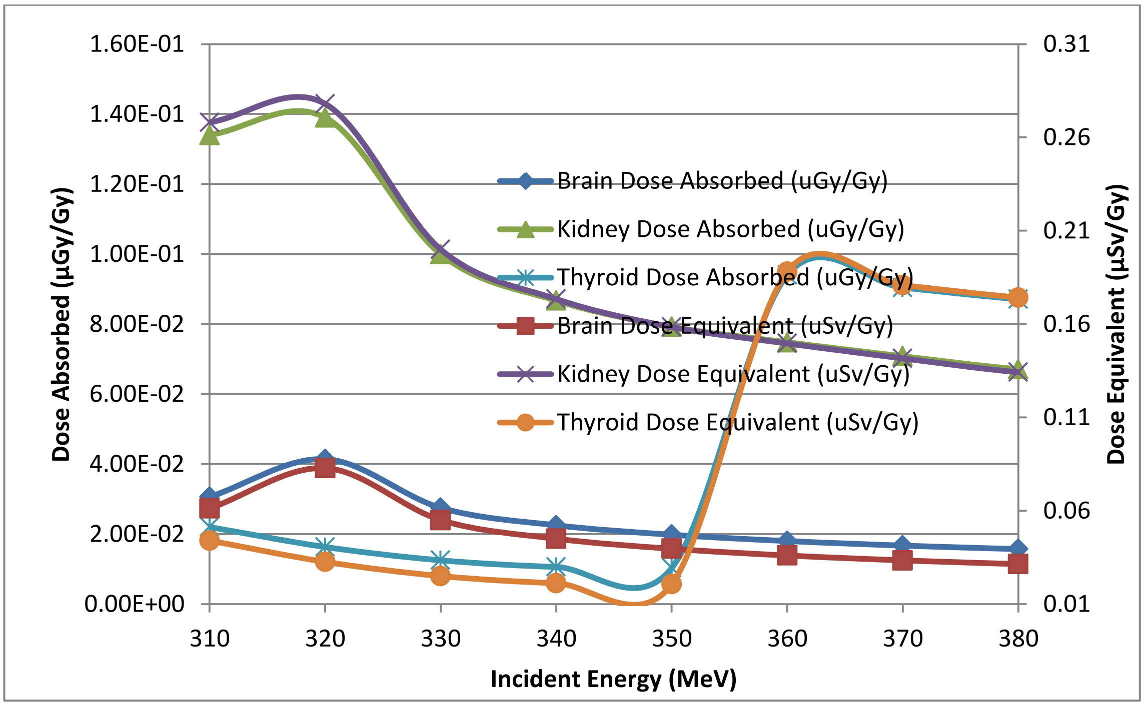

Figure 88: Absorbed Dose, Dose Equivalent as function of Depth (cm) in 15 year Child Phantom

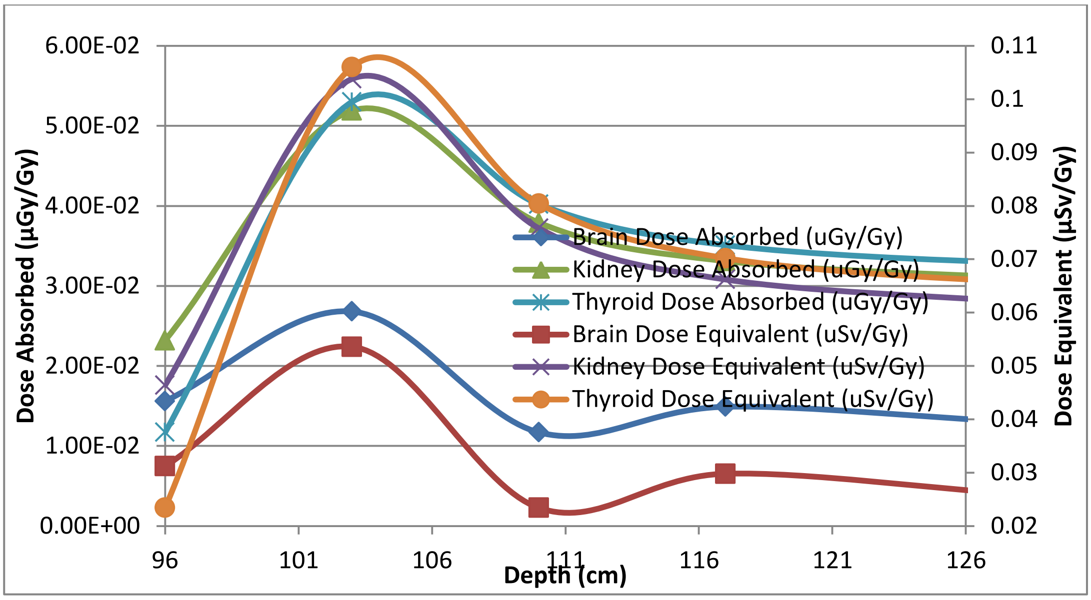

Figure 89: Absorbed Dose, Dose Equivalent as function of Depth (cm) in Adult Phantom

Table 22: Dose Equivalent for specific organs obtained from simulation

Phantom Age	Organs	Dose Absorbed (µGy/Gy)	Dose Equivalent (µSv/Gy)
5 year	Brain	(0.15 – 0.46)	(0.30 – 0.92)
	Kidney	(2.32 - 5.61)	(4.64 – 11.38)
	Thyroid	(0.77 – 8)	(0.63 – 16)
10 year	Brain	(0.13 – 0.44)	(0.32 – 0.78)
	Kidney	(0.71 – 2.47)	(1.28 – 2.89)
	Thyroid	(0.27 – 0.65)	(0.55 – 1.34)
15 year	Brain	(0.11 – 0.41)	(0.23 – 0.82)
	Kidney	(0.58 – 1.39)	(1.18 – 2.78)
	Thyroid	(0.10 – 0.94)	(0.20 – 1.38)
Adult	Brain	(0.10 – 0.26)	(0.21 – 0.53)

	Kidney	(0.23 – 0.51)	(0.46 – 1.03)
	Thyroid	(0.11 – 0.53)	(0.23 – 1.06)

From the above table 22, it shows the equivalent dose deposited during proton therapy in each organ with respect to different ages of phantoms. We observed the dose deposition is dependent on the age. It is analyzed from results that a higher dose rate is necessary for a patient at younger age than compared to rest of the cases i.e. 10 year, 15 year and Adult. In the report of ***Christina Zacharatou Jarlskog et.al.***, he considered a kidney in a four year old phantom for determining its dose rate which is observed to be varied from (0.2 – 0.5) mSv/Gy. As in this report, they used a active scanning beam where some field parameters are considered for upstream of the aperture and spread-out Bragg peak. Due to the limitation of a experimental setup in our study, we used a passive proton beam due to which the equivalent dose deposited in our study is i.e. (4.64 – 11.38) (µSv/Gy) while compared to result of ***Christina Zacharatou Jarlskog et.al.***. As stated in the report of ***Gottschalk, Paganetti et.al, 2006,*** passive scattered proton beams typically offer a limited set of different field sized impinging on the final aperture which may influence the yield due to its dependence on the ratio of the field size and aperture.

The effect of absorbed dose on target volume production of soft electrons and photons is observed on varying the step length of the proton. This is shown in table 23. Here the proton beam is fixed at energy i.e. 440 MeV and the dose rate were computed for Adult and it also compared among Geant4 9.3 and Geant4 9.4 versions. There is a negligible variation within the specific dose of organs as function of step length.

Table 23: Dose Equivalent for specific organs obtained from simulation as function of particle step length

	Geant4.9.4				Geant4.9.3		
Adult	Thyroid	Kidney	Brain	Adult	Thyroid	Kidney	Brain
Step Length(mm)	Dose Absorbed (μGy/Gy)			Step Length(mm)	Dose Absorbed(μGy/Gy)		
1	0.11	0.23	0.159	1	0.14	0.215	0.15
2	0.10	0.21	0.157	2	0.10	0.212	0.15
3	0.09	0.22	0.156	3	0.09	0.213	0.15
4	0.10	0.21	0.155	4	0.09	0.224	0.15
5	0.10	0.21	0.154	5	0.10	0.216	0.15
6	0.10	0.21	0.153	6	0.10	0.217	0.15
7	0.10	0.21	0.153	7	0.10	0.21	0.15
8	0.10	0.20	0.151	8	0.10	0.211	0.15
9	0.09	0.19	0.147	9	0.10	0.209	0.14
10	0.08	0.20	0.149	10	0.08	0.201	0.14

4.7 Summary

Monte Carlo methods are extensively used in field of radiotherapy applications for optimizing the treatment planning systems. The interfacing approach in the Geant4 toolkit developed for nuclear medicine and radiotherapy was studied. There are also ample choices of Physics models available in the toolkit to exploit the user for study of electromagnetic and hadronic physics interactions in different applications. The Monte Carlo simulation systems i.e. GAMOS because of its specific features such as voxelised phantom, advanced visualization tools, dose estimation maps allow these systems to be used for different applications such as realistic simulations in field of hadrontherapy, complicated 3D sources, emission tomography systems. Further the Geant4 studies also can be extended for different organs depicted as inhomogeneous volumes inside the human phantom. The study includes the shift in the Bragg Peak and other parameters such as Bragg Peak Position, Range, and Penumbra Width with respect to the homogeneous water phantom. We also computed the amount of dose necessary to deposit using proton and carbon ion beams for different ages of human in soft and bone tissues. For varied incident energy of proton beam, its corresponding Bragg curve and its parameters are computed. But they differ with the results regarding its peak obtained from respective bragg curves when compared with the work conducted by G.A.P Cirrone et.al (2004), L.Grevilliot et.al (2010). The expansion of this work is incorporated to study the effect of hadronic models such as Pre-compound, Hadronic_QGSP, and Hadronic_QBBC on the parameters. But on activating the inelastic interaction mechanism at higher energies, these measurements have an impact with reference to the models used. This study provides a detail discussion of computational simulation of Inhomogenities in a human phantom. It is observed that the depth dose distribution of the proton beam is dependent on the Inhomogenities and their density. The results presented in this chapter also explains that therapeutic energy range of proton beam is also dependent on the geometry of the medium. In summary, we have shown quantitatively how organ specific proton equivalent doses for 5, 10, 15 years and an adult patients vary as a function of patient age, organ, depth and step length (a Geant4 user parameter). The dose equivalent measured for radiological shielding to represent the probability of health effects at low level ionizing radiation on human phantom is computed from the obtained absorbed dose and quality factor of proton beam. We observed for an organ with respect to its volume and position in the phantom, higher proton energies are required to incident on the target for curing tumours with efficient dose rate. Most importantly, our study shows that equivalent dose for specific organ depends considerably on patient age/size. The younger and smaller the patient, the higher the dose deposited via proton therapy. It needs an attention while treating pediatric patients. As per (***BEIR et.al 2006),*** cancer risks also increases with decreasing patient age, extra attention must be paid to the treatment of pediatric patients. The absorbed dose in tumour region is dependent on the proton incident energy and also on target volume (***S.N.L Sirisha et.al. 2014***). While comparing the parameter i.e. dose equivalent for specific organs as function of patient age, in case of brain it is 0.92 µGy/Gy for 5 year patient, whereas the maximum dose rate decreases nearly i.e. 0.82 µGy/Gy, 0.78 µGy/Gy and 0.53 µGy/Gy for 10 year, 15 year and an adult. The range cut and step size of the particle are varied to observe the effect on dose absorption in target volume from the production of soft electrons and photons due to bremsstrahlung process which is involved in proton interaction. The accuracy of the data among the results is observed by comparing among Geant4 9.3 and 9.4 versions.

Conclusion

The aim of Quantum Field theory is to understand particle interactions at the lowest level and be able to combine all the fundamental forces i.e. strong, electromagnetic, weak and gravitational at a particular scale. A 'superconducting phase' where the human life survives in similar to vacuum is the main principle behind modern unified theory. The study of electroweak, strong interactions is experimentally well established theories and current active research areas. They collectively form an effective theory, "Standard Model" (SM) for study of elementary particles.

Cosmic rays are a prevailing source of information for performing high energy physics experiments. They provide energetic, correlated, particles which arrive on Earth. The particle detection and their wide-ranging influenced possessions of secondary cosmic rays have made an effective way to analyze from the educational activities which needs to be done from the feedback of students in the laboratory. The hardware required by such experiments may include the use of scintillators and fast pulse techniques for possible experimental investigations. By such devices we can carry out numerous quantitative experiments, with the prospect to enhance the physics curriculum.

Chapter 1 presents an introduction to Standard Model and physics behind study of particle interactions by using various detectors through experiment and Geant4 based simulations. It is to understand several aspects such as particle cross-section and their energy loss, response and surface characteristics of detector sensitivity which cannot be achieved by conducting an experiment. Thus, an object –oriented programming i.e. Geant4 simulation based toolkit is used to study the aspects and their principle which are mentioned above. The research work covers the study of interactions of muons, gamma rays and hadronic interactions performed in particle detectors.

Chapter 2 includes experimental studies performed using a muon telescope, which is fabricated at Cosmic Ray Laboratory (CRL), Ooty, a field station of TATA INSTITUTE OF FUNDAMENTAL RESEARCH (T.I.F.R), Mumbai. It is used to study the muon flux at Agra (27.18 N, 78.02 E) obtained from the detector setup. Cut off rigidity of 22GeV obtained for the location i.e. Agra (27.18 N, 78.02 E), India where the experiment is situated. The integral muon flux is observed to be 9.61/cm^2.sec.str with an inaccuracy of ±0.31% from analytical and experimental calculations. The efficiency of the 3-fold experimental detector setup is also calibrated from muon coincidence rate. The count rate as function of detector separation (horizontal-vertical) is determined to project decoherence curve over a period of 1 December 2014 – 16 September 2015. The characteristic study of secondary cosmic rays provided from a basic and advanced educational activity for undergraduate and PG students. The feedback (Appendix I) is also analyzed based on the conceptual questionnaire of NIM (Nuclear Instrumentation Module) experiments performed in the laboratory. The detector setup would be further interfaced with **CAEN C111C Ethernet CAMAC Controller** in order to investigate the cosmic ray muon life time with different counters and absorbers. A series of environmental correlation studies will be performed using detector station corresponds to its cosmic ray flux with atmospheric parameters for study of angular dependency of secondary muons.

Chapter 3 includes simulation of multiple scattering phenomena to observe its effect on muon interactions with different density materials. The basic architecture and features of Geant4 simulation toolkit is given in Appendix – II. The muon telescope is simulated in Geant4 to observe the response of muon and also the effect on photon yield while corresponding to various surface characteristics. The Tyvek wrapping with a polished surface of dielectric_metal interface is observed to have 96% of photon yield that reaches the sensitive region of the detector. The intensity and peak energy of gamma radiation source (Cs-137) is observed for a plastic scintillator. A scatterer in front of the gamma source is employed and its relative position is determined using rotation matrix based on Geant4. The angle between scatterer and detector is varied to understand the phenomena of Compton scattering. The work will be further extended for study of cosmic ray interaction, nuclear composition and their propagation in atmosphere by numerical simulation based on **Leaky and Diffusive model**. A detector station also should to be designed and configured at Cosmic Ray Laboratory, Ooty, India in an appropriate geometry which will be optimized using **CORSIKA** and **Geant4 Monte-Carlo simulation toolkits**.

Chapter 4 discuss the physical characteristics of particle beams in hadron therapy, its effect on curing tumors in presence of heterogeneous medium and specific dose equivalent required for patients of various ages. Physical distribution of dose curves of proton beam is studied from Geant4 simulation of the setup installed at INFN Catania for curing ocular tumours. The significance of the spectra due to secondary particles produced in interactions of 60 MeV proton beam is discussed which is relevant for study of harmful genetic adeptness and proton range in Bragg Peak (SOBP). The suitable energy range for each tumour of the human organ was optimized. The Bragg curve parameters were computed which involves its peak, range, dose rate and its uncertainty. A significant shift on an average of approx. -0.44% in the position of Bragg peak is observed for the materials i.e. muscular skeleton and soft tissue. The substantial outcome of the absorbed dose of proton beam in different ages is from the relation which is obtained between dose equivalent and absorbed dose as function of depth to target volume. The dose deposition is observed to have dependency with higher dose rate for patient who is necessary of it at younger age while compared to other cases. The study would be further extended to observe the influence of nuclear interactions in beam irradiation.

REFERENCES

A.A.Petrukhin. (2014). Muon puzzle in cosmic ray experiments and its possible solution. Nuclear Instruments and Methods in Physics Research A, 228-231.

Abgrall, N. (2016). Muon Flux Measurements at the Davis Campus of the Sanford Underground Research Facility with the {\sc Majorana Demonstrator} Veto System. Nuclear Experiment (nucl-ex), 1-14.

Abbasi, R. e. (2013). Lateral distribution of muons in IceCube cosmic ray events. Physical Review D, 87.1 (2013): 012005.

Amaldi, U. (2014). Particle Accelerators: From Big Bang Physics to Particle Accelerators. CERN, Switzerland: Springer.

Anthon lechner (2012) Investigation of the geometric accuracy of proton beam irradiation in the liver. Int J Radiat Oncol Biol Phys;82:826–33.

Asatiani et.al, (2013) The angular resolution of the GRAPES-3 array from the shadows of the Moon and the Sun. Astropart Phys **33** 97-107. doi: 10.1016/ j.astropartphys.

Allkofer (2012), 13a In-beam quality assurance using induced β+ activity in hadrontherapy: a preliminary physical requirement study using Geant4 Phys. Med. Biol. **57** 6497–518

Allkofer, J et.al (2014), Relativistic quantum molecular dynamics approach to nuclear collisions at
ultrarelativistic energies Nucl. Phys. A **498** 567–76

Abebe Getachew (2007), Did the 28 October 2003 solar flare accelerate protons to 20GeV A study of the subsequent Forbush decrease with the GRAPES-3 tracking muon telescope. Phys Rev D **74** 052003 1-15. doi: http:// dx.doi.org/10.1103/PhysRevD.74.052003

Agosteo. (1998), Atmospheric Cosmic Rays and Solar Energetic Particles at Aircraft Altitudes. Env. Int., 22(1), S9-S44.

B.Mitrica. (2015). New cosmic rays experiments in the underground laboratory of IFIN-HH from Slanic Prahova, Romania. AIP Conf. Proc., 188.

Blokh et.al, (2015) Validation of recent Geant4 physics models for application in carbon ion therapy Nucl. Instrum. Methods B **268** 2343–54

B´en´, S. (2013). Air shower simulation for background estimation in muon tomography of volcanoes. Geosci. Instrum. Method. Data Syst, 11-15.

Bellotti et.al, (2016) The Standard Model of Electroweak Interactions. High Energy Physics - Phenomenology, CERN-2012-001, pp.1-50.

Bellotti et.al, (2013) New LHC results suggest there's a flaw in the standard model. Science alert.

Bachri, A. (2011). Analysis of Gamma rays and cosmic ray muons wirh single detector. Journal of Arkansas of sciences, 27-32.

Bahr, B. (2016). Standard Model of Elementary Particles. ISBN: 978-3-662-49507-0: Springer, pp 212-215

Blasi, (2013) "The LAGUNA Design Study: towards giant liquid based underground detectors for neutrino physics and astrophysics and proton decay searches,"Acta Physica Polonica B, vol. 41, pp. 1727–1732.

Bogdanov, A. (2012). "Energy spectrum of cosmic ray muons in ∼100 TeV energy region reconstructed from the BUST data". Astroparticle physics , pp:224.

Burigo, (2013) 12C nuclear reaction measurements for hadrontherapy 12th Int. Conf. on Nuclear Reaction Mechanisms (Varenna, Italy) pp 531–7

Bourngaleb, (2011) The reliability of proton-nuclear interaction cross-section data to predict proton-induced PET images in proton therapy Phys. Med. Biol. **56** 2687–98

Binns Hough (1997) Incidence of cancer among Finnish airline cabin attendants, 1967-92. Brit. Med. J., 311, 649-652.

BEIR (2006) Monte Carlo simulation of proton-induced cosmic-ray cascades in the atmosphere. Lawrence Livermore National Laboratory, Livermore, CA, Tech. Rep. UCRL-TM-229452

Carlson et.al, (2012) GATE as a GEANT4-based Monte Carlo platform for the evaluation of proton pencil beam scanning treatment plans Phys. Med. Biol. **57** 4223–44

Carmi, D. (2012). Interpreting LHC Higgs Results from Natural New Physics Perspective. Journal of High Energy Physics, 07 (2012) 136 [arXiv:1202.3144].

Cecchini. (2012). Atmospheric muons: experimental aspects. Geosci. Instrum. Method. Data Syst, 185-196.

Christina Zacharata Jarlskog (2008) "Assessment of organ specific neutron equivalent doses in proton therapy using computational whole body age dependent voxel phantoms", Phys. Med Biol. 2008 February 7; 53(3): 693-717

Clarkson, A. (2014). GEANT4 simulationofascintillating-fibretrackerforthecosmic-ray muon tomographyoflegacynuclearwastecontainers. NuclearInstrumentsandMethodsinPhysics Research A, 746; 64–73.

Collaboration, A. (2012). Observation of a new particle in the search for the Standard Model Higgs boson with the ATLAS detector at the LHC. Phys. Lett. B, 716 (2012) 1 [arXiv:1207.7214].

Collaboration, (2014) "Amobile detector for measurements of the atmospheric muon flux in underground sites," Nuclear Instruments and Methods in Physics Research A, vol. 654, pp. 176–183, 2011.

Cortes, M. L. (2014). BC404 scintillators as gamma locators studied via Geant4 simulations. Journal of Instrumentation, JINST 9 C05049.

Coutu et.al, (2011) Spontaneous Abortions Among Finnish Flight Attendants. J.Occup. & Env. Med., 41(6), 486-491

CRM Experiment, (2013) The nuclear physics of muon capture Phys. Rep. **354** 243

C. Grupen, (2012) Cosmic-ray intensity fluctuations at sea level Phys. Rev. **96** 1116

C. Grupen, (2014) Temperature effect of the muon component underground and pion attenuation length Nuovo Cimento B **51** 525 hyperphys-phy-astr.gsu.edu

DJ Thomsan, (2012) Cosmic Rays from Galactic Gamma-Ray Bursts. Astrophys. J. L., 628, L21-L24.

D. Kosenko, (2014) Improved radiotherapy for primary and secondary liver cancer: stereotactic body radiation therapy. Anticancer Res ;32:649–55.

Dayananda, M. A. (2013). Correlation Studies of Cosmic Ray Flux and Atmospheric and Space Weather. ScholarWorks @ Georgia State University.

Dosanjh, M. (2016). Medical Applications at CERN and the ENLIGHT Network. FRONTIERS IN ONCOLOGY, 6-9.

DepawnN, (2013) comparison of secondary neutron dose in proton therapy resulting from the use of a tungsten alloy MLC or a brass collimator system" Med. Phys. **39** 2306–9

Ellis, J. (2015). The effective Standard Model after LHC Run I. Journal of High Energy Physics, 157. doi:10.1007/JHEP03(2015)157.

Franke et.al, (2010) Secondary beam fragments produced by 200 MeV/u ^{12}C ions in water and their dose contributions in carbon ion therapy New J. Phys. **10** 075003

Fix, (2013) Nuclear reactions in Monte Carlo codes Radiat. Prot. Dosim. **99** 29–38

Grassberger C. (2011). Variations in linear energy transfer within clinical proton therapy fi elds and the potential for biological treatment planning. Int J Radiation Oncol Biol Phys, Vol: 80:1559-66.

Gupta, S. (2014). High Energy Astroparticle Physics at Ooty and the GRAPES-3 Experiment. Proc Indian Natn Sci Acad, 80 No. 4, pp. 827-876.

Golden et.al, (2009) Fast neutrons produced by nuclear fragmentation in treatment irradiations with 12C beam Radiat. Prot. Dosim. **110** 595–600.

Greisen (2012) Dose profile monitoring with carbon ions by means of prompt-gamma measurements Nucl. Instrum. Methods B **267** 993–6

Grider (2008) Cosmic Rays at Earth (Amsterdam: Elsevier)

Griffiths D (2008) Introduction to Elementary Particle Physics

Geant4 Collaboration et.al, Physics Ref Manual 9.4, (2012)

Geant 4 Collaboration et.al, User Manual (2015)

Garg, (2014) "The energy spectrum and Rotational matrix based study of gamma rays", ICTCS '14 Proceedings of the 2014 International Conference on Information and Communication Technology for Competitive Strategies, Article No. 24 ACM, New York, USA ©2014 ISBN: 978-1-4503-3216-3 doi:10.1145/2677855.2677879.

GAP Girrone (2004) Monte Carlo simulation of proton-induced cosmic-ray cascades in the atmosphere. Lawrence Livermore National Laboratory, Livermore, CA, Tech. Rep. UCRL-TM-229452.

Gottschalk, Paganetti (2006) , "Neutron dose in scattered and scanned proton beams: in regard to Eric J. Hall (Int. J Radiat Oncol Biol Phys 2006; 65: 1-7)". Int. J. Radiat. Oncol. Biol Phys 2006; 66: 1594.

H.Paul Nucl. Instr (1991) The energy spectrum of cosmic-ray induced neutrons measured on an airplane over a wide range of altitude and latitude. Rad. Prot. Dos., 110(1-4), 387-392. doi: 10.1093/rpd/nch216.

Hanitra Szymanowski (2013) Dose–volume histogram analysis for risk factors of radiation-induced rib fracture after hypofractionated proton beam therapy for hepatocellular carcinoma. Acta Oncol 2013;52:538–44.

ICRU reports 49, (1993) Long term time variability of cosmic rays and possible relevance to the development of life on Earth. Surveys in Geophys., 31(4), 383-398. doi: 10.1007/s10712-010-9097-8

Joyce, A. (2015). Beyond the cosmological standard model. Physics Reports, Volume 568, 22 March 2015, Pages 1–98.

James F , (2011) A new measurement of the intensity of cosmic-ray ionization at sea level J. Geophys. Res. **71** 4651

Kojima, H. e. (2015). Dependence of cosmic ray intensity on variation of solar wind velocity measured by the GRAPES-3 experiment for space weather studies. Physical Review D, 91.12 (2015): 121303.

Krizmanic et.al, (2011) Gamma electron vertex imaging and application to beam range verification in proton therapy Med. Phys. **39** 1001–5

Kitamura, (2011) Investigating the accuracy of the FLUKA code for transport of therapeutic ion beams in matter Phys. Med. Biol. **51** 4385–98

K Jourde, (2016) Overview of the integrated global radiosonde archive J. Clim. **19** 53

K Gwosch (2013) A tracking Compton-scattering imaging system for hadron therapy monitoring IEEE Trans. Nucl. Sci. **57** 144–50

L. Grevilliot (2010) Optimization of GEANT4 settings for proton pencil beam scanning simulations using GATE Nucl. Instrum. Methods B **268** 3295–305

M, J. (2010). Patient statistics per end of 2010: Hadron therapy patient statistics. Retrieved from http://ptcog.web.psi.ch/.

Mendez, J. R. (2015). Improved efficiency in Monte Carlo simulation for passive-scattering proton therapy. Physics in Medicine & Biology, Phys. Med. Biol. 60; 5019–5035.

Macdonald, F. (2015, August 15). The LHC has discovered a brand new class of particles. Science alert.

Mauro, (2014) Modeling high-energy cosmic ray induced terrestrial muon flux: A lookup table. Rad. Physics & Chem., 80(6), 701.

Mitrica. (2013). A Mobile Detector for Muon Measurements based on Two Different Techniques. 2013, Article ID 256230, 7 pages.

M. Cristy (2013) Sequential phase I and II trials of stereotactic body radiotherapy for locally advanced hepatocellular carcinoma. J Clin Oncol 2013;31:1631–9.

Mesoloras (2006) Astrophysical Ionizing Radiation and the Earth: A Brief Review and Census of Intermittent Intense Sources. Astrobiology, 11, 343-361, doi:10.1089/ast.2010.0603.

Nagashima, Y. (2012). Beyond the Standard Model of Elementary Particle Physics. CERN: Wiley-vch.

Narasimham, (2010) Forbush decreases and turbulence levels at coronal mass ejection fronts. Astron Astrophys **494** 1107-1118. doi: http://dx.doi.org/10.1051/ 0004-6361.

Newhauser, W. D. (2015). The physics of proton therapy. Physics in Medicine and Biology, Phys. Med. Biol. 60 (2015) R155–R209.

Overholt, A. C. (2015). A link between solar events and congenital malformations: Is ionizing radiation??

PDG et.al, (2015) K.A. Olive et al. (PDG), Chin. Phys. C38, 090001

PDG et.al, (2016) K.A. Nakamura et al. (PDG), JP G 45, 075056

PK Mohanty (2014) Particle Acceleration in Impulsive Solar Flares. Space Sci Rev **86** 79-105. doi: 10.1023/ A:1005066209536

PS Satsangi, (2013) “Towards Integrating Arts (First-Person Spiritual-Cognitive-Material Phenomenology) and Science (Third-Person Neuro-Physical Environmental-Cognitive Correlates) of Consciousness : The Dayalbagh Vision”, Vision Talk at the Inaugural

Session of The Twentieth International Conference on Toward a Science of Consciousness (TSC 2013), Dayalbagh Educational Institute, Dayalbagh, Agra, March 3-9, 2013.

Paganetti, H. (2013). Biological Considerations When comparing proton to photon therapy. Radiation Oncology, 1053-4296/13/$ - © 2013 Elsevier.

Park, S. H. (2011). Basics of particle therapy I: physics. Radiation Oncology Journal, 29(3):135-146, http://dx.doi.org/10.3857/roj.2011.29.3.135, pISSN 2234-1900 · eISSN 2234-3156.

Poulson, D. e. (2016). Cosmic ray muon computed tomography of spent nuclear fuel in dry storage casks. arXiv , arXiv:1604.08938 (2016).

Pflugfelder et.al (2010) Particle beam radiotherapy with a surgical spacer placement for advanced abdominal leiomyosarcoma results in a significant clinical benefit. J Surg Oncol 2010;101:97–9.

Polf & Newhauser (2005) Past Galactic GRBs, and the origin and composition of ultrahigh-energy cosmic rays. AIP Conference Proceedings; 1279(1), 242.

Ralph Engel, (2009) Altekruse SF, McGlynn KA, Reichman ME. Hepatocellular carcinoma incidence, mortality, and survival trends in the United States from 1975 to 2005. J Clin Oncol 2009;27:1485–91.

Ryazhskaya, (2009) Physics settings for using the Geant4 toolkit in proton therapy IEEE Trans. Nucl.
Sci. **55** 1018–25

Roy & Sandison (2004) Breast cancer risk among Finnish cabin attendants: a nested case-control study. J. Occup. Env. Med., 62, 488-493.

Riggi, F. (2014). An extensiveairshowertriggerstationforthe Muon Portal detector. Nuclear Instruments and Methods in Physics Research A, 142-149.

Riggi, S. (2011). GEANT4 simulation of plastic scintillator strips with embedded optical fibers for a prototype of tomographic system. Nuclear Instruments and Methods in Physics Research A, 583-590.

Riggi, S. (2013). Muon tomography imaging algorithms for nuclear threat detection inside large volume containers with the Muon Portal detector. Nuclear Instruments and Methods in Physics Research A, 59.

R, Z. (2013). Comparison of risk of radiogenic second cancer following photon and proton. Physics in Medicine and Biology, Phys. Med. Biol. 58 807–23.

SNL Sirisha et.al, (2014) Preliminary Studies of Muon Telescope” presented in IARPNC-2014: 31. IARP National Conference on Advances in Radiation Measurement Systems and Techniques; Bhabha Atomic Research Centre; Mumbai and published in conference proceedings by Indian Association for Radiation Protection (IARP), Reference No: 46053360, The International Nuclear Information System (INIS) Volume:26, INIS Issue:23, 2014.

SNL Sirisha et.al, (2014) "Geant4: GATE and GAMOS – A systematic Implementation of HEP Simulation toolkit to oncology therapy", presented in "IEEE Student's technology Symposium – 2014", IIT Kharagpur, 28Feb-2March, 2014 organized by IEEE Student Branch, IIT Kharagpur and IEEE Kharagpur Section and published in IEEE Xplore, ISBN 978-1-4799-2608-4/14©2014 pp.25 – 30.

Sirisha et.al, (2016) "Study the correlation of muon paddle efficiency with temperature, pressure, decoherence curve and effect of Multiple Scattering Physics in Geant4 based detector simulation" , International Journal of Current Research Vol. 8, Issue, 09, pp.39537-39545, September, 2016

Sirisha et.al, (2011) Study of photon yield in a plastic scintillator embedded with wave length shifting fiber. International Conference on Agile Manufacturing, 2011, December 19-22.

Sonali Bhatnagar, S. S. (2014). "Stopping Power of Proton Beam in Water Phantom: A Simulational Study", Recent Advancements in System Modelling Applications, Lecture Notes in Electrical Engineering 188, DOI: 10.1007/978-81-322-1035-1_8, Springer India

Schwartz, M. D. (2014). Quantum Field Theory and the Standard Model. Harvard University: Cambridge University Press, ISBN 978-1-03473.

Schneider (2008) Quantitative assessment of the physical potential of proton beam range verification with PET/CT Phys. Med. Biol. **53** 4137–51

Shen & Chiang (2014) Monte Carlo simulations of prompt gamma emission during carbon ion irradiation IEEE Trans. Nucl. Sci. **57** 2768–72

Suh, (2011) Real-time prompt gamma monitoring in spot-scanning proton therapy using imaging through a knife-edge-shaped slit Phys. Med. Biol. **57** 297–308

S. Guatelli et.al (2007) Proton therapy – a systematic review of clinical effectiveness. Radiother Oncol 2007;83:123–32.

Stephen J Dowdell 2011 Terrestrial effects due to possible astrophysical sources of an AD 774-775 increase in ^{14}C production. Geophys. Res. Lett., 40, 1-4. DOI: 10.1002/grl.50222.

S. Bhatnagar (2012) "Study for Stopping Power of Proton in Different materials – A Geant4 Simulation", Proceedings of the DAE Symp. on Nucl. Phys. 57 (2012).

T. Aso et.al, (2010) Overview of research on aircraft crew dosimetry during the last solar cycle. Rad. Prot. Dos., 136, 244-250.

Tayama (2006) "Measurement of neutron dose distribution from a passive scattering nozzle at the Proton Medical Research Centre", Nucl. Instr. Methods., Phys. Res. A 2006; 564:532-536.

Thompson, (2011) Monte-Carlo simulations to support start-up and treatment planning of scanned proton and carbon ion therapy at a synchrotron-based facility Phys. Med. Biol. **57** 3759–84

Thompson, L. (2013). A Head and Neck Simulator for Radiology and Radiotherapy. IEEE TRANSACTIONS ON NUCLEAR SCIENCE, 60;3.

Wilson et.al, (2005) Long term time variability of cosmic rays and possible relevance to the development of life on Earth. Surveys in Geophys., 31(4), 383-398. doi: 10.1007/s10712-010-9097-8

Yan et.al, (2002) Radiation Environment in the Stratosphere. Rad. Prot. Dos., 48, 5-20.

Yun, Jun (2010) Influence of lipiodol agent on proton beam range in radiotherapy planning using computed tomography for hepatocellular carcinoma. Int J Radiat Oncol Biol Phys 72:687–94.

Yu-Cheng, W. e. (2013). Measurement of cosmic ray flux in the China JinPing underground laboratory. Chinese physics C, 37.8 (2013): 086001.

Yun Hokim, (2012) Monte Carlo study of neutron dose equivalent during passive scattering proton therapy Phys. Med. Biol. **52** 4481–96

Zohar, E. (2016). Particle physics: Quantum simulation of fundamental physics. Nature, volume: 534, 480-481, doi:10.1038/534480a.

Zahra, (2011) Measurement of neutron spectra generated by a 62 AMeV carbon ion beam on a PMMA phantom using extended range Bonner sphere spectrometers Nucl. Instrum. Methods A **681** 110–5

http: antares.in2p3.fr/users/bailey/thesis/html/node/73.html

Appendix - I

QUESTIONNAIRE and ANALYSIS FROM POST GRADUATE STUDENTS

The preliminaries which are discussed till now are also performed in M.Sc. lab and the conceptual understanding of experiment by the students was also analyzed. It comprises of abstract questions relative to scintillation mechanism, PMT significance, experimental techniques, coaxial cable concepts, signal transmission, noise suppression, trigger level and particle interactions. The feedback from the students on these above topics is obtained from the following choice i.e.

(a) Appreciable (b) Enough (c) relatively (d) not a single thing.

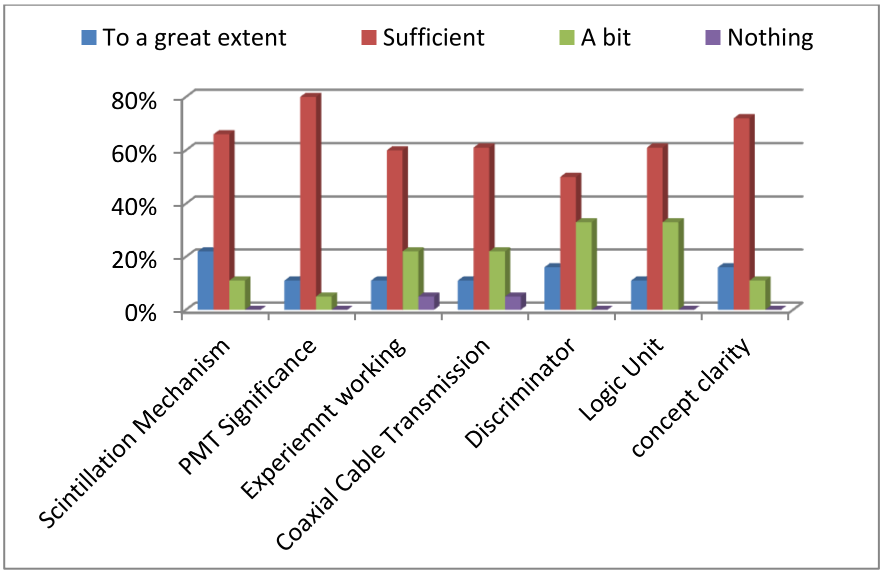

Figure 1: Students feedback in understanding the concepts of the experiment

On considering the student feedback, it is observed from the graph (figure 1) that the response on understanding the concepts of the experiment are varied as given in Table 1:

Basic Understanding	In terms of Percentage
Scintillation Mechanism	66%
PMT significance	83%
Experiment	61%
Coaxial Cable Transmission	60%

Discriminator	59%
Logic Unit	60%
Concept Clarity	72%

The next response is to choose the experiment which is more flexible to use and understand

a. GM counter b. NaI - Gamma ray spectroscopy

c. NaI - Multichannel analyzer d. Plastic scintillator – Nuclear Instrumentation Module

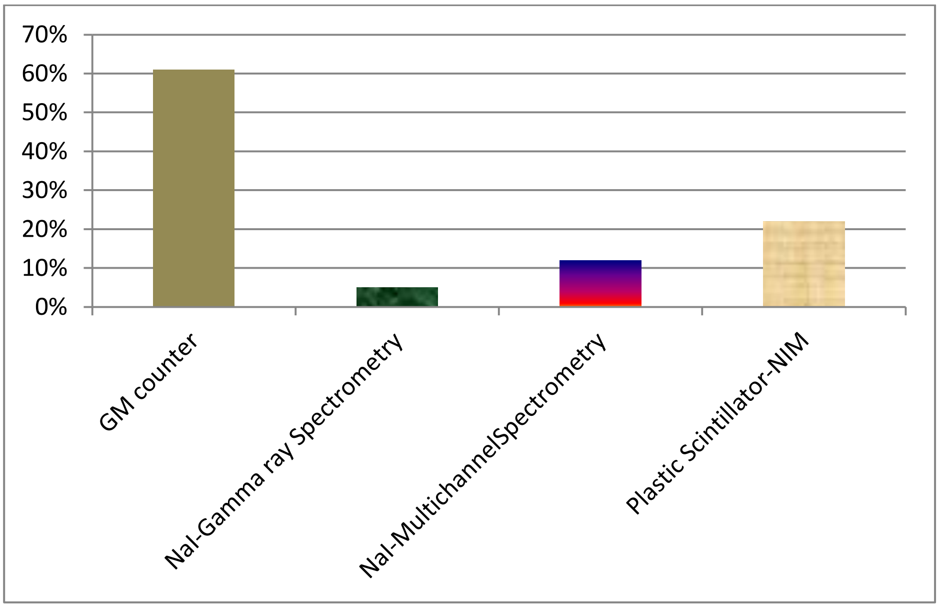

Figure 2: Students feedback after performing the experiments in the laboratory

Among the experiments which are performed by students in the laboratory, as shown in graph (figure 2), 61% of the students felt GM counter is more userfriendly where as it is remarkable that 22% of the class are comfort with the usage of NIM based plastic scintillator experiment which is presently studied in this paper.

1. Which one do you think is more preferable for study of cosmic rays?

a. NaI b. Plastic Scintillator

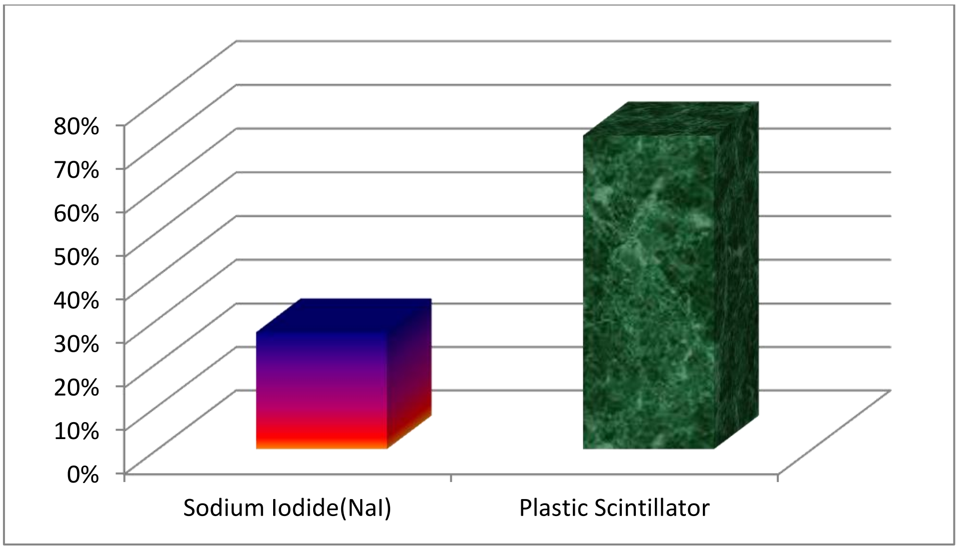

Figure 3: The feedback of students in using the plastic scintillator and Sodium Iodide (NaI) for study of cosmic rays

While comparing the organic and inorganic detectors (as shown in graph (figure 3)) which are present in laboratory for study of cosmic rays, 72% of the students opted for plastic scintillator which is suitable got cosmic ray study.

2. Among the techniques used, which is preferable for studying the efficiency of detectors

a. Pulse Height Discrimination b. Coincidence Technique

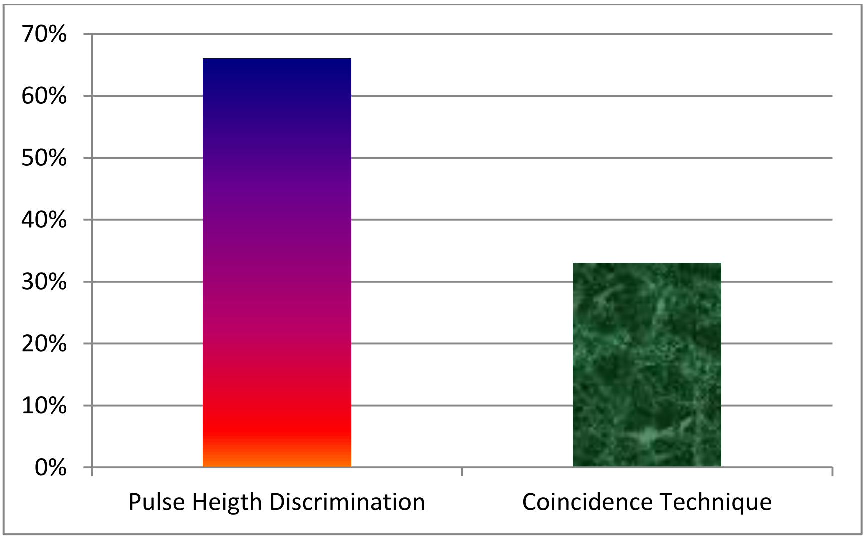

Figure 4: The technique suitable to determine efficiency of detectors from students rating of their opinion

The two techniques i.e. pulse height discrimination and coincidence technique when compared for determining the efficiency of detectors (as shown in graph (figure 4)), 66% of the students opted for pulse height discrimination where as 33% opted for coincidence technique.

11. Among the equipments given, which can cause main source for errors/noise in the experiment?

a. Scintillator b. Coaxial Cables c. PMT d. Discriminator

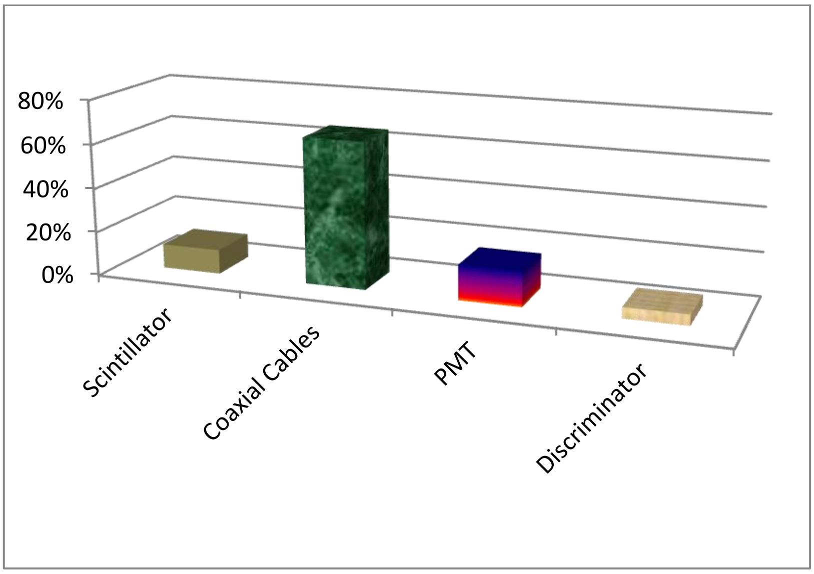

Figure 5: Students feedback regarding the noise/error source in experiment within the equipments

When discussed for possible error/noise source in experiment as shown in graph (figure 5)), 66% of the students gave their feedback for coaxial cables and 16% opted for PMT as a main source of noise in experiment.

Appendix - II

APPLICATION OF QUANTUM FIELD THEORY TO THE STUDY OF PARTICLE INTERACTIONS – GEANT4 (GEOMETRY AND TRACKING 4)

The experiments for modern nuclear physics fields are leading to increasing challenge of extensive, precise and inclusive simulations of the detectors. This is due to demand of their intense size and detector sensitivity which are operated by essential computer systems. In response to their, Monte-Carlo methods with object – oriented simulation toolkits have been developed to provide a manifold of software components. The rise of quantum mechanics helped us to correlate the radiation interactions using their cross-sections where random sampling is applied to determining the probability. The basic strategy from random variables, probability density function (PDF) and its moments, significance of variance. There are also ample set of algorithms which are available to understand the particle transport, deflection and displacement of particles, global effects of collisions such as scattering theories, angular distribution and tracking of particles. The above physics can be implemented by use of Poisson stochastic process and condensed simulation algorithms such as EGS4 and ETRAN. The high energy simulation codes such as Geant4 follows mixed simulation method where it can simulate hard and soft collisions. It also reduces the dependency of angular distribution of particle tracking on step length which results in decrease of uncertainties in results. In the upcoming subsections, the detail overview and architecture of Geant4 Monte-carlo object oriented toolkit are discussed.

DESIGN OVERVIEW AND ARCHITECTURE

Geant4 is a standalone application that covers all aspects of the simulation process such as geometry, materials, particle deflection, generation of a event, particle tracking and its physics which includes electromagnetic, hadronic interactions, detector response, generation and storage of data, user interface which helps in visualization of detector and particle trajectories at different levels of aspects. The hierarchical structure for the toolkit is shown in Figure 1:

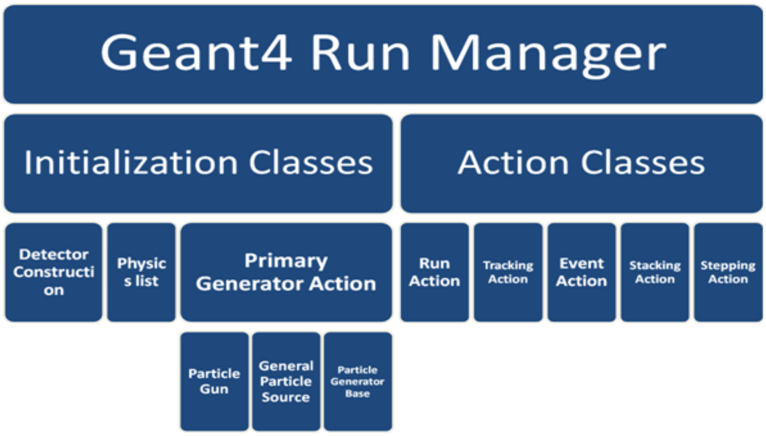

Figure 1: Hierarchy system in Geant4 toolkit

SOFTWARE PROCESS

Object-Oriented Analysis (OOA), Design (OOD) and code implementation define the major phase of software development process in an OO methodology. OOA and OOD provide an object-based decomposition of a software system into smaller and smaller parts, each of which can be refined independently. They also offer a set of logical and physical models with which the developer can understand both the entire architecture and the class design. To construct such models, OOA and OOD provide a coherent set of processes.

There are a set of requirements for the methodology of which the essential points are as follows: (1) the process must be flexible, (2) it should provide a way to decompose a system not only for code implementation, but also for analysis and design, (3) models, notations and tools are necessary for exchange of ideas to design, (4) there should be incremental development strategy, (5) it should provide a reverse engineering capability to ensure a way for the evolution of the methodology.

THE KERNEL

The essential capabilities required in the Geant4 Kernel are run and event management, region dependent production thresholds and variance reduction. The configuration of a simulation setup is controlled by run manager system in Geant4. It reads the primary events which are stored in a high energy physics (HEP) standard event generator format. It also handles track vectors which can combine different sources of primary particles. There are optional helper classes which provide the information like a primary vertex, primary particle, an event and a region. The Initialization classes associated in Geant4 architecture (Figure 11), customize the user requirements such as setting up the geometry, event kinematics, physics processes and User Action classes perform the run and event processing, event verbosity which controls the order of primary and secondary particles tracking in the detector. The geometry module is a key component of the toolkit. We begin with the study of the geometrical design presented in Geant4 as shown in Figure 2.

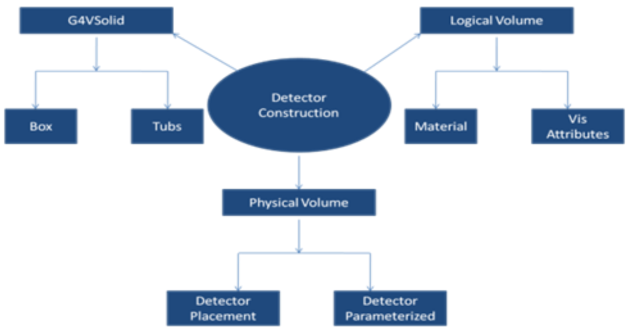

Figure 2: Detector Construction Module.

It allows the design of geometrical structure of simple and complex ranging from one up to hundreds of thousands of volumes of the LHC experiments, human phantoms for medical applications, space crafts and planets for simulation in space environment can also be modeled. The navigation class is one of its significant features. Repeated volumes can be defined by replicas of different sizes where the constructed solid geometry (CSG) volumes which include boxes, tubes, cones and polyhedron can be sliced along appropriate axis. Several volumes can be modeled using Geant4 parameterization. For each volume the position, rotations, material, volume shapes and dimensions can be changed for each volume.

PHYSICS PROCESSES

The Geant4 assigns multiple processes and models as alternatives to the same physical processes from which the user can choose at the run time. The most significant feature of this software system is an abundant set of physics models to handle the interactions processes (electromagnetic, elastic scattering, inelastic scattering of protons and neutrons, inelastic scattering of ions) of particles with matter across a very wide energy range. Many previous software systems such as EGS4, ETRANS are having limitations in adding new or variant physics models. It became difficult to implement this feature due to the increasing size, complexity and inter dependency of procedure-based code. In Geant4 toolkit, the use of system objects has allowed to manage complexity and limit dependencies by defining a uniform interface and a common organizational principle for all physics models. The physics list in Geant4 comprises of four modules associating the following types of interactions: (a) electromagnetic, (b) elastic scattering, (c) inelastic scattering of protons and neutrons, (d) inelastic scattering of heavier ions as shown in Figure 3 given below.

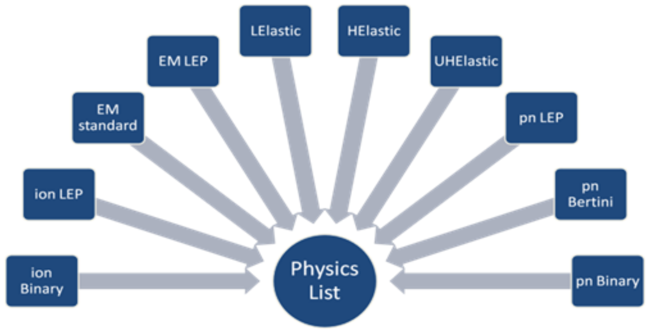

Figure 3: Structure of Modular Physics list

The processes and models (Figure 4) included in Geant4 toolkit were: Standard electromagnetic model, LEP (Low energy parameterized) electromagnetic model, three implementations of low energy parameterized nuclear elastic model (LElastic, HElastic and UHElastic), Binary cascade model for the inelastic scattering of protons, neutrons and heavier ions (pnBinary and ionBinary), Bertini cascade model developed for the inelastic scattering of protons and neutrons, low energy parameterized for inelastic nuclear scattering of ions. The scattering of light ions can be simulated by low energy parameterized model in ion Binary module. There are also additional models registered for low energy nuclear inelastic scattering (composite nucleus and thermalized nucleus decays) and for implementation of neutron induced interactions below 20 MeV, G4NeutronHP model is developed. Here the modeling of neutron interactions has its impact on computation of secondary dose calculations.

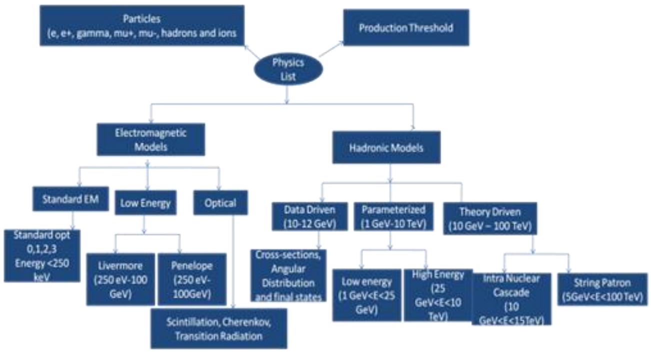

Figure 4: Physics Models for Electromagnetic and Hadronic Processes in Geant4

The "Standard" electromagnetic package is an analytical model that derives directly from Quantum Electro Dynamics (QED) calculation and describes the interactions of photons and all charged particles down to 1 keV. The energy loss of leptons is studied in Standard model using Bethe-Bloch formula < 2 MeV, whereas above this level (>2MeV) the ionization is analyzed by the low-energy parameterized model. It is initially focused on high energy physics experiments providing a fast computation but is less accurate for keV energies. The "low energy" was developed for medical and space applications with more CPU time consumption.

The hadronic models result in collection of cross-section data sets to build its own physics list. There are three cascade models: the Binary cascade model, the Bertini model and Low-energy parameterized models are used for simulation of inelastic nuclear scattering in a hadronic collision which gives rise to an intra-nuclear cascade. A Pre-equilibrium phase is automatically evoked by the intra-nuclear cascade which comprises of two models. One of these, the Pre-compound model is used for implementation of the inelastic scattering, particularly for incoming particle of energies below 100 MeV. It is based on the Griffins semi-classical description of composite nucleus decay. This pre-compound model is invoked by binary cascade in the code. The other is Pre-equilibrium model which describes the emission of photons, nucleons and light fragments. It is also invoked by the Bertini cascade, which combines a Quantum Molecular Dynamics (QMD) component and a classical cascade component to study the inelastic scattering of protons. The low-energy parameterized model of the nuclear category is used to implements the elastic models. In the hadronic processes, the data driven modeling is known to provide the best approach to low energy neutron transport for radiation studies in large detectors. Theory driven modelling is the approach that promises safe extra-polation of results toward energy beyond the test beam region, and allows for maximum extension and customization of underlying physics.

INTERACTIVITY AND VISUALIZATION

The second significant extension of Geant4 capability is to define regions of behavior in experimental setup and different particle production threshold in each region characterized in detectors with precision capabilities (for eg: a muon detector with an outer layer of germanium detector). This feature improves the simulation accuracy in high resolution detector saving the computing time. The user can also efficiently generate propagation of charged particles in a field associated with geometrical volume.

The General Particle Source is a subsystem of Primary Generator Action class associated with architecture. It has a feasible functionality to implement the particle distribution in terms of x-, y, z- direction. An advanced technique i.e. particle tracking is developed in the Stepping Action class as a sub-system of user action of Geant4 kernel in order to improve the performance of CPU. This technique does not depend on the particle type or on specific physics processes. The particle tracking is categorized as primary at rest, energy loss of primary particle or secondary particle production due to decay or interaction. An interface to the event generation of primary particle is defined by the event action system. It contains the list of primary vertices and particles before processing the event. The hits and digitization are further generated where the trajectories of primary particles get recorded for each event. The schematic description of Geant4 Kernel in processing event is shown in Figure 5.

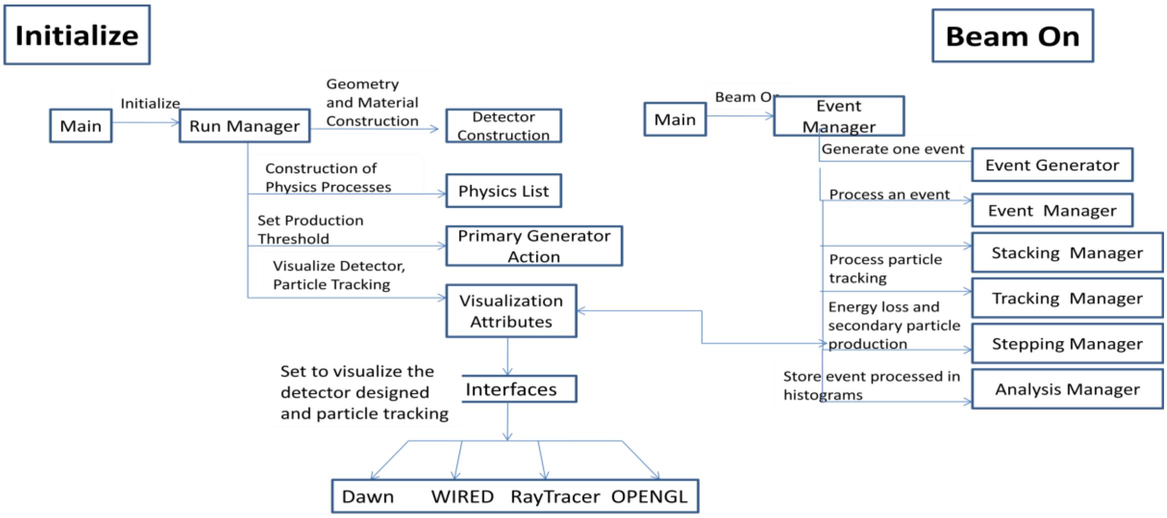

Figure 5: Initialization and Event Processing in Geant4 Kernel.

The event biasing methods are used in order to facilitate the usage of variance reduction techniques which are applicable in radiation shielding studies resulting in high gain in time efficiency. It is also associated with each volume of the geometry where physics and particle tracking are defined. For each run, the whole event processing is customized by a run action class where for each begin of a run, a histogram can be defined and gets stored at the end of each run. These are analyzed with the help of analysis tools such as ROOT, AIDA which are interface in Analysis Manager.

Introduction

Origin of Proposal

Muon detection is an essential part in the Large Hadron Collider (LHC) experiments. It helps in understanding the background of the underground detectors and to simulate the atmospheric showers induced by muons. Muons of super high energies are also considered for exploration of primary cosmic rays, neutrino studies in different arrays like Super-Kamiokande **(A.A.Petrukhin, 2014)**, GRAPES-3 (Gamma Ray Astronomy at PeV EnergieS) **(Gupta, 2014)** and for numerous environmental experiments like the solar activity characterization or climate change observations **(Dayananda, 2013)**. Also, it has successfully been used as muon tomography technique in the search for hidden rooms in pyramids or in volcanology **(B´en´, 2013)**. There are other possible applications to increase the safety procedures in mining excavations, oil industry as an easy way to search for oil bags or at the customs checkpoints, to scan the passing vehicles **(Overholt, 2015)**.

In many applications such as industry and academia, an accurate determination of the direction from where gamma rays are emitted is either needed or desirable. Radiation therapy treatments, the search for unknown sources, and homeland security applications are few of the fields that can benefit from directional sensitivity to gamma-radiation **(Cortes, 2014)**.

Hadron therapy is one of the emerging techniques which destroy the cancerous tissues by using ionizing particles while preserving the surrounding healthy tissues. The dose deposition of X-rays induced by different projectiles decreases slowly with respect to the penetration depth of the tumour region. It is also difficult to accurately define tumours which are located in denser region of the body. While compared to X-rays, the charged particle beams have a finite range of ballistics **(Paganetti, 2013)**. Both proton and ^{12}C beams deposit their maximum dose located at the end of the path. This results in a Bragg Peak where its location depends on the beam energy, tissue density and its composition. The proton beam gradually slows down by energy loss undergoing Multiple Coulomb Scattering with material. The consistency of dose deposition may also be influenced by inhomogeneous materials present in path of beam direction. These inhomogenities results in degradation of Bragg peak and its range. This uncertainty in dose distribution can be determined from Full Width Half Maximum (distance between the entrance surface of beam and distal FWHM) which has a large impact on treatment system because maximum dose of proton may be delivered to normal tissue **(SNL Sirisha, 2014)**. The point at 80% of energy deposition results in particle range during beam irradiation. Another parameter, penumbra width gives the resultant absorbed dose in distal region of Bragg peak. At low energy range (<100 MeV), proton beams is a key issue in various experimental domain such as oncological radiotherapy, radiation protection, space science and optimization of radiation monitoring detectors **(Mendez, 2015)**. SLAC has become a major US collaborator for medical physicists working on

Geant4 applications, particularly in hadrontherapy and brachytherapy for the treatment of tumours.

Review of status research and development

Monte Carlo simulations of the showers and detector are developed by the TOMUVOL (Tomography with Atmospheric Muon Volcanoes) collaboration. The atmospheric showers were simulated using GEANT4 to study the spatial distribution and energy spectrum of the muons **(Clarkson, 2014)**. The CMS (Compact Muon Solenoid, Switzerland) used a object oriented Geant4-based program to simulate the complete central CMS detector (over 1 million geometrical volumes) which utilizes the full set of electromagnetic and hadronic physics processes provided by Geant4 and detailed particle tracking (**SNL Sirisha**, GEANT4 & GAMOS- A Particle Implementation of High Energy Simulation Toolkit to Oncology Therapy, **2014**). The processes affecting the transport and collection of optical photons generated inside a scintillation detector were simulated and studied using Geant4 toolkit (**Clarkson**, The design and performance of a scintillating-fibre tracker for the cosmic-ray muon tomography of legacy nuclear waste containers, **2014**). The processes such as ionization, direct production of e^-, e^+ pairs, bremsstrahlung and inelastic muon interaction with nuclei which are studied for muon interactions with low-Z materials was discussed **(Cecchini, 2012)**. The properties of wavelength shifting fibre were studied which tends to decrease the self-absorption of detector to propagate maximum light that reaches the PMT as possible **(Riggi, 2010)** .

Precise measurements of the muon flux are important for different practical applications, both in environmental studies and for the estimation of the water equivalent depths of underground sites. A mobile detector for cosmic muon flux measurements has been setup at IFIN-HH, Romania. The device is used to measure the muon flux on different locations at the surface and underground **(Mitrica, 2013)**.

The Lawrence Berkeley National Laboratory (LBNL) designed a plastic scintillator (EJ212) which was coupled with a light guide to PMT. It was developed for detection of gamma rays and to improve efficiency of cosmic ray detection. The effect of different shielding on gamma rays produced and the cosmic ray muon flux dependence on direction were also studied **(Bachri, 2010)**.

In recent years, a numerous number of high schools and universities are making collaborations (for e.g.: CROP (Cosmic Ray Observatory Project), CHICOS (California High School Cosmic ray ObServatory), SEASA (Stockholm Educational Air Shower Array), ALTA (Alberta Large Area Time-Coincidence Array) for performing the cosmic ray studies all over the world **(Riggi F. , 2014)**. Many educational aspects tend to characterize the experiments using different detection techniques for study of fundamental properties of high energy particles. This has also offered a possible usage of the advanced nuclear laboratory which involves construction of apparatus, use of different detectors, physical measurements, muon monitoring, data analysis and interpretation for students in field of high energy physics (**Riggi S.** , Muon tomography imaging algorithms for nuclear threat detection inside large volume containers with the Muon Portal detector., **2013**).

Instead of measuring the number of particles passing through the detector, efficiency of the entire system can be determined from the coincidence measurement. The ratio of coincidence counters to optimized counters allows to study the number of particles in a particular counter detects relative to the others (**A.A.Petrukhin**, Muon puzzle in cosmic ray experiments and its possible solution, **2014**).

The sensitivity of stopping power and depth-dose distribution of proton to the relative location among adjacent materials when placed in plateau and Bragg peak region in water were studied **(Suh, 2011)**. The effect of deeply penetrating energetic ions like ^{3}He, ^{12}C, ^{20}Ne, ^{58}Ni was studied from dose profiles when passing through water phantom **(Burigo, 2013)**. The influence of low energy production threshold of secondary electrons on dose distribution of carbon ion beam in water phantom was studied **(Zahra, 2010)**. The effect of electromagnetic and hadronic processes of proton in application to oncological radiotherapy was studied **(Depauw N, 2011)**. The impact of relative biological effectiveness and passive elements which are helpful in optimizing the physical dose profiles were studied **(Bourngaleb, 2011)**.

(Thompson, 2013) reported the dependence of Bragg peak region on density of inhomogeneous media. **(Fix, 2013)** presented a novel architectural approach to design human phantom. The dose in entire organs was calculated resulting from radiation exposure. **(Robert, 2013)** described about estimation of influence of material assignment in a patient geometry for dose calculations in hadrontherapy using Geant4. The dose distribution of proton beam at energies 160 MeV, 190 MeV and 220 MeV is studied to determine the Bragg peak and proton range of different materials like water, lead and aluminum are also compared with NIST data base. Then the dose distribution based on CT data was also studied with actual treatment parameters. **(KGwosch, 2013)**, studied the dose distributions for beams of heavy and light nuclei to study the effect of nuclear fragmentation reactions on the dose profile. **(Mendez, 2015)** analyzed the physics models which contributed in studying the electromagnetic, hadronic interactions of proton beam. The Bragg profile of proton beam at different energies in water phantom for radiotherapy applications was also studied.

The muon telescope is a new experimental setup after the Geiger Muller detector and NaI detector in our Detector Physics laboratory, Department of Physics and Computer Science, Dayalbagh Educational Institute (DEI), Agra. This is an outcome of the collaboration between DEI and TIFR, Mumbai under which the Institute has acquired plastic scintillation detectors from Cosmic Ray Laboratory, Ooty for research purpose. The Nuclear Electronics for the NIM has been setup in the laboratory. The detector design using Geant4 simulation have been studied by post graduate students of physics and the simulation results compared with the experiments going on in the laboratory. In the upcoming sections, the abstract gives a brief overview of the thesis objectives which includes the fabrication and characterization of muon telescope; Geant4 based simulation study of the high energy muon interactions with cosmic ray charged particle detector and study of proton and carbon ion beam interactions in a sensitive region of a water phantom. The details of the objectives with their methodology, results and discussion from simulation and measurements of muon telescope for study of its response to muons are explained in chapter 1, 2 and 3 of the thesis outline. The energy spectrum and rotational matrix based study of gamma rays is discussed in chapter 4. The physical characteristics of particle beams in hadron therapy, its effect on curing tumors in presence of heterogeneous medium and specific dose equivalent required for patients of various ages are discussed in chapter 5. The effect of nuclear interactions in dose computation of ^{12}C in tumors is given in chapter 6. The main contributions of the thesis are outlined in the chapter 7.

Thesis Objectives

Step I: Fabricate and characterize the muon telescope.

a. Design and fabricate a muon telescope of dimension 23.5x24x2 cm^3, embedded with single and double fibre at Cosmic Ray laboratory, field station of TIFR, Ooty.
b. Find the acceptance of the telescope.
c. Find the efficiency of muon telescope.

Step II: Geant4 based simulation study of the high energy muon interactions with muon telescope.

a. Study the dependence of muon interaction processes on differential cross-section of muon telescope and muon energy loss within the scintillator.
b. Observe the muon response of the telescope and its effect on implementing various surface reflectors of UNIFIED model.
c. Study the electromagnetic interactions in telescope using standard, low energy and Penelope packages.

Step III: Energy spectrum and Rotational Matrix based study of Gamma rays.

a. Study the pulse height spectrum of the detector in Geant4.
b. Observe the effect of detector to source distance on pulse height spectrum.
c. Study the dependence of Compton scattering process on scattering angle.

Step IV: Analytical Study of proton and carbon ion beam interactions in a sensitive region of a water phantom.

a. Determine the energy deposition of particle beams in homogeneous and inhomogeneous materials: Bragg Peak.
b. Compute the specific dose equivalent of proton beam for distinct ages of human phantom.
c. Study the influence of nucleus-nucleus collisions in study of dose computation.

Thesis Outline

Chapter 1

A brief summary for importance to study the particle interactions of leptons, protons and heavy ions with radiation detectors will be explained. Detector sensitivity for incident particle energy depends on many factors including cross-section for ionizing reactions in the detector and its mass, inherent detector noise, surface material surrounding the sensitive volume of the detector **(Riggi F. , 2014)**. The cross-section and detector mass determine the probability of the incident particle to convert its energy in the detector into form of ionization. When a highly ionized charged particle is incident on a detector, it produces ionization resulting in a certain minimum amount of signal which is further determined by noise from the detector and its associated electronics in the form of a fluctuating voltage or current at the detector output **(Gupta, 2014)**. For a given amount of radiation type in an energy range, the total amount of ionization produced is determined by sensitive volume. A second limiting factor is the material covering the sensitive volume of the detector because of the absorption, only radiation with sufficient energy to penetrate this layer can be detected **(Cecchini, 2012)**. For measurement of energy spectra, an important factor which must be considered is the response of the detector. When any radiation detector operates in pulse mode, amplitude of every pulse carries important information about the charge generated by the particular radiation interaction in the detector. So it is very necessary to store each pulse according to its amplitude. In pulse height spectrum each pulse sorted into one of the large number of bin (channel) which corresponds to a single pulse of small amplitude range.

Hadrontherapy is a different technique of radiotherapy that makes use of fast non-elementary particles made of quarks i.e.; protons, neutrons and light nuclei are used to control tumours **(Mendez, 2015)**. These particles stop at a certain depth in a substance and deposit a large portion of its energy near the end of its range. The deposited energy forms a narrow dose peak known as the Bragg Peak. This physical characteristic is suitable for radio-therapeutic treatment of tumours because it sterilizes cells in the target volume while minimizing damage to healthy tissues along the radiation path **(Dionisi, 2014)**. The energies required for therapy of deep-seated with hadrons are typically in the range 60 to 230 MeV for protons and 120 to 400 MeV/nucleon for carbon ions **(Gudowska, 2014)**. These beam energies can be achieved with synchrotrons, cyclotrons or linacs as main accelerators. But the choice of accelerators mainly depends on beam delivery system or desired particle species.

Chapter 2

This chapter gives a detailed description of methodology about fabrication and assembly of detectors, high voltage power supply design, setting up of electronics for interfacing with NIM data acquisition. Some important aspects of the experimental detection of particles, such as the relative importance of different interaction mechanisms of a particle with the detector material, evaluation of geometrical acceptance, energy deposition to sensitive volumes, are difficult to understand without proper simulations of the detector response. A widely used package to treat all these aspects is the Geant4 simulation code, where the user can define the physics processes, geometry, material and surface properties of the detector. The simulation is performed using an object oriented toolkit Geant4 along with ROOT which is used for data analysis.

Chapter 3

(S.N.L Sirisha, Sonali Bhatnagar ***Simulation based study of Muon Telescope and parameters affecting detector response. European Journal of Physics - IOP (Submitted Revised Version – June 2015).***

The muon interaction processes in different materials was studied using Geant4 simulation toolkit. The total cross-section, interaction length and energy loss of muons was calculated. The dependance of muon cross-section mechanisms on muon energy transfer to secondaries was studied. At moderate muon energy i.e. at E=100GeV, the dominant interaction process in both iron and polystyrene materials is observed to be production of knock-on electrons. But when we consider higher energies (E=10 TeV), the production of neutral particles and hadronic flow is prevailing for polystyrene, where as in case of iron the electron pair production is foremost process during muon interaction. The result for differential cross-section of muon interaction in iron is also comparable with the literature et.al **(Bogdanov, 2012)**.

The muon energy loss associated with these processes varies linearly in relation with muon energy. It is to be observed that bremsstrahlung process gets concealed due to mass of muon. The electron pair-production and bremsstrahlung increases relative to muon energy in case of iron and these processes are dominant in case of higher energies. For polystyrene material, the proportionality of energy loss to muon energy in case of bremsstrahlung process is very less comparable to iron. The effect on muon energy loss by implemeting optional physics models i.e. (G4StandardEM_opt0, G4StandardEM_opt1, G4StandardEM_opt2, G4StandardEM_opt3) of Standard EM Package is studied.

The physics processes necessary for implementation using Standard EM Package in different bulk density materials like iron, polystyrene, hydrogen and carbon are studied. The effect of multiple scattering on muon interaction length and total cross-section within these materials is observed. The interaction length of muon has an exponential decrease in nature on increasing the incident muon energy while total cross-section has linear increase w.r.t energy of muon. After a certain cut-off region of muon energy, both the parameters remain constant. For further accuracy in results, step cut of incident muon is varied to observe its effect on total cross-section and interaction length.

The physics of optical photon transport is defined to predict the light distribution in scintillating materials. The surface characteristics of the muon telescope based on UNIFIED optical model characterized with different properties such as specular spike, specular lobe, backscatter, and Lambertian are implemented to observe the photon yield of the plastic scintillator for various reflectors such as Teflon tape, ESR film, Lumirror, paint, and Tyvek paper in each polished, etched, and rough-cut surfaces.

The experimental measurements include the description of fabrication of polystyrene based scintillator paddles (23.5x24x2 cm^3) and the experimental setup used for fast signal processing through Nuclear Instrumentation Modules. The preliminary testing of light leakage in detectors and optimisation of discriminator threshold voltage are computed. Counting statistics is also applied to observe the uncertainty within the data range (S.N.L *Sirisha, Shubhi Parolia, Sonali Bhatnagar, "**Preliminary Study of Muon Telescope",** IARPNC-2014, BARC. Mumbai).*

The coincidence rate as function of detector seperation in horizontal and vertical direction is determined to study the decoherence curve which helps in finding the energy distribution of the primary particle source information. It is nearly 4 Hz/cm^2/sec when detectors are placed with null separation in the vertical direction. In second case, the distance is varied horizontally where the coincidence rate is approximately 1 Hz/cm^2/sec at zero separation among the detectors.

The efficiency of the muon telescope is also observed with respect to environmental conditions to study its impact due to temperature and solar irradiance at ground level. It is necessary to understand the temperature effect on the muon flux due to heliosphere processes such as inherent acceleration mechanism, information about its source and transient modulation effect by the sun *(S.N.L Sirisha, Sonali Bhatnagar* ***Simulation based study of Muon Telescope and parameters affecting detector response. European Journal of Physics - IOP (Submitted Revised Version – June 2015).***

The characteristic study of secondary cosmic rays provide a basic and advanced educational activity for undergraduate, post graduate students to carry out conceptual experiments. (S.N.L Sirisha, Kajal Garg, Sonali Bhatnagar "***MUON TELESCOPE – AN EDUCATIONAL EXPERIMENT FOR POST GRADUATE STUDENTS, Submitted revised version to Physics Education Journal, June 2015)***.

Chapter 4

A plastic scintillation detector was simulated in Geant4 and the distance from source to detector was varied. The effect on intensity and peak energy is observed. Then a scatterer is placed in front of the gamma source where the angle between scatterer and detector is rotated to study Compton scattering (Kajal Garg, S.N.L Sirisha, Sonali Bhatnagar; ***"The energy spectrum and Rotational matrix based study of gamma rays",*** ACM 978-1-4503-3216-3/14/11, ICTCS-2014).

Chapter 5

The stopping power in heavy charged particles is an important parameter in determining the energy loss. It is calculated for proton in materials like Brass, Al, Cu, Pb, Water, Plexiglas, and Galactic within an energy range 0.1 to 10^5 MeV. *(S.N.L Sirisha, Sonali Bhatnagar; Paper titled* ***"Stopping Power of Proton in different materials – A Geant4 based Simulation"*** *at "DAE Symposium on Nuclear Physics, Dec (03-07)2012" organized by Board of Research in Nuclear Sciences and Department of Atomic Energy.)*

The physical interpretation of dose distribution curves for proton beam is studied from Geant4 simulation of the set up which is installed at Laboratory Nazionali del Sud (INFN) in Catania for curing ocular tumours. The significance of the spectra due to secondary particles produced in the interactions for 60 MeV proton beam is discussed which is relevant for the study of Radioactive Biological Efficiency (RBE) and Spread Out in Bragg Peak (SOBP). *(S.N.L Sirisha, Sonali Bhatnagar; Paper titled* ***"Stopping Power of Proton beam in water Phantom – A simulational study"*** *at* ***"National Systems Conference-2012"*** *during December (06-08), 2012 and also published by Springer in the Lecture Notes in Electrical Engineering, Volume 188: titled* ***"Recent Advancements in Systems Modelling Applications"****, page no. (79-88), ISBN: 978-81-322-1034-4.)*

An overview of the basic architecture and implementation of physics processes in Geant4 and GAMOS toolkits are discussed. The dose deposition of a passive proton beam of 60 to 240 MeV in a human phantom geometry is calculated. The resulting Bragg peak, range and penumbra width were calculated and verified with results of other groups. *(S.N.L Sirisha, Sonali Bhatnagar , Paper titled* ***"Geant4: GATE and GAMOS – A systematic Implementation of HEP Simulation toolkit to oncology therapy",*** *presented in "IEEE Student's technology Symposium – 2014", IIT Kharagpur, 28Feb-2March, 2014 organized by IEEE Student Branch, IIT Kharagpur and IEEE Kharagpur Section, Kharagpur. It is also published in the IEEE Explore with ISBN no. 978-1-4799-2608-4/14/$31.00 ©2014 IEEE)*

Whenever a proton beam is radiated through the tumour region a significant influence over the stopping power and the depth-dose distribution of the proton energy can be observed due to the adjacent materials. The effect of the heterogeneous medium in tumour has been studied by several groups to assess the ability of beam convolution which predicts the dose required. Adipose, bone and soft tissues materials are considered for the present study. The human organs along with the positioning of the tumour region were designed. The suitable energy range for each tumour of the human organ was optimized. The study was also followed with thickness variation of each material from 0.1 cm to 1.0 cm. Various parameters of the Bragg curve were computed i.e. Bragg peak position, range, penumbra width, full width at half maximum and dose of Bragg curve. A significant shift in the Bragg peak position is observed in each case i.e., approx. -0.36% for muscular skeleton, -0.44% for soft tissue. The applications of these systems in fields of nuclear fragmentation for carbon ion therapy, nuclear imaging and hadrontherapy for *in vivo* dose monitoring are also discussed. *(S.N.L Sirisha, Sonali Bhatnagar,* ***Paper Title: "Geant4 - Study of Dose Curve Parameters of Tumour in Human Tissues Using Passive Proton Beam****", 2014 Sixth International Conference on Computational Intelligence and Communication Networks, Udaipur, November 14-16, 2014, and published by IEEE computer society with ISBN no. 978-1-4799-6929-6/14, DOI 10.1109/.50)*

The significant effect of the absorbed dose of proton beam in different ages is studied. Distinct phantom volumes with their respective organs i.e. brain, kidney and thyroid of children at various ages such as 0, 1, 5, 10, 15 years and an adult are considered from OAK RIDGE NATIONAL LABORATORY (ORNL) report (Thompson, 2013) for present simulation study. The relation between dose equivalent and absorbed dose as function of depth to target volume is computed. We observed that the dose deposition is dependent on the age where patient at younger age receives dose at higher rate while it gradually decreases in the other cases i.e. 10 year, 15 year and adult. The step length of the particle is varied which imposes a limit during particle interaction in the medium per unit length. The obtained dose rate on varying the step length is compared among the Geant4 9.3 and 9.4 versions (*SNL Sirisha, Sonali Bhatnagar* ***"Determination of Equivalent Dose of Specific Organs in computational age dependent phantoms using proton therapy in Geant4",*** *Submitted the extended paper to IEEE Xplore, CICN, May-2015).*

Chapter 6

The study regarding energy deposition by ^{12}C in a homogeneous and heterogeneous medium is performed to observe its impact on adjacent materials while curing tumours. The influence of nuclear interactions on dose computation is studied. When a projectile hits a target nucleus, light particles are promptly emitted and a quasi target is formed. The excited nucleus decay through combination of fragmentation process (entrance channel) and decay phase. This is simulated in Geant4 to understand the nucleus-nucleus collisions. The Binary Intra-nuclear Cascade model based on the Quantum molecular dynamics is used for fragmentation process which assumes that the nucleons of the projectile are free from each other.

Chapter 7: Conclusion

Calibration of Muon Telescope

1. Fabrication of scintillation paddles – T.I.F.R, Mumbai.
2. Preliminary studies of muon telescope which includes:
   i. ***Optimizing discriminator threshold***
   ii. ***Pulse width***
   iii. ***PMT operating voltage***
   iv. ***PMT amplitude dependence on high voltage***
3. Muon count rate dependence on varying the horizontal and vertical distance between two paddles for study of decoherence curve.
4. Muon telescope efficiency (3-fold efficiency) and its effect by environmental factors such as temperature, pressure.

Muon Interaction Study of a Muon Telescope using Geant4

5. Cross-section dependence of muon in materials of different density with respect to multiple coulomb scattering.
6. Acceptance of muon telescope and studied the solid angle dependence as function on varying distance between paddles
7. Muon telescope response and its effect by surface characteristics.

Energy spectrum and Rotational Matrix based study of Gamma rays

8. Simulated and analyzed pulse height spectrum of the detector in Geant4.
9. Studied the effect of detector to source distance on pulse height spectrum from the intensity of peak energy.
10. The effect of Compton scattering dependence on scattering angle for NaI (Tl) is observed.

Hadronic Interaction Study in Human Phantom using Geant4 (Dosimetry)

11. Computed physical characteristics of proton beam such as stopping power and range.
12. Inhomogenities are shown to be an important consideration to the depth dose distribution of therapeutic proton beams.
13. Therapeutic energy range of proton beam is observed to be dependent on the geometry of the medium.
14. Proton equivalent dose for specific organs such as brain, thyroid and kidney.
15. The influence of ^{12}C in nuclear interactions during dose computation in homogeneous and heterogeneous medium is studied.

References

A.A.Petrukhin. (2014). Muon puzzle in cosmic ray experiments and its possible solution. *Nuclear Instruments and Methods in Physics Research A* , 228-231.

B´en´, S. (2013). Air shower simulation for background estimation in muon tomography of volcanoes. *Geosci. Instrum. Method. Data Syst* , 11-15.

Bachri, A. (2010). Analysis of Gamma rays and cosmic ray muons wirh single detector. *Journal of Arkansas of sciences* , 27-32.

Bogdanov, A. (2012). Energy spectrum of cosmic ray muons in ∼100 TeV energy region reconstructed from the BUST data. *Astroparticle physics* , 224.

Bourngaleb, F. (2011). Monte Carlo Simulation for Beam Delivery Line Design in radiotherapy with heavy ion beams. *INTECH* .

Burigo, L. (2013). Microdosimetry of radiation field from a therapeutic 12C beam in water: A study with Geant4 toolkit. *Nuclear Instruments and Methods in Physics Research B* , 37-53.

Cecchini. (2012). Atmospheric muons: experimental aspects. *Geosci. Instrum. Method. Data Syst* , 185-196.

Clarkson, A. (2014). GEANT4 simulationofascintillating-fibretrackerforthecosmic-ray muon tomographyoflegacynuclearwastecontainers. *NuclearInstrumentsandMethodsinPhysics Research A* , 746; 64–73.

Clarkson, A. (2014). The design and performance of a scintillating-fibre tracker for the cosmic-ray muon tomography of legacy nuclear waste containers. *Nuclear Instruments and Methods in Physics Research A* , 138-149.

Cortes, M. L. (2014). BC404 scintillators as gamma locators studied via Geant4 simulations. *Journal of Instrumentation* , JINST 9 C05049.

Dayananda, M. A. (2013). Correlation Studies of Cosmic Ray Flux and Atmospheric and Space Weather. *ScholarWorks @ Georgia State University* .

Depauw N, S. J. (2011). Sensitivity study of proton radiography and comparison with kV and MV x-ray imaging using GEANT4 Monte Carlo simulations. *Phys Med Biol* , 2407-2421.

Dionisi, F. (2014). Is there a role for proton therapy in the treatment of hepatocellular carcinoma? A systematic review. *Radiotherapy and Oncology* , 1-10.

Fix, M. K. (2013). Macro Monte Carlo for dose calculation of proton beams. *PHYSICS IN MEDICINE AND BIOLOGY* , 2027-2044.

Gudowska, I. (2014). Influence of the patient size on secondary doses delivered in light ion beams . *Progress in Nuclear Science and Technology* , 294-297.

Gupta, S. (2014). High Energy Astroparticle Physics at Ooty and the GRAPES-3 Experiment. *Proc Indian Natn Sci Acad* , 80 No. 4, pp. 827-876.

KGwosch. (2013). Non-invasive monitoring of therapeutic carbon ionbeams in a homogeneous phantom by tracking of secondary ions. *PHYSICS IN MEDICINE AND BIOLOGY* , 3755-3773.

Kim, Y. H. (2012). Cosmic ray measurement and experimental temperature analysis with a muon detector. *Journal of Korean Physical Society* , 647-652.

Mendez, J. R. (2015). Improved efficiency in Monte Carlo simulation for passive-scattering proton therapy. *Physics in Medicine & Biology* , Phys. Med. Biol. 60; 5019–5035.

Mitrica, B. (2013). A Mobile Detector for Muon Measurements Based on Two Different Techniques. *Advances in High Energy Physics* , 1-7.

Overholt, A. C. (2015). A link between solar events and congenital malformations: Is ionizing radiation??

Paganetti, H. (2013). Biological Considerations When Comparing Proton Therapy With Photon Therapy. *Radiation Oncology* , 77-87.

Riggi, F. (2014). An extensiveairshowertriggerstationforthe Muon Portal detector. *Nuclear Instruments and Methods in Physics Research A* , 142-149.

Riggi, S. (2010). GEANT4 simulation of plastic scintillator strips with embedded optical fibers for a prototype of tomographic system. *Nuclear Instruments and Methods in Physics Research A* , 583-590.

Riggi, S. (2013). Muon tomography imaging algorithms for nuclear threat detection inside large volume containers with the Muon Portal detector. *Nuclear Instruments and Methods in Physics Research A* , 59.

Robert, C. (2013). Distributions of secondary particles in proton andcarbon-ion therapy: a comparison betweenGATE/Geant4 and FLUKA Monte Carlo codes. *PHYSICS IN MEDICINE AND BIOLOGY* , 58; 2879-2899.

Saavedra, O. (2013). NEVOD-DECOR experiment: results and future . *Journal of Physics: COnference Series* , 409.

SNL Sirisha, Sonali. Bhatnagar. (2014). Geant4 - Study of Dose Curve Parameters of Tumor in Human Tissues Using Passive Proton Beam. *IEEE Computer Society* , 978-1-4799-6929-6/14.

SNL Sirisha, Sonali. Bhatnagar. (2014). GEANT4 & GAMOS- A Particle Implementation of High Energy Simulation Toolkit to Oncology Therapy. *IEEE Computer Society* , 978-1-4799-2608-4/14; 25-30.

Suh, T. S. (2011). Variation of Bragg Curve Characteristic Induced by Changing the position of Inhomogeneous material: Geant4 simulation study. *Journal of Korean Physical Society* .

Thompson, L. (2013). A Head and Neck Simulator for Radiology and Radiotherapy. *IEEE TRANSACTIONS ON NUCLEAR SCIENCE* , 60;3.

Zahra, N. (2010). Influence of Geant4 paramters on dose distribution and computation time for carbon io therapy simulation. *Physics media* .